INTERFERENCE LITHOGRAPHY FOR OPTICAL DEVICES AND COATINGS

BY

ABIGAIL THERESE JUHL

DISSERTATION

Submitted in partial fulfillment of the requirements
for the degree of Doctor of Philosophy in Materials Science and Engineering
in the Graduate College of the
University of Illinois at Urbana-Champaign, 2010

Urbana, Illinois

Doctoral Committee:

   Professor Paul V. Braun, Chair and Director of Research
   Professor John A. Rogers
   Professor Kenneth S. Schweizer
   Professor Nancy R. Sottos

Report Documentation Page		*Form Approved* *OMB No. 0704-0188*

Public reporting burden for the collection of information is estimated to average 1 hour per response, including the time for reviewing instructions, searching existing data sources, gathering and maintaining the data needed, and completing and reviewing the collection of information. Send comments regarding this burden estimate or any other aspect of this collection of information, including suggestions for reducing this burden, to Washington Headquarters Services, Directorate for Information Operations and Reports, 1215 Jefferson Davis Highway, Suite 1204, Arlington VA 22202-4302. Respondents should be aware that notwithstanding any other provision of law, no person shall be subject to a penalty for failing to comply with a collection of information if it does not display a currently valid OMB control number.

1. REPORT DATE **2010**	2. REPORT TYPE	3. DATES COVERED **00-00-2010 to 00-00-2010**
4. TITLE AND SUBTITLE **Interference Lithography for Optical Devices and Coatings**		5a. CONTRACT NUMBER
		5b. GRANT NUMBER
		5c. PROGRAM ELEMENT NUMBER
6. AUTHOR(S)		5d. PROJECT NUMBER
		5e. TASK NUMBER
		5f. WORK UNIT NUMBER
7. PERFORMING ORGANIZATION NAME(S) AND ADDRESS(ES) **Philosophy in Materials Science and Engineering ,Graduate College of the University of Illinois ,at Urbana-Champaign,Urbana,IL**		8. PERFORMING ORGANIZATION REPORT NUMBER
9. SPONSORING/MONITORING AGENCY NAME(S) AND ADDRESS(ES)		10. SPONSOR/MONITOR'S ACRONYM(S)
		11. SPONSOR/MONITOR'S REPORT NUMBER(S)

12. DISTRIBUTION/AVAILABILITY STATEMENT
Approved for public release; distribution unlimited

13. SUPPLEMENTARY NOTES
Dissertation.

14. ABSTRACT
Interference lithography can create large-area, defect-free nanostructures with unique optical properties. In this thesis, interference lithography will be utilized to create photonic crystals for functional devices or coatings. For instance, typical lithographic processing techniques were used to create 1, 2 and 3 dimensional photonic crystals in SU8 photoresist. These structures were in-filled with birefringent liquid crystal to make active devices, and the orientation of the liquid crystal directors within the SU8 matrix was studied. Most of this thesis will be focused on utilizing polymerization induced phase separation as a single-step method for fabrication by interference lithography. For example, layered polymer/nanoparticle composites have been created through the one-step two-beam interference lithographic exposure of a dispersion of 25 and 50 nm silica particles within a photopolymerizable mixture at a wavelength of 532 nm. In the areas of constructive interference, the monomer begins to polymerize via a free-radical process and concurrently the nanoparticles move into the regions of destructive interference. The holographic exposure of the particles within the monomer resin offers a single-step method to anisotropically structure the nanoconstituents within a composite. A one-step holographic exposure was also used to fabricate self-healing coatings that use water from the environment to catalyze polymerization. Polymerization induced phase separation was used to sequester an isocyanate monomer within an acrylate matrix. Due to the periodic modulation of the index of refraction between the monomer and polymer, the coating can reflect a desired wavelength, allowing for tunable coloration. When the coating is scratched, polymerization of the liquid isocyanate is catalyzed by moisture in air; if the indices of the two polymers are matched, the coatings turn transparent after healing. Interference lithography offers a method of creating multifunctional self-healing coatings that readout when damage has occurred.

15. SUBJECT TERMS

16. SECURITY CLASSIFICATION OF:			17. LIMITATION OF ABSTRACT	18. NUMBER OF PAGES	19a. NAME OF RESPONSIBLE PERSON
a. REPORT **unclassified**	b. ABSTRACT **unclassified**	c. THIS PAGE **unclassified**	**Public Release**	**124**	

ABSTRACT

Interference lithography can create large-area, defect-free nanostructures with unique optical properties. In this thesis, interference lithography will be utilized to create photonic crystals for functional devices or coatings. For instance, typical lithographic processing techniques were used to create 1, 2 and 3 dimensional photonic crystals in SU8 photoresist. These structures were in-filled with birefringent liquid crystal to make active devices, and the orientation of the liquid crystal directors within the SU8 matrix was studied.

Most of this thesis will be focused on utilizing polymerization induced phase separation as a single-step method for fabrication by interference lithography. For example, layered polymer/nanoparticle composites have been created through the one-step two-beam interference lithographic exposure of a dispersion of 25 and 50 nm silica particles within a photopolymerizable mixture at a wavelength of 532 nm. In the areas of constructive interference, the monomer begins to polymerize via a free-radical process and concurrently the nanoparticles move into the regions of destructive interference. The holographic exposure of the particles within the monomer resin offers a single-step method to anisotropically structure the nanoconstituents within a composite.

A one-step holographic exposure was also used to fabricate self- healing coatings that use water from the environment to catalyze polymerization. Polymerization induced phase separation was used to sequester an isocyanate monomer within an acrylate matrix. Due to the periodic modulation of the index of refraction between the monomer and polymer, the coating can reflect a desired wavelength, allowing for tunable coloration. When the coating is scratched, polymerization of the liquid isocyanate is catalyzed by moisture in air; if the indices of the two polymers are matched, the coatings turn transparent after healing. Interference lithography offers

a method of creating multifunctional self-healing coatings that readout when damage has occurred.

I would like to thank Christy Chen for her help with SU8 processing and laser alignment, Andreas Menzel for his help with liquid crystals, Congjun Wang for quantum dot synthesis, and Hailong Ning for all of his help in the laser lab. Special thanks to John Koval who worked with me as an undergrad for many years.

This work would not have been possible without the support and the friends from my research group. Special thanks to Jericho Moll, Margaret Shyr, Matt George, Vinayak Ramanan, Dara Gough, Sid Gupta, Erik Nelson, Aaron Jackson, Corissa Lee, and Xindi Yu for research discussions, encouragement, and making my time at Illinois much more enjoyable.

Finally, I would like to thank my parents who love me in success or failure, who encourage me, and who remind me of the important things in life. I thank my brothers: Josh, Jake, and John for their willingness to eat Thanksgiving dinner in Illinois on my apartment floor. I especially want to thank my husband Shane who taught me the real meaning of _for better or for worse, for richer or for poorer, in sickness and in health, to love and to cherish.'

TABLE OF CONTENTS

CHAPTER 1

INTRODUCTION

1.1...Multib eam Interference Lithography

The directed assembly of materials has been of considerable interest for a number of years, however only recently has it become possible to program structure and properties on the nanoscale with the precision required for important nanophotonic applications like photonic crystals, plasmonic devices, waveguides, lasers, solar cells, and optical switches. Multibeam optical interference is being utilized to create 3D nanostructured solids with almost limitless structural complexity. Optical interference has the unique ability to create virtually any periodic structure through control of the phase, intensity, polarization and direction of the interfering laser beams. A number of unique optical interference approaches have been applied to program the structure of 3D solids with ever increasing complexity over length scales ranging from 10's of nanometers to micrometers.

1.1.1 Interference of Waves

Interference lithography is the interaction between two or more coherent light sources to create spatially periodic regions of high and low intensity light which are -recorded within a photosensitive media. Thomas Young experimentally demonstrated the interference pattern between two coherent beams over two hundred years ago.[1] The characteristic two beam interference pattern is governed by Bragg's Law. When two coherent beams are interfering, as the green lines are in figure 1.1, the incident beam must stay in phase and parallel up to the point at which the top of the beam strikes the top of the surface of the sample. When the incoming

beam hits the surface of the sample it is refracted and the lower part of the beam must travel the

extra distance AC + CB for the incident beam to remain coherent. This extra distance must be an

integral (m) multiple of the wavelength (λ) for the phase of the beams to remain the same, or:

$$AC + CB = m\lambda$$

Based on Snell's Law, if the incoming beam hits the surface at an angle ($\theta/2$), then: [1]

$$\sin(\phi) = \frac{n_1 \cdot \sin(\frac{\theta}{2})}{n_2}$$

Using trigonometry, AC $=$ CB $=$ CE$\cdot\sin(90-\phi)$. Since AC $+$ CB $= m\lambda$, then:

$$\Lambda = \frac{m\lambda n_2}{2n_1 \cdot \sin(\frac{\theta}{2})}$$

Therefore, the spacing between interference maxima (Λ) is dependent on the incident angle of the

beam, the wavelength of the laser, and the indices of refraction. The interference pattern is also

dependent on polarization, because two orthogonal polarizations will not interfere.
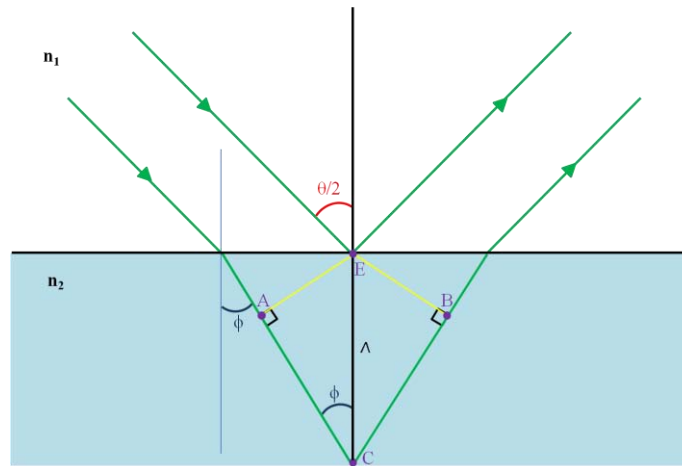
Figure 1.1. Schematic diagram of two coherent interfering beams for the derivation of Bragg's
Law: $\Lambda = (m\lambda n_2) / (2n_1 \cdot \sin(\theta/2))$.

Since the invention of the modern laser in 1960,[2] it became experimentally feasible to interfere many coherent beams in a variety of geometries. Using three or more coherent beams makes determining the final interference pattern more complex because three beams creates a two-dimensional periodicity, and four or more beams create a three-dimensional periodicity. (Figure 1.2)

2 beams (1D)	3 beams (2D)	4 beams (3D)
1-D	2-D	3-D
periodic in one direction	periodic in two directions	periodic in three directions
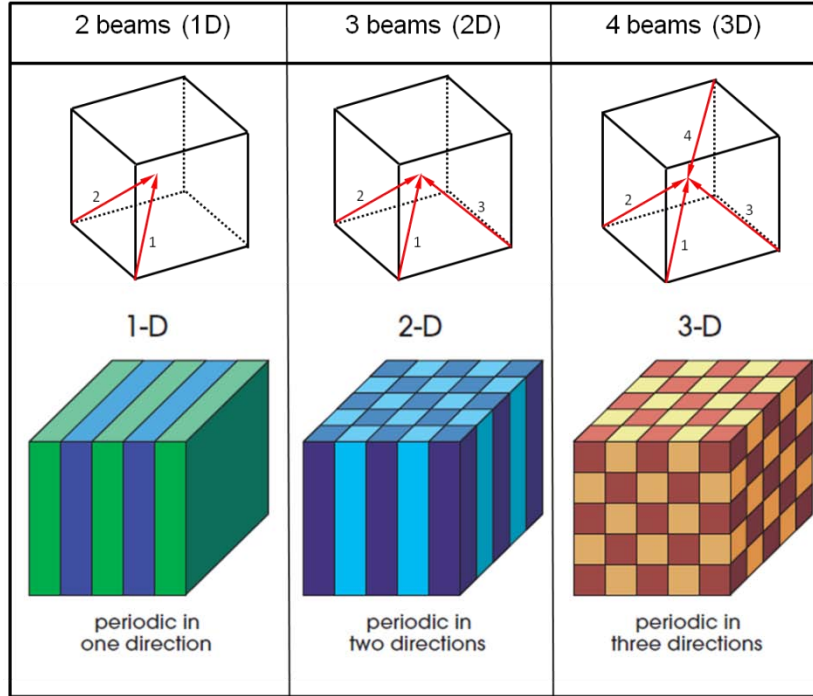
Figure 1.2. A representation of the periodic nanostructures formed by two, three, and four beam laser interference patterns. The two beam setup offers a 1 dimensional periodicity, while the three beam setup, a 2 dimensional periodicity, and the four beam setup has a 3 dimensional periodicity. Figure adapted from "Photonic Crystals: Molding the Flow of Light".[3]

To determine why interference occurs, consider multiple plane waves with frequency ω, a wave vector k, and a complex electric field E_0:

$$E_j(r,t) = (E_{0j}e^{i(k_j \cdot r - \omega t)}), \quad j=1,\ldots,N$$

Based on the superposition principal, the total electric field is equal to the sum of the electric fields of the individual plane waves:

$$E_T(r,t) = \sum_{j=1}^{N} E_j(r,t)$$

The resulting intensity of the total wave is the square of the magnitude of the total electric field, or:

$$I(r) = \sum_{j=1}^{N} |E_{0j}|^2 + \sum_{1 \le i < j \le N} 2\,\mathrm{Re}(E_{0i} \cdot E_{0j}^*)\cos[(k_i - k_j)\cdot r] - 2\,\mathrm{Im}(E_{0i} \cdot E_{0i}^*)\sin[(k_i - k_j)\cdot r]$$

‗Re' stands for ‗real' and ‗Im' stands for ‗imaginary'. The intensity of the total wave is not just a sum of the intensities of the individual waves (blue term). The total wave intensity also consists of two addition terms (red terms) which are called interference terms.[4] The intensity depends on position, which is the definition of an interference pattern. The intensity pattern is dependent on the wavelength of the light source, the refractive index of the photosensitive media, and the polarization, power, phase, and geometry of each beam. With so many parameters to engineer, it is possible to create all of the Bravais lattices using three and four coherent laser beams.[5]

1.1.2 Fabrication of Periodic Structures

In 1995, Mei showed it was possible to create three-dimensional ordered patterns using holography.[6] In 1997, Berger et al. used three coherent beams to record a two dimensional pattern.[7] A polymer photoresist served as a template into which this pattern was recorded, which caused photochemical reactions that allowed the selective removal of material from the regions of constructive interference. Berger also theorized the possibility of creating 3D nanostructures using interference lithography.[7] This was followed three years later by the production of three dimensional nanostructures using interference lithography.[8] The resultant nanostructure was face centered cubic-like and was recorded in SU-8 photoresist using four coherent 355 nm laser beams. (Figure 1.3)

4
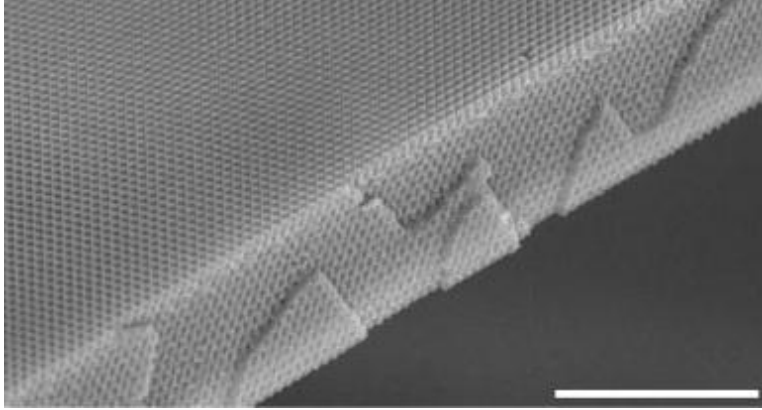
Figure 1.3. SEM micrograph of a photonic crystal fabricated by interference lithography. The top surface is the (111) plane and the scale bar is 10 μm. Image adapted from *Nature*, **404**, 53 (2000).[8]

1.1.3 Applications

Interference lithography is typically used to nanostructure materials on the order of the wavelength of light for optical applications such as photonic crystals.[7-14] Photonic crystals modify the motion of photons due to periodic changes in dielectric constant.[3, 15] Alternating planes of material cause strong modulation of the light due to refraction and reflection off the interfaces. A photonic crystal with a photonic band gap is analogous to a semiconductor with an electronic band gap. There are certain frequencies of light that cannot propagate within a photonic crystal, just as there are certain electronic energies that cannot exist within an electronic band gap.

One-dimensional photonic crystals have been commercially available for many years as high efficiency thin film optics like dielectric mirrors or optical filters, which reflect certain frequencies of light. Adding another dimension of periodicity can localize light at a defect or at a surface. Two-dimensional photonic crystals are used to create laser cavities for low-threshold lasers,[16] sensors,[17] and optical fibers for low-loss guidance of light.[18] Extending confinement to three dimensions (3D) allows for a complete photonic band gap in which a certain frequency of light cannot propagate in any direction. Defect structures can be placed inside of the three-

dimensional photonic crystal to guide the light in a desired direction.[10, 19-20] Metallic 3D photonic crystal emitters are used for thermal photovoltaic power generation.[21-22] Yablonovitch proposed fabricating a 3D photonic crystal where an electronic and photonic gap overlapped to reduce spontaneous emission and enhance the performance of lasers, heterojunctions, bipolar transistors, and solar cells.[23] Zero threshold lasers[24] and superprisms[25] have also been proposed.

1.2...Photoi nitiation

The properties of a polymeric material are defined by the monomeric units. Polymerization is the process of converting the liquid monomer species into solid polymer. There are two main mechanisms for synthesizing polymers: step-growth and chain polymerization. In step-growth polymerization, bifunctional or multifunctional monomers are built-up in a step-wise fashion from dimer to trimers and continuing to larger molecular weights until the monomer is exhausted. Nylon, polyester, and polyurethanes are step-growth polymers. Chain-growth is the polymerization of unsaturated compounds by cationic or free-radical polymerization mechanisms.[26] Photopolymerizations are usually free-radical chain reactions with initiation by a photochemical event.[27] For clarity of nomenclature, a photoinitiator, as defined by Fouassier, is a molecule employed alone or in a chemical system that absorbs light and forms reactive initiating species: radicals, H^+, or cation radicals. A coinitiator does not absorb light but participates in the forming the intiating species. A photosensitizer absorbs light and transfers the excitation to another molecule that generates active centers.[27]

Photo-induced chain polymerization occurs in three steps: initiation, propagation, and termination. The general mechanism for free-radical polymerization is in figure 1.4. An initiator molecule, I, absorbs light and cleaves into two reactive species, R·. The free radical then attacks

the monomer, M, breaks open the double bond, and the free radical moves to the other end of the

monomer. As long as unreacted monomers are available, this reaction propagates by reacting

radical monomer species with the non-radical monomer species. This continues until two

radicals react together and terminate the polymer chain. The total time from initiation to

termination is usually only a few seconds.[28-29]

Initiation

$$I \xrightarrow{k_d} 2R\cdot$$

$$R\cdot + M \xrightarrow{k_a} M_1\cdot$$

Propagation

$$M_1\cdot + M \xrightarrow{k_p} M_2\cdot$$

$$M_2\cdot + M \xrightarrow{k_v} M_3\cdot$$

$$M_x\cdot + M \xrightarrow{k_p} M_{x\cdot+1}$$

Termination

$$M_x\cdot + M_y\cdot \xrightarrow{k_{tc}} M_{x+y}$$

$$M_x\cdot + M_y\cdot \xrightarrow{k_{td}} M_x + M_y$$
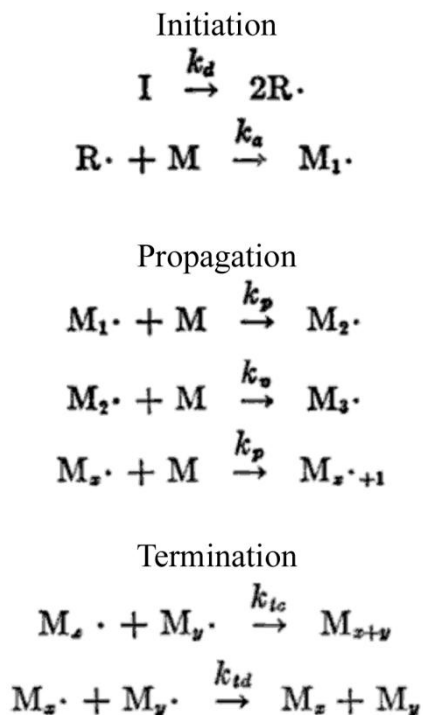
Figure 1.4. A generalized mechanism of free-radical polymerization. Adapted from ―Principles of Polymerizarion"[28]

1.2.1 Free Radical Photoinitiators

Photoinitiators for free-radical polymerizations need to be tailored for each material

system. The initiator must be stable within the monomer for long periods of time, it must highly

absorb at the incident wavelength, there must be efficient production of the initiating species, and

the initiating species must react with the monomer.[27]

There are three main photochemical routes that can lead to initiating species: photoscission reactions, hydrogen abstraction, and electron transfer followed by proton transfer.[30] Most free radical photoinitiators use photoscission or cleavage reactions to produce the radicals necessary for initiation. Many factors like added solvent, oxygen, or additives can greatly alter the rate constant of cleavage.[27]

Although the mechanism has not been determined, monomers in this work have been free-radical polymerized at 532 nm using a mixture of diiodofluorescein and 2,6-Diisopropyl-N,N-dimethylaniline (DIDMA). (Figure 1.5) The DIDMA most likely served as an electron transfer agent.[31] A commercially available mixture from BASF called Darocure 4265[32] was used for free-radical polymerizations at 365 nm.
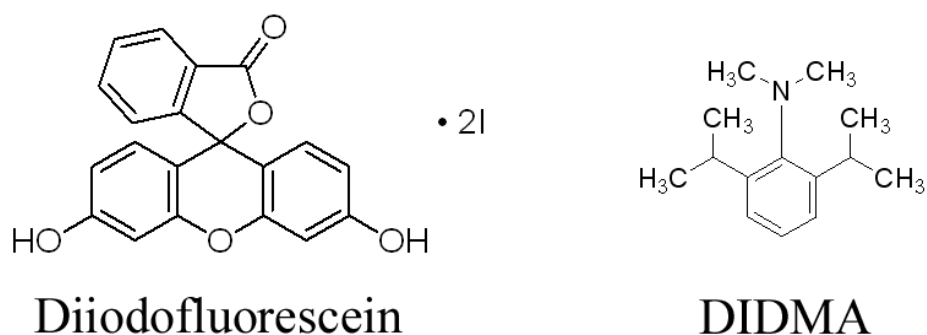
Figure 1.5. Chemical structures of diiodofluorescein and 2,6-Diisopropyl-N,N-dimethylaniline. (DIDMA)[33]

1.2.2 Cationic Photoinitiators

Cationic photoinitiation is dependent on the formation and propagation of an ionic species. Cationic polymerizations are less typical than free-radical polymerizations because the monomer must contain moieties that release electrons, and the reactions are highly dependent on solvent and impurities.[34] However for interference lithography, cationic polymerizations are preferred because laser exposure and polymerization are performed separately, which decreases distortions due shrinkage from polymerization. The most widely used cationic photoinitiators

8

belong to three classes: diazonium salts, onium salts, and organometallic complexes.[27] Diazonium salts form a Lewis acid when exposed to light, which opens an epoxide ring and rapidly polymerizes. Using diazonium salts as a photoinitiator typically causes pinholes or bubbles within the coating due to nitrogen evolution.[35-36] Onium salts are very efficient cationic photoinitators that photolysis into a cationic moiety and non-nucleophilic anion.[37-38] The cation controls the UV absorption and photosensitivity of the compound, while the anion controls the acid strength and initiation efficiency.[38] Organometallic complexes are good cationic photoinitiators for the visible spectrum. When irradiated, they generate a Lewis acid which causes epoxide polymerization.[27] Cyclopentadienyl(fluorene)-iron(II) hexafluorophosphate will be used as the photoinitiator for cationic polymerizations performed in this work. (Figure 1.6)

Figure 1.6. Chemical structure of Cyclopentadienyl(fluorene)iron(II) hexafluoro-phosphate.[33]

1.3 Photoresists

Photoresists are light sensitive materials composed of monomeric species that are typically spin-coated onto a substrate. When the appropriate wavelength of light exposes a photoresist, it causes a photochemical reaction that solublizes either the exposed or unexposed regions to a particular solvent. When the exposed photoresist is placed in the "developing" solvent, it washes away the solublized regions. The photoresist is defined as positive or negative based on whether the exposed region becomes soluble or insoluble in the developer. (Figure 1.7) Exposed regions of a positive resist become soluble in the developer, leaving the unexposed regions on the substrate. Unexposed regions of a negative resist become soluble in the developer,

9

leaving the exposed regions on the substrate. Every photoresist described in the following work will be a negative photoresist.
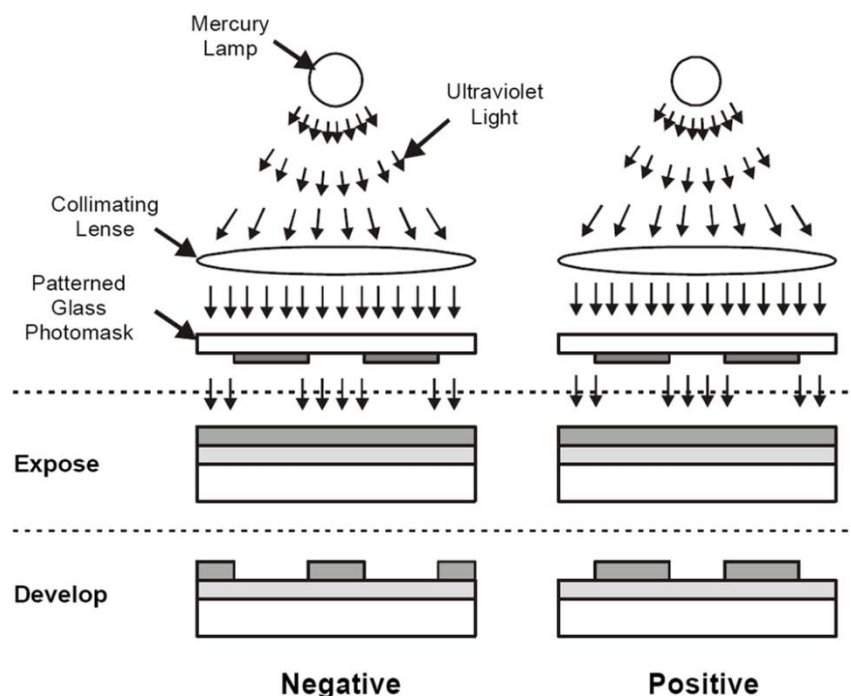
Figure 1.7. Schematic of the exposure and development of a negative and positive photoresist. Adapted from reference 39.[39]

1.3.1 Acrylate Based Photoresists

Acrylic resins were first synthesized in Germany around 1900 and they are known for their high transparency, weatherability, chemical resistance, and toughness.[40] Due to their favorable properties they are commonly used for finishes, adhesives, and coatings.[41] Photopolymerization of acrylate monomers occurs almost instantaneously through free radical polymerization, which allows for ultrafast drying of solvent-free resins.[42] Since acrylate monomers polymerize by free radicals, oxygen within the resin can inhibit or slow the rate of polymerization.[42] Many different acrylate monomers are commercially available, and the chemical structure of the monomer can be changed to enhance properties like water solubility,

mechanical toughness, stiffness, or number of crosslinks.   The chemical structures of the main

acrylate monomers used in this work are in figure 1.8.

Dipentaerythritol Pentaacrylate

Pentaerythritol Tetraacrylate

Pentaerythritol Triacrylate
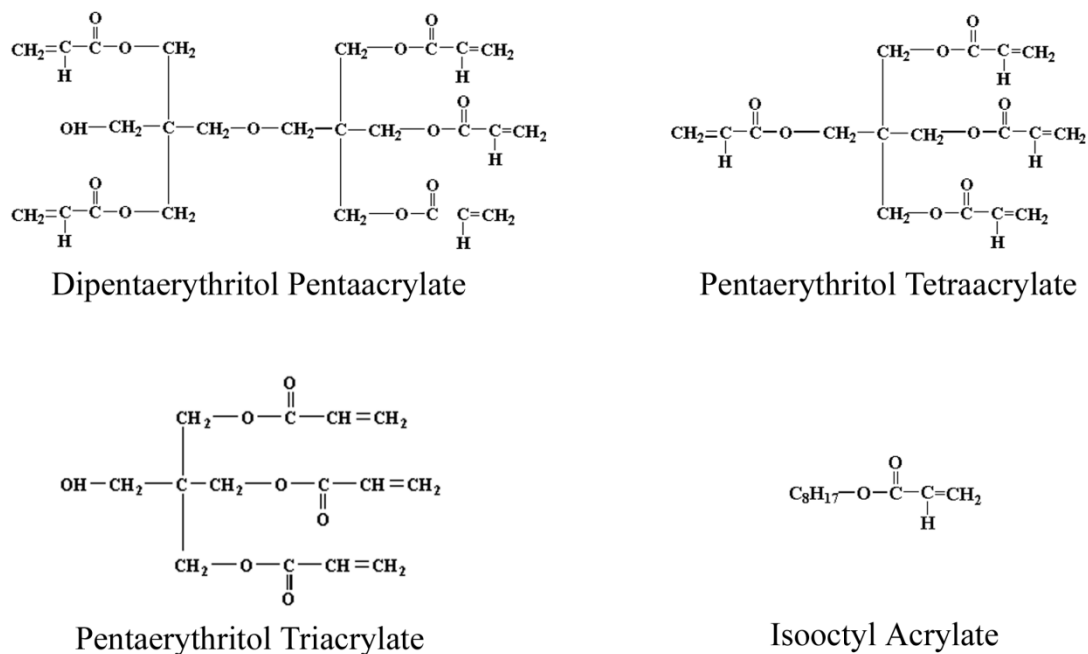
Isooctyl Acrylate

Figure 1.8. Chemical structures of common acrylate monomers: dipentaerythritol pentaacrylate, pentaerythritol tetraacrylate, pentaerythritol triacrylate, isooctyl acrylate.[43]

1.3.2 Thiol-ene Based Photoresists

The thiol-ene chemistry was first developed for large-scale photopolymerization by W.R.

Grace in the 1970's.[44-46] A thiol and alkene("–ene") monomer such as allyl ether, vinyl ether, or

acrylate are reacted in a step growth polymerization.[47] (Figure 1.9) Unlike the acrylate system,

thiol and "–ene" monomers must have a reactive functionality of at least two in order to form

polymer chains. Thiol-ene monomers have fewer oxygen inhibition problems than the acrylate

monomers and they typically undergo higher conversion rates, but thiol-ene monomers have

more problems with yellowing, odor, and cost.
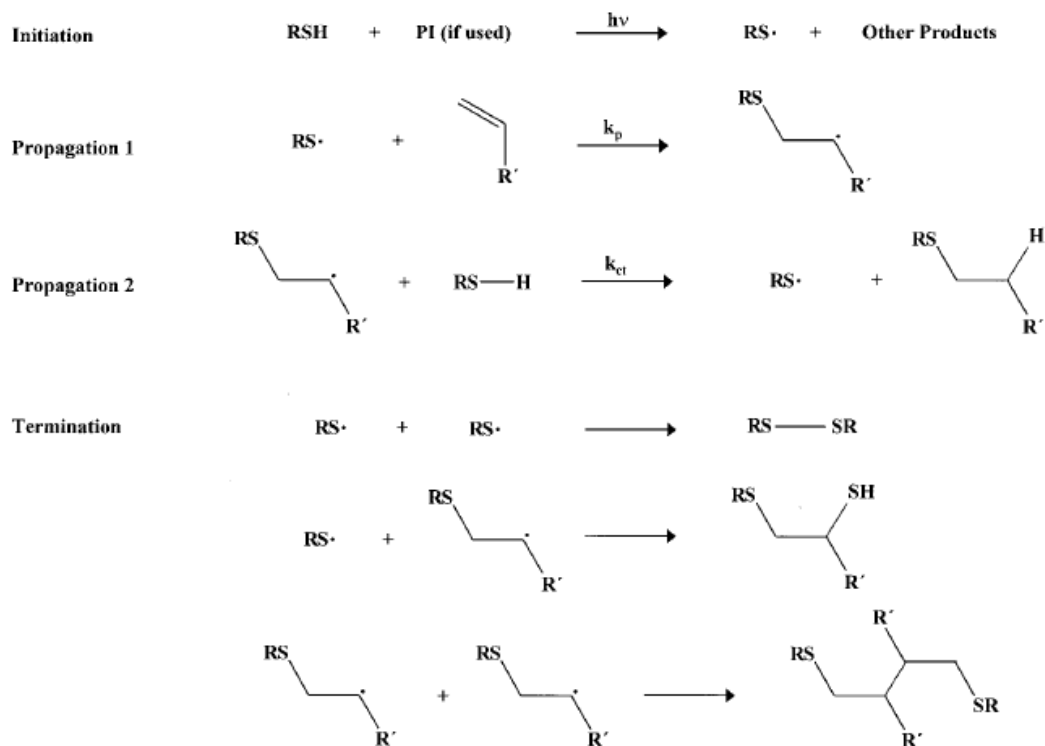
Figure 1.9. The general free radical step growth photopolymerization of a thiol-ene chemistry.[47]

1.3.3 SU8

SU8 is a very common epoxy-based, negative photoresist commercially provided by Microchem Corporation.[48] SU8 was designed for microelectronic applications, and is typically crosslinked by near-UV light (350-400 nm). However, the SU8 has been sensitized to green light, specifically 532 nm, by the addition of Cyclopentadienyl(fluorene)iron(II) hexafluoro-phosphate.[9] Figure 1.10 shows the absorption spectrum of a 1 micron thick film of SU8 sensitized with 2 w% Cyclopentadienyl-(fluorene)iron(II) hexafluoro-phosphate. The physical properties of SU8, as provided by Microchem Corporation, are in figure 1.11.
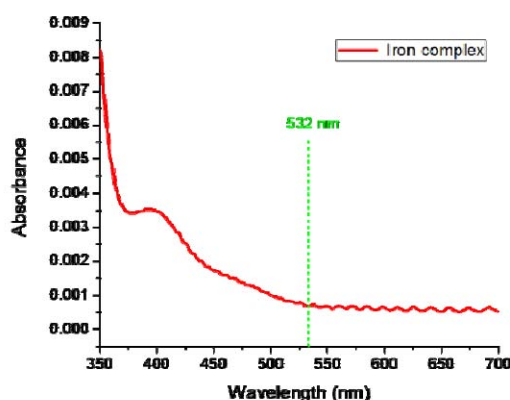
Figure 1.10. Absorption spectra of 1 μm of SU8 resin sensitized with 2 w% Cyclopentadienyl-(fluorene)iron(II) hexafluoro-phosphate. Figure provided by Dr. Ying-Chieh Chen.

Adhesion Strength (mPa) Silicon/Glass/Glass & HMDS	38/35/35
Glass Transition Temperature (Tg °C), tan δ peak	210
Thermal Stability (°C @ 5% wt. loss)	315
Thermal Conductivity (W/mK)	0.3
Coeff. of Thermal Expansion (CTE ppm)	52
Tensile Strength (Mpa)	60
Elongation at break (εb %)	6.5
Young's Modulus (Gpa)	2.0
Dielectric Constant @ 10MHz	3.2
Water Absorption (% 85°C/85 RH)	0.65

Figure 1.11. The physical properties of SU8 photoresist. Chart provided by Microchem Corporation.[48]

1.4 Polymerization Induced Phase Separation

When recording an interference pattern into a positive or negative photoresist, typically the portion of the sample that was either exposed or unexposed to the light becomes soluble and is developed away.   However, multi-component photoresists enable one- step fabrication by photopolymerization induced phase separation (PIPS).   In this method, a monomer, photoinitiator, and at least one other component are mixed together in ratios that allow for homogonous mixing. Upon application of light, the monomer begins to photopolymerize in the high intensity regions, and the volume fraction of monomer in the system reduces, causing the

13

homogeneous mixture to undergo phase separation. Due to this instability, the second component is usually sequestered into the regions of destructive interference. In this manner, periodic nanostructures consisting of more than one phase can be fabricated in one step. Figure 1.12 is a transmission electron microscopy (TEM) image of a grating formed by PIPS within a monomer and liquid crystal system. The liquid crystal droplets have been sequestered in to the low-intensity regions of the one dimensional interference pattern.[49]
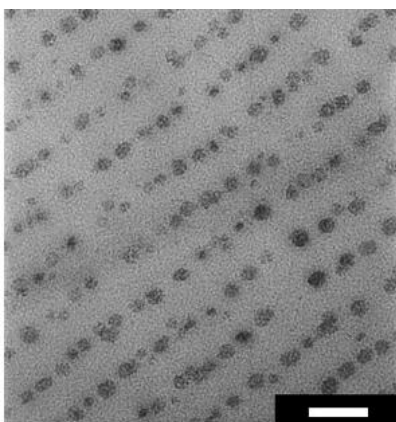
Figure 1.12. TEM image of a reflection grating formed by a photopolymerization induced phase separation with holographic polymer dispersed liquid crystals. Scale bar is 200 nm. Adapted from *Polymer* **2007,** *48* (20).[49]

1.4.1 Liquid Crystal Sequestration

Interference lithography and polymerization induced phase separation have been used for a variety of applications including nanoparticle assembly,[50-51] holographic films for data storage,[52-53] displays,[54-55] switchable gratings,[56-57] switchable lasers,[58] switchable microlenses,[59-60] and tunable photonic crystals.[61] In this thesis, systems that independently sequester nanoparticles, monomer, and liquid crystal into the low-intensity regions of the interference pattern will be reviewed and their applications will be discussed.

The most widely investigated example of this photopolymerization induced phase separation is in holographic polymer dispersed liquid crystals (HPDLCs), which start as a homogeneous mixture of monomer, free-radical photoinitiator and liquid crystal. Upon optical exposure, the monomer begins to polymerize in the regions of constructive interference, which reduces the solubility of the liquid crystal in those areas. This causes the liquid crystal to sequester into droplets in the regions of destructive interference.[62] The exact morphology and connectivity of these droplets is a function of both the exposure conditions and material system. Since the liquid crystal is birefingent and electrically tunable, it offers a way to electrically tune the refractive index within the device. With no electric field applied, the liquid crystal directors are in random orientations. Since at least one of the two incidences of refraction of the liquid crystal and the index of refraction of the polymer must differ, there will be some reflection of the incoming light. If an electric field is applied the liquid crystal directors, they become aligned. The materials can be engineered carefully so that the index of refraction of the liquid crystal for light polarized perpendicular to the director matches the index of refraction of the polymer; then light will propagate all the way through the material without being reflected. (Figure 1.13) A holographic polymer dispersed liquid crystal in the on and off state is shown in figure 1.14. Due to their ability to make optical devices active, PDLCs are typically used in displays,[54-55] switchable gratings,[56-57] switchable lasers,[58] switchable microlenses,[59-60] and tunable photonic crystals.[61]
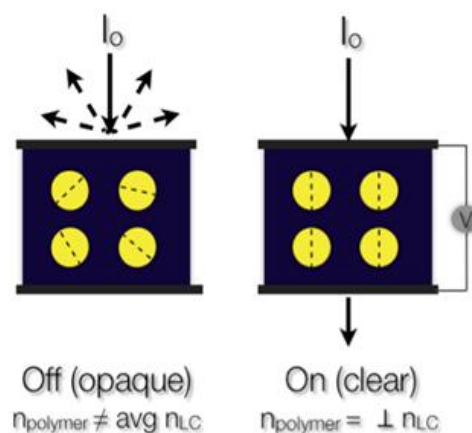
Figure 1.13. Schematic of a polymer dispersed liquid crystal in the off and on state. The liquid crystal directors are randomly oriented when there is no electric field, but they align when an electric field is applied. Light is reflected in the off state, but transmitted when the electric field is on.
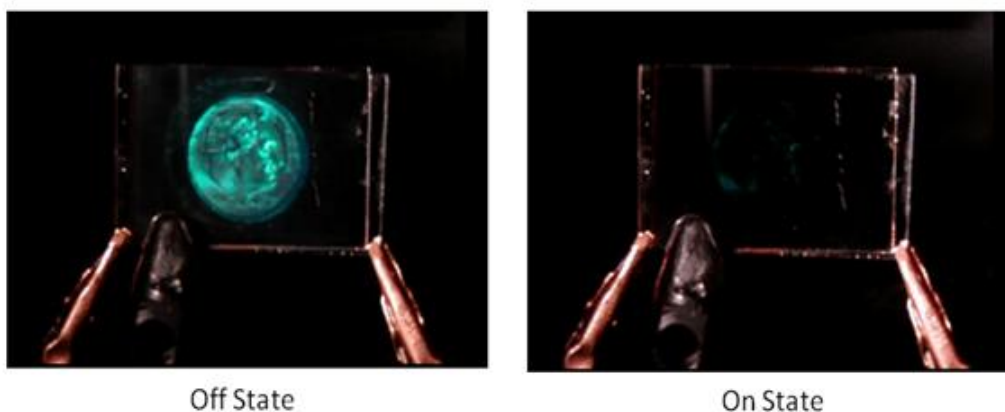
Figure 1.14. A typical HPDLC device. This device reflects blue light when no electric field is applied. It becomes transparent when an electric field is applied.[63]

1.4.2 Nanoparticle Sequestration

One way to create functional nanocomposites is by placing inorganic materials in higher or lower concentrations throughout the sample which can be easily achieved in two dimensions by many methods including nano-imprint lithography,[64] micro-contact printing,[65] and e-beam writing.[66] Extending this to three dimensions usually involves time-consuming multistep

processing, but it has been shown that a one-step method of interference lithography can be used to spatially design the position of nanoparticles within a three-dimensional polymer nanocomposite.[51] A nanoparticle/monomer mixture is used as a template into which a laser interference pattern is recorded. In the regions of constructive interference (high intensity), the monomer begins to polymerize. As monomer diffuses into this region and is added to the growing polymer, the nanoparticles diffuse towards regions of destructive interference. Eventually, the leftover monomers in the regions of destructive interference begin to polymerize and subsequently the nanoparticles are locked into place.

One example of using PIPS as a general method to assemble nanoparticles is shown in figure 1.15. Vaia et al. mixed a low volume fraction of 5 nm gold particles into an acrylate monomer and photoinitiator mixture. Upon photopolymerization, using a two beam laser setup with a wavelength of 532 nm, the monomer regions began to polymerize in the constructive interference regions which pushed the nanoparticles into the regions of destructive interference. The result was periodic lines of gold nanoparticles approximately a micron apart.[51] There are many other examples of using this method to assemble layered nanoparticles such as 260 nm polystyrene spheres, and clays.[51] Other groups have assembled zirconia,[67-69] titania,[68, 70-71] doped LaPO$_4$,[72] silica,[73-74] semiconductor,[75] and zeolite[76-77] nanoparticles. Not only does PIPS offer a one-step general method for efficient assembly of nanoparticles, the nanoparticles can also be used to engineer the periodic refractive index of the structure for optical applications such as photonic crystals.[78]
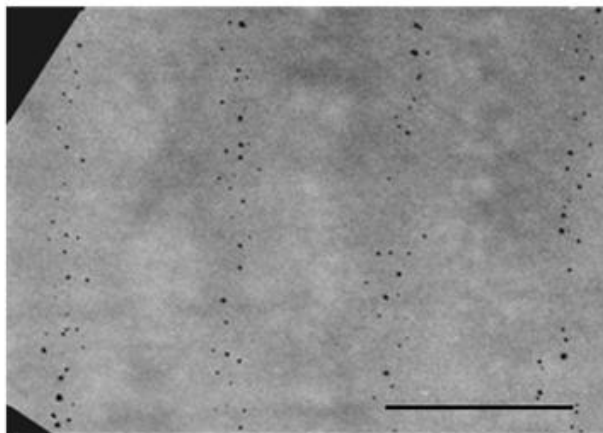
Figure 1.15. SEM of 5nm gold nanoparticles assembled into a 1D pattern of lines using photopolymerization induced phase separation. Scale bar is approximately 1 micron.[51]

1.4.3 Monomer Sequestration

Photopolymer systems are usually composed of thick photosensitive monomers that are precured into a partially polymerized gel state. Interference lithography is then used to impose a pattern onto the oligomeric resin. Depending on the intensity of the light, the monomer in the high intensity regions of the pattern will begin to polymerize, but due to the gelled state of the resin, free-radical polymerization will not occur in the low intensity regions. Instead the monomers that have not been polymerized will re-diffuse to an equilibrium state, leaving a periodic structure of monomer and polymer. (Figure 1.16) The monomer and polymer do not have the same index of refraction which generates a periodic change in the dielectric constant. This type of system is usually used for holographic data storage, since many interference patterns can be multiplexed throughout the recording medium.[52, 79]
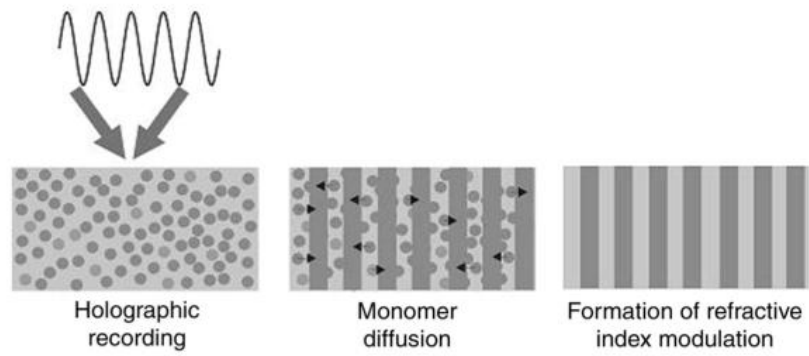
Figure 1.16 Method of using PIPS to periodically structure monomer and polymer for application in holographic data storage.[80]

CHAPTER 2

HOLOGRAPHICALLY DIRECTED ASSEMBLY OF POLYMER NANOCOMPOSITES[*]

2.1 Introduction

Nanocomposite materials have been shown to have advanced properties relative to conventional bulk polymeric systems,[81] however in almost all cases, the nanoscopic elements are randomly distributed; there has only been limited success in fabricating nanocomposites in which the nanoconstituent is arranged in a regular fashion.[78] Explicit control of the arrangement of matter in a nanocomposite material is important for both optical and electrical applications due to the fact that electrical and optical properties are very sensitive to the nanoscale arrangement of matter. It remains a major challenge to efficiently assemble nano-sized inorganic species into the complex, hierarchical structures often required for optically and electrically functional materials. Rigorous spatial control of materials in two dimensions can be achieved by many methods including nano-imprint lithography,[64] micro-contact printing,[65] and e-beam writing,[66] but extending this to three dimensions usually involves time-consuming multistep processing. Other techniques which can add structure to a nanocomposite system, including shear,[82] and external electric[83] or magnetic[84] fields require either inorganic moieties that lack translational symmetry or the use of a structured matrix, such as a block copolymer.[85] However, there is now promising evidence that a one-step holographic method can be used to spatially control the position of nanoparticles within a three-dimensional polymer nanocomposite.

Several years ago, Vaia *et al.*, demonstrated the formation of polymer nanocomposites containing periodic layers of 5 nm gold nanoparticles, 260 nm polystyrene spheres, and clays.[51] Other groups have assembled zirconia,[67-69] titania,[68, 70-71] doped LaPO$_4$,[72] silica,[73-74] semiconductor,[75] and zeolite[76-77] nanoparticles *via* holography. In all cases, nanoparticles are added into a mixture of monomer, photoinitiator, and coinitiator. Upon holographic illumination, the photoinitiator in the regions of high intensity forms radicals which initiate polymerization. Polymerization decreases the concentration of the monomers in the high intensity regions causing a net flux of monomers into that region. As the monomers react, the unreactive, mobile species move into the regions of low intensity (Figure 2.1). This movement of the monomers towards regions of constructive interference, and nanoparticles towards regions of destructive interference was shown experimentally by Tomita and Suzuki.[86-87]
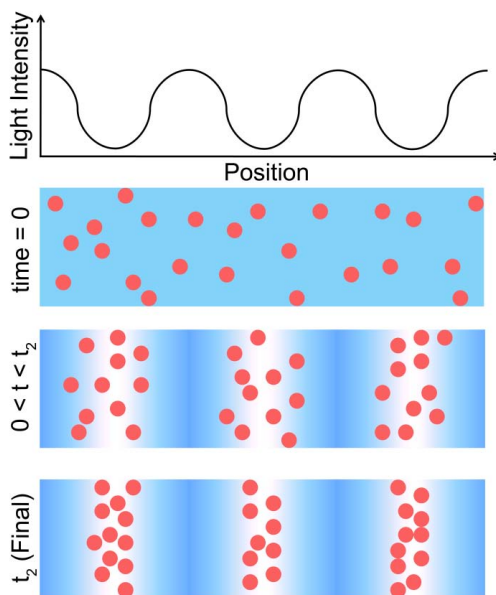
Figure 2.1. Spatial distribution of nanoparticles as a function of time when exposed to a periodically varying light intensity distribution. Before laser exposure at time (t) = 0, nanoparticles are homogeneously distributed throughout the sample. Polymerization is then induced by the optical interference pattern. The constructive interference regions of the sample polymerize first, leading to sequestration of monomer towards the high intensity regions and nanoparticles towards the low intensity regions (0 < t < t2). Photopolymerization eventually occurs even in the low intensity regions, locking the nanoparticles in place (t2= Final).

Tomita and Suzuki's phase shift measurement,[86-87] shows clearly that the nanoparticles move into the low intensity regions and monomer moves into the regions of high intensity. The mechanism for nanoparticle movement however is unclear. Possible reasons for nanoparticle transport include nanoparticle phase separation as monomer is polymerized, monomer transport into the polymerizing regions leading to sequestration of the nanoparticles into the low intensity regions (conservation of volume), and diffusion- limited mass transport in a matrix containing a gradient of polymerization kinetics. To determine the dominant mechanism, it is necessary to quantitatively determine the final nanoparticle positions as a function of exposure geometry, exposure time, exposure power density, grating periodicity, particle size, and nanoparticle concentration. Although a number of materials systems have been demonstrated *via* this method, the majority of the reports to date have only used diffraction efficiency to estimate the positions of nanoparticles within the photopolymer. However, Goldenberg *et al.* showed that the diffraction efficiency was not always a good predictor of nanoparticle sequestration.[88] In only a few systems have measurements of the spatially-varying nanoparticle concentration been obtained,[72, 76, 89-90] and only rarely have real-space images been obtained with sufficient resolution to show individual nanoparticles.[51, 88] In the work reported here, diffraction measurements are compared with corresponding transmission electron microscopy (TEM) micrographs to determine if the magnitude of the diffraction spots is a good predictor of nanostructure. We find that the magnitude of diffraction is altered by factors other than nanoparticle assembly, and thus only TEM was used to characterize nanoparticle assembly. We demonstrate the effect of exposure geometry, time, power density, periodicity, particle size, and nanoparticle concentration on final nanoparticle positions within the photopolymer, and from this determine the primary mechanism for nanoparticle sequestration is neither nanoparticle phase

separation due to conversion of monomer to polymer, nor conservation of volume as monomer diffuses into the polymerizing regions of the sample. The best nanoparticle sequestration occurred using low exposure power densities, short periodicities, and the smaller nanoparticles. Exposure time and nanoparticle concentration did not have a large effect on the final nanoparticle assembly. These results indicate that nanoparticle segregation is a diffusion-limited nanoparticle transport process, most likely driven by gradients in polymerization kinetics under holographic illumination, and guided by Stokes-Einstein dynamics.

2.2 Fabrication

2.2.1 Silica Nanoparticle Synthesis

25 nm silica particles were prepared by mixing 240 mL ethanol (Decon Laboratories INC, cat # 2701), 3 mL deionized water, and 6 mL ammonium hydroxide (Aldrich, cat# 329145). Under rapid stirring, 6 mL of tetraethyl orthosilicate (TEOS, Fluka cat# 86578) were added quickly into the mixture and left to stir for 24 hours.

50 nm silica was prepared very similarly, but the volume fractions (mL) of ethanol, DI water, ammonium hydroxide, and TEOS were changed to a volume ratio of 245: 3.8: 8.5: 7.7 respectively. After 24 hours of stirring, the silica nanoparticles were placed into 12,000 MW dialysis membranes (Fisher, cat# 08667E) and placed into a pure ethanol bath. This bath was changed every five hours at least four different times to remove any excess water and ammonium hydroxide not consumed in the reaction.

2.2.2 Polymer Matrix Formulation

A study of the fundamental mechanism for the holographic nanoparticle assembly required development of a silica nanoparticle containing system that would not aggregate under the various experimental conditions. Previous systems incorporating mixtures of multifunctional

23

and monofunctional acrylates such as SR399 and isooctylacrylate were considered,[72] but the unfunctionalized 25 nm silica nanoparticles aggregated in these systems. The other system developed by Tomita was not commercially available and therefore not considered.[89] A new experimentally simple system was developed containing the monomers pentaerythritol triacrylate (PETA) and 1-vinyl-2-pyrrolidinone (NVP), silica nanoparticles, and photoinitiator. The bare silica nanoparticles disperse within the PET/NVP mixture.

0, 6.8, 12.8, or 22.7 w% silica particles in ethanol were added into 0.35 g of Pentaerythritol triacrylate (Aldrich, cat# 246794). The ethanol was rotovaped from the mixture, and immediately following, 0.2 g of 1-Vinyl-2-pyrrolidinone (NVP, Aldrich, cat# V3409) were added to reduce the viscosity. The photoreactive mixture was then vortexed and sonicated in a separate container in the dark. It consisted of 0.01 g diiodofluorescein (Aldrich, cat# 206806), 0.1 g NVP, 0.01 g 30 μm glass spheres, and 0.02 g 2,6-Diisopropyl-N,N-dimethylaniline (Aldrich, cat# 550698). This photoreactive mixture was then added into the monomer containing the nanoparticle solution. This mixture was sandwiched between two glass slides using 30 μm glass spacers to give the syrup a uniform thickness.

2.2.3 Laser Setup

A 532 nm continuous wave Nd:YVO4 Coherent Verdi laser (5 Watt) was used to photopolymerize the mixture of monomer and silica nanoparticles.   The geometry of the laser interference pattern imparts the final morphology of the nanoparticles within the monomer matrix; therefore, a two beam interference pattern with one-dimensional periodicity was chosen for the sample geometry because it simplified sample characterization. The pattern could be fabricated in reflection mode with alternating intensity planes parallel to the substrate, or in transmission mode with alternating intensity planes perpendicular to the substrate (Figure 2.2).

In this chapter, all of the samples were fabricated in the transmission geometry, because it

allowed the diffraction efficiency of the transmission grating to be monitored by another laser

throughout the writing of the sample.
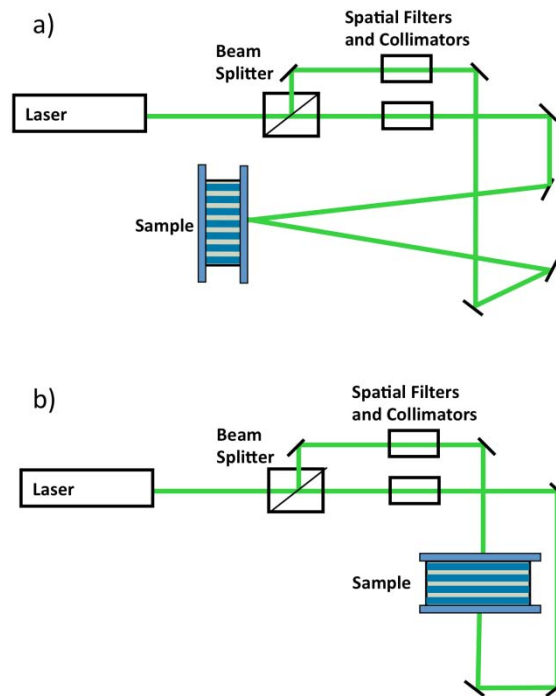
Figure 2.2. Schematic of laser geometry for fabrication of a a) Bragg transmission grating or b) Bragg reflection grating.[91]

The periodicity of the interference pattern is defined by the wavelength of the coherent

light source and by the angle between the propagating wave vectors as illustrated in Figure 2.3.[92]

The grating will be blazed (tilted planes) unless both beams hit the substrate at the same angle,

meaning the laser set-up is perfectly symmetric.
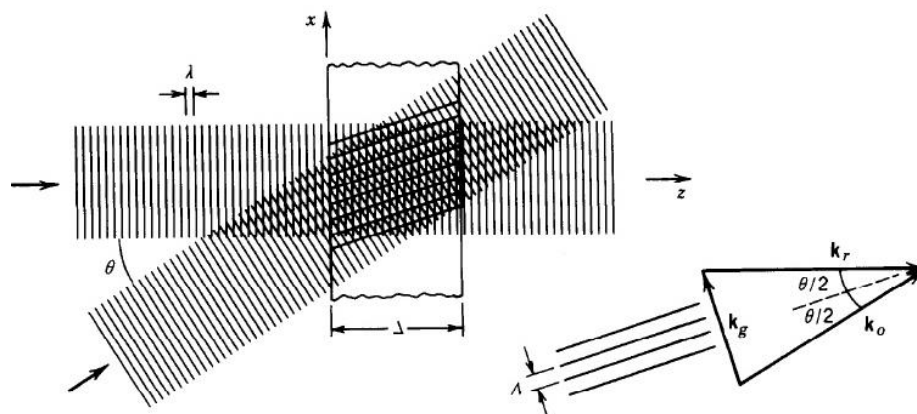
$$Periodicity \ (\Lambda) = \frac{Wavelength \ (\lambda)}{2 * \sin \left(\frac{\theta}{2}\right)}$$

Figure 2.3. Schematic representation of the interference of two laser beams in transmission geometry, and a formula describing the resulting periodicity of the high intensity light planes.[92]

In the following work, the angle between the two beams was approximately 30 degrees resulting in about a 1 micron periodicity. The exposure power density was set between 0.035 mW/cm^2 and 200 mW/cm^2 per beam.

2.3 Characterization of Assembled Nanocomposites

2.3.1 Microtoming and Transmission Electron Microscopy

Holographically photopolymerized samples containing silica nanoparticles were microtomed in 90 nm sections using a Leica Ultramicrotome, and then characterized using a Philips CM200 TEM. Figure 2.4a is a TEM micrograph of a sample consisting of 12.8 w% 25 nm diameter silica particles, 44.9 w% PETA, 38.5 w% NVP, and 3.8 w% photoinitiator that was polymerized using two-beam interference from a 532 nm laser. The nanoparticle concentration has been increased to 22.7 w% silica in Figure 2.4b. Each sample was exposed for 300 seconds with each beam having a power density of 200 mW/cm^2. High and low density silica

nanoparticle layers are apparent, and the pitch of the layers was slightly larger than 1 μm, matching the pitch of the interferogram.
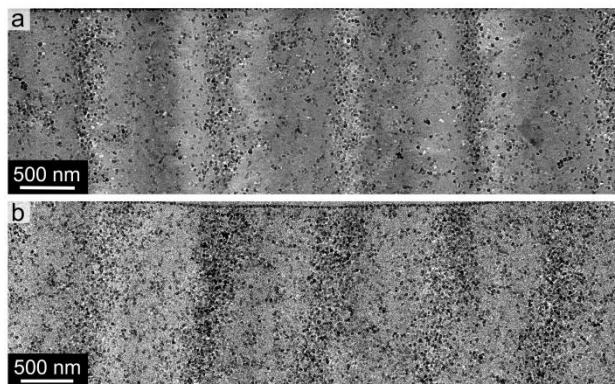
Figure 2.4. TEM micrographs of holographically photopolymerized samples containing (a) 12.8 w% and (b) 22.7 w% 25 nm SiO_2 using a 300 sec 2-beam exposure at 200 mW/cm^2 per beam.

2.3.2 Diffraction

To determine the magnitude of diffraction during the writing of the Bragg grating, a HeNe laser was placed normal to the sample and the power of the resulting first order Bragg diffraction peak was measured and normalized to the zeroth order peak. The zero and first order diffraction peaks were measured and recorded every 0.25 sec. Diffraction magnitude was determined by dividing the intensity of the first order diffraction peak by the sum of the zero and first order peaks. The diffraction curve of the 500 nm sample was not measured as a function of time as it was trapped by total internal reflection.

Diffraction measures the index contrast between periodic alternating layers of material. The silica particles have an index of refraction (n) of ~1.46 which is similar to that of the monomers, n~1.5. With this low of an index contrast, a high intensity diffracted beam is not expected, but it is still interesting to consider if the magnitude of the diffracted beam can be used to characterize the degree of nanoparticle assembly. To determine if diffraction is a good predictor of nanoparticle assembly, the magnitude of the diffraction from the +1 order and 0th

order was monitored while writing the hologram into samples containing various nanoparticle concentrations, and correlated to the TEM determined nanoparticle distribution. Diffraction curves of samples containing different nanoparticle concentrations can be seen in figure 2.5a. Over the first few seconds there is a rapid increase in the diffraction magnitude followed by a steady decrease, which has been attributed to slow polymerization of monomers in the darker regions of the sample.[93] We did not always see a decrease in the diffraction curve, this was the case for example when exposures were done at low power densities or with high nanoparticle concentrations (> 20 w%). Most germane to the discussion here, however, is that the magnitude of the diffraction was virtually the same for samples containing either 6.8 w% agglomerated nanoparticles or 12.8 w% non-agglomerated nanoparticles. The agglomerated nanoparticles do not assemble into regions of destructive interference, while the 12.8 w% assemble as expected (Figure 2.5b-c). If diffraction magnitude was a strong function of nanoparticle assembly, the diffraction curves of these two samples should be significantly different. This was not the case. The diffraction magnitude in both samples is probably caused by monomer segregation due to differences in their polymerization rates. Stumpe *et al.* showed that monomers that polymerize more slowly are sequestered into the regions of destructive interference just as our nanoparticles are,[88] and this is probably the origin of the diffraction magnitude in our samples. To evaluate the maximum contribution of the nanoparticles to the diffraction curve, the diffraction magnitude as a function of time was recorded for a nanoparticle free sample (Figure 2.5a). At most, a 10% change in diffraction magnitude can be attributed to the addition of nanoparticles. The 10% diffraction magnitude change may not even be completely due to nanoparticle assembly, as it has also been shown that the nanoparticles can promote polymer segregation as well.[88] Therefore, diffraction will not be used to characterize the assembly of nanoparticles since other non-

nanoparticle effects can alter the absolute magnitude of the measurement. The shape of the diffraction curve can be used to investigate the kinetics of the photopolymerization, but the final positions of the nanoparticles should be determined using a different approach, for example TEM.
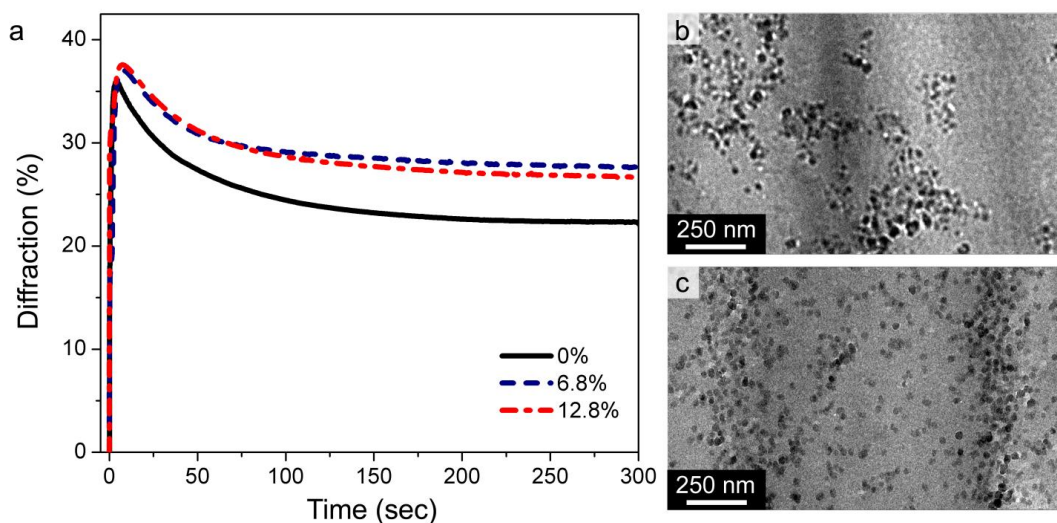
Figure 2.5. (a) Diffraction intensity of the first order diffraction peak dividied by the sum of the zero and first order peaks as a function of exposure time for different concentrations of nanoparticles. (b-c) Corresponding TEM micrographs of samples containing 6.8 and 12.8 w% 25 nm SiO_2 nanoparticles, respectively. The 12.8 w% sample shows nanoparticle assembly while the 6.8 w% sample only shows agglomerations.

2.4 Possible Mechanisms for Nanoparticle Assembly

2.4.1 Polymer/Nanoparticle Miscibility Mechanism

With a stable nanoparticle containing photopolymerizable system, coupled with TEM characterization, it was possible to study the fundamental mechanism for nanoparticle sequestration. One possible driving force for nanoparticle assembly is a decrease in the ‗miscibility‗ of the nanoparticles as monomer is converted to polymer. If this mechanism dominates, then a flood lit exposure is expected to show large particle aggregations. Figure 2.6 is a TEM image of a flood lit exposure of a sample containing 12.8 w% 25 nm diameter silica

particles, 44.9 w% PETA, 38.5 w% NVP, and 3.8 w% photoinitator that was polymerized for 300 seconds using one beam from a 532 nm laser with a power density of 400 mW/cm^2. These exposure conditions were chosen to match the average power density of the sample shown in figure 2a, so single-beam and interferometric exposures could be directly compared. There may be minor agglomerations in the silica nanoparticles of the flood-lit sample, but the density of the aggregations is not sufficient to account for the nanoparticle assembly indicating nanoparticle immiscibility is not the dominant mechanism for nanoparticle sequestration.
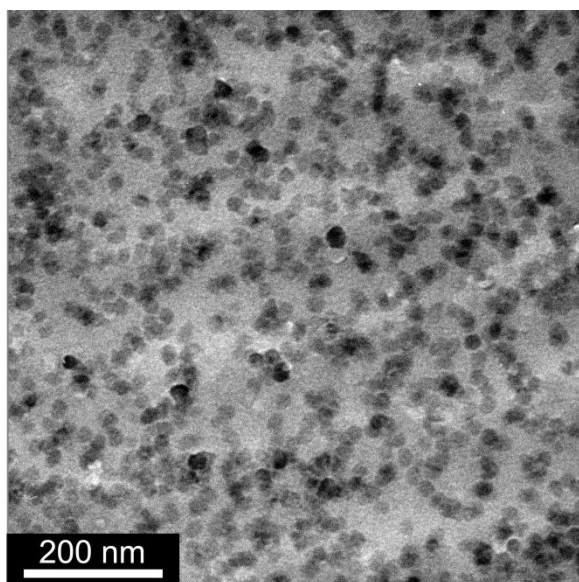
Figure 2.6. TEM image of a flood lit exposure of a sample containing 12.8 w% 25 nm diameter silica particles, 44.9 w% PETA, 38.5 w% NVP, and 3.8 w% photoinitator that was polymerized for 300 seconds using one beam from a 532 nm laser with a power density of 400 mW/cm^2.

Although we do not attribute the primary mechanism to liquid-gel demixing, the frontal nature of the polymerization process may cause a similar type of phase separation. If a liquid-gel front moves through the sample it could essentially _sieve' the nanoparticles into the regions of low-intensity light. A flood exposure creates a uniform gelation without a liquid-gel front, so this mechanism would not result in regions of high density particles. However, for the sinusoidal interferogram we impose on the sample, we expect the result of this mechanism to be more

binary, that is, we would expect significant aggregations of nanoparticles in low intensity light regions and almost no particles in high intensity regions, rather than the smooth gradient in the nanoparticle density across the period seen in Figure 2.4. We would also expect this mechanism to work at long length scales, which does not occur as we show later.

2.4.2 Monomer Transport Mechanism

Another possible mechanism for nanoparticle assembly is that nanoparticles are effectively pushed into the regions of destructive interference to conserve volume as the monomers diffuse towards the regions of high intensity light and polymerize. To test this hypothesis, the assembly of 25 nm and 50 nm particles was compared. If monomer transport dominates nanoparticle assembly, and thus particle size and particle mobility are no longer important, then 25 and 50 nm particles should assemble under similar photopolymerization conditions. At an exposure power density of 400 mW/cm^2, the 25 nm silica particles sequestered into the regions of destructive interference, but the 50 nm particles did not show any structuring (Figure 2.7). To assemble the larger particles, the power density had to be reduced to 0.07 mW/cm^2. This suggests nanoparticle assembly is a function of particle mobility, rather than monomer transport. If monomer transport to the polymerizing regions is not the driving force for nanoparticle assembly, then nanoparticle assembly can only occur while the viscosity of the matrix is low enough to allow particle motion. In our system, a three-dimensional network of branched polymer chains forms, leading to a point in which the matrix gels and diffusion can no longer occur. This gel point probably occurs within the first few seconds of exposure at 400 mW/cm^2. Since the 50 nm particles move more slowly than the 25 nm particles, a longer time was needed for nanoparticle sequestration before matrix gelation. Decreasing the power density slowed the polymerization kinetics enough to allow the larger particles to assemble. Due to light

scattering by the 50 nm particles, nanoparticle assembly only occurred near the surface of the sample; however, this is only a practical problem and not something that impacted our analysis. In comparing the TEM images of the 25 and 50 nm samples in figures 2.7a and 2.7b, there is an obvious change in the appearance between the high and low intensity regions sample. We suspect that the microtoming of the sample containing larger particles into 90 nm thick sections left holes within the destructive regions of the sample. The positions of the nanoparticles were measured from the TEM micrographs and plotted in figure 2.7c. A quantitative understanding of the nanoparticle segregation was obtained through image analysis on each of the TEM micrographs as outlined in Figure 2.8. Each nanoparticle on the micrograph was treated as a 25 or 50 nm circle, and the effective aerial particle density was measured using ImageJ and plotted against position (Figure 2.7c). The samples were 90 nm thick so nanoparticles can overlap in the TEM micrograph. Overlapping particles were not counted, so the number of nanoparticles, primarily in the high intensity regions, is artificially low. To demonstrate that the TEM micrograph in Figure 2.7a is representative, 5 TEM micrographs from different positions on sample 2.7a are added in Figure 2.9.
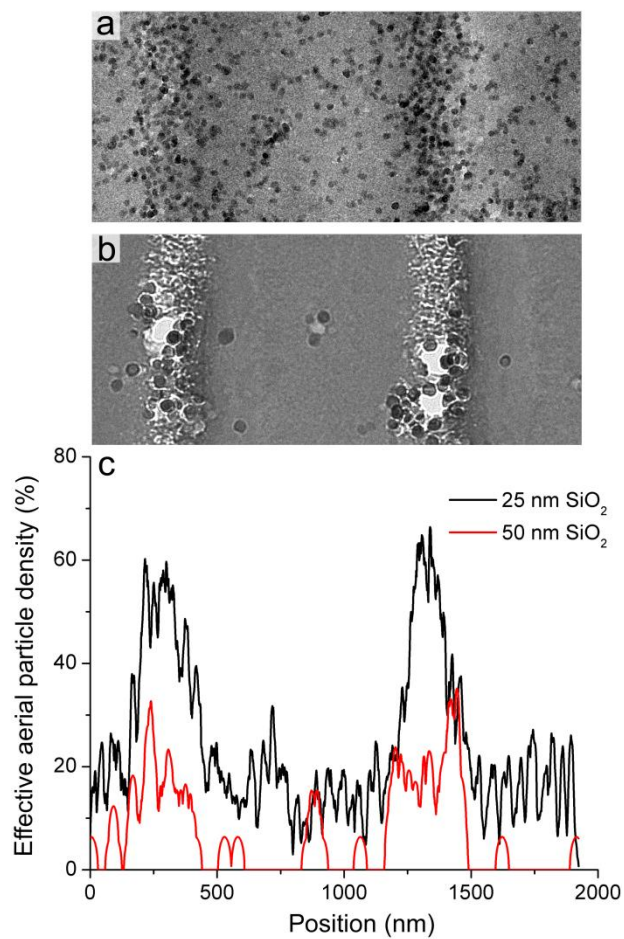
Figure 2.7. (a-b) TEM micrographs of samples containing 12.8 w% SiO_2 photopolymerized for 300 seconds (a) 25 nm SiO_2 at an exposure power density of 400 mW/cm^2 and (b) 50 nm SiO_2 at an exposure power density of 0.07 mW/cm^2. (c) Graph of the effective aerial nanoparticle density as a function of position extracted from a and b. The x-axis in (c) is to scale with both TEM micrographs.
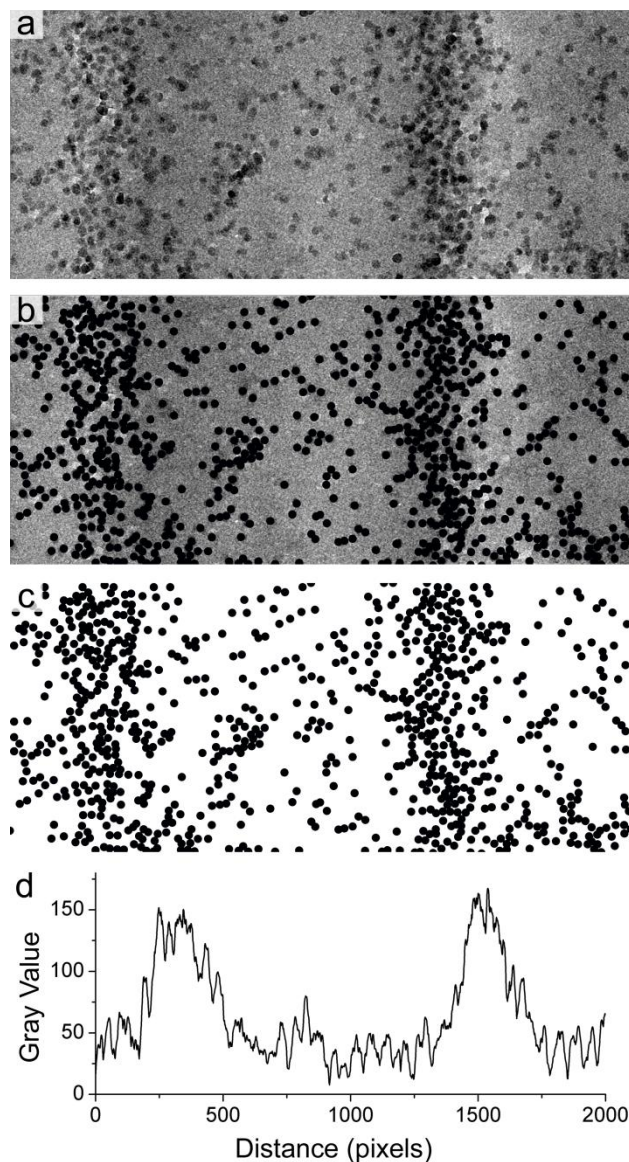
Figure 2.8. Example of the process used to determine aerial nanoparticle density. (a) Original TEM micrographs were imported into Adobe Photoshop and cropped to 1923 nm by 828 nm. (b) Black circles corresponding to the nanoparticle diameter (25 or 50 nm) placed onto each nanoparticle. (c) The background was then deleted and the dots were placed on a white background. (d) The images with black dots on a white background were then imported into ImageJ and the colors were inverted. The images were then analyzed using ‚plot profile', and the grey value was graphed versus distance (in pixels). The grey value was then divided by the total number of pixels to get aerial nanoparticle density, and the pixel number was then correlated to the actual length of the TEM micrograph.
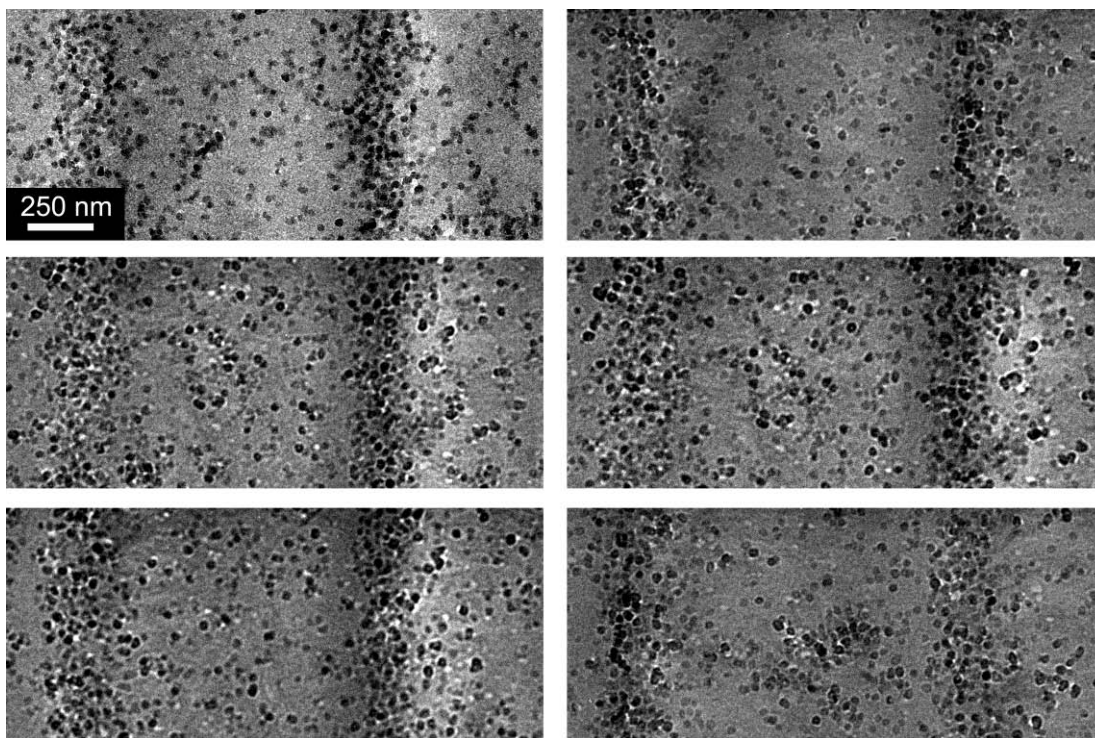
Figure 2.9. Six TEM images of different regions of a sample containing 12.8 w% 25 nm SiO_2 photopolymerized for 300 seconds (~1 μm periodicity) at an exposure power of 400 mW/cm^2, demonstrating that the TEM micrographs in the paper are representative.

2.4.3 Diffusion-Limited Mass Transport Mechanism

Based on the experiments with different size nanoparticles and the lack of aggregation under flood exposure, we suggest nanoparticle sequestration is primarily based nanoparticle transport in a matrix containing a spatially varying gradient of polymerization kinetics. As the matrix polymerizes and gels in the high field region, movement of nanoparticles towards that region should be greatly suppressed, while transport away from that region should remain allowed. To confirm this hypothesis, the exposure time, power density, and periodicities were varied to study the effects on the final nanoparticle assembly. Exposure times ranged from 6.75 to 300 sec, the exposure power densities ranged from 1.6 to 300 mW/cm^2, and the interferogram spacings were 0.5, 1, and 2 μm.

Assuming diffusion- limited mass transport is the primary mechanism for nanoparticle assembly, exposure time should only effect nanoparticle sequestration if the laser interferogram is turned off before gelation has locked the nanoparticles in place. The effect of exposure time on the final nanoparticle positions was studied via TEM to obtain a qualitative understanding of the temporal evolution of the nanoparticle positions. Figure 2.10a is a TEM micrograph of a sample exposed holographically for 6.75 sec. Despite the short exposure time, there are still definite high-density regions of 25 nm silica particles periodically spaced about a micron apart, and the overall structure is similar to a sample exposed for 300 sec. (Figure 2.10b). The spatial distribution of nanoparticles in both images is nearly identical (Figure 2.10c). The aerial particle density for figure 2.10b was determined for 5 separate TEM micrographs of the same sample for a total of 10 regions of high nanoparticle density. The aerial particle density peaks at ~67.4% with a standard deviation of 5.75% in regions of low intensity, and 15-20% in the regions of high intensity. Most of the nanoparticle sequestration must occur in the first 6.75 seconds, and further increases in exposure time, despite the fact that some of the monomer has not polymerized at 6.75 sec., do not have an effect on the final nanoparticle positions, supporting the hypothesis that the nanoparticle movement is driven by particle transport away from the polymerization front, and not monomer diffusing into the polymerizing region.

Figure 2.10. (a-b) TEM micrographs of samples containing 12.8 w% 25 nm SiO$_2$ photopolymerized at 400 mW/cm^2 (~1 μm periodicity) for (a) 6.75 seconds and (b) 300 seconds. (c) Graph of the effective aerial nanoparticle density as a function of position extracted from (a) and (b). The x-axis in (c) is to scale with both TEM micrographs. (d-e) TEM micrographs of samples containing 12.8 w% 25 nm SiO$_2$ photopolymerized for 300 seconds (~1 μm periodicity) at an exposure power density of (d) 1.6 mW/cm^2 and (e) 400 mW/cm^2. (f) Graph of the effective aerial nanoparticle density as a function of position extracted from (d) and (e). The x-axis in (f) is to scale with both TEM micrographs.

If nanoparticle transport away from the polymerizing regions is limited by biased Brownian motion,[94] lowering the exposure power density should slow the polymerization rate and increase the time before gelation. Therefore, samples exposed at lower power densities should have better nanoparticle sequestration. The effect of exposure power density was investigated using interferograms with a total power density of 1.6 and 400 mW/cm^2, figures 2.10d and 2.10e, respectively. As expected, both power densities provided alternating layers of high and low density SiO$_2$. The nanoparticle effective aerial particle density was measured as a function of position (Figure 2.10f). The lower power density exposure generated a greater degree of nanoparticle sequestration as shown by the fact that there were fewer nanoparticles in

37

the high intensity regions. The effective aerial density of the low power density sample nearly reaches zero density in the high intensity regions, while in the high power density sample it remains above 10%. Very few nanoparticles remained in the high intensity regions of the lower exposure power density sample, presumably because they had time to segregate into the low intensity regions before they were trapped by gelation of the matrix.

If we assume that transport of nanoparticles is diffusion- limited, then lowering the exposure power density should slow the reaction rate and give more time for nanoparticle sequestration. As just demonstrated, when an exposure power density of 1.6 mW/cm^2 was coupled with a long exposure time (300 sec), nanoparticle assembly occurred. But if the lower exposure power density was coupled with a short exposure time, would the samples still sequester? A sample with 12.8 w% 25 nm SiO$_2$ was photopolymerized at 1.6 mW/cm^2 for 6.75 seconds with a 1 μm periodicity (Figure 2.11). The effective aerial particle density was determined and plotted versus position. Although the sequestration was not as strong as for as the sample exposed for 300 sec, it is clear that nanoparticle assembly occurs rapidly even under low exposure power densities.
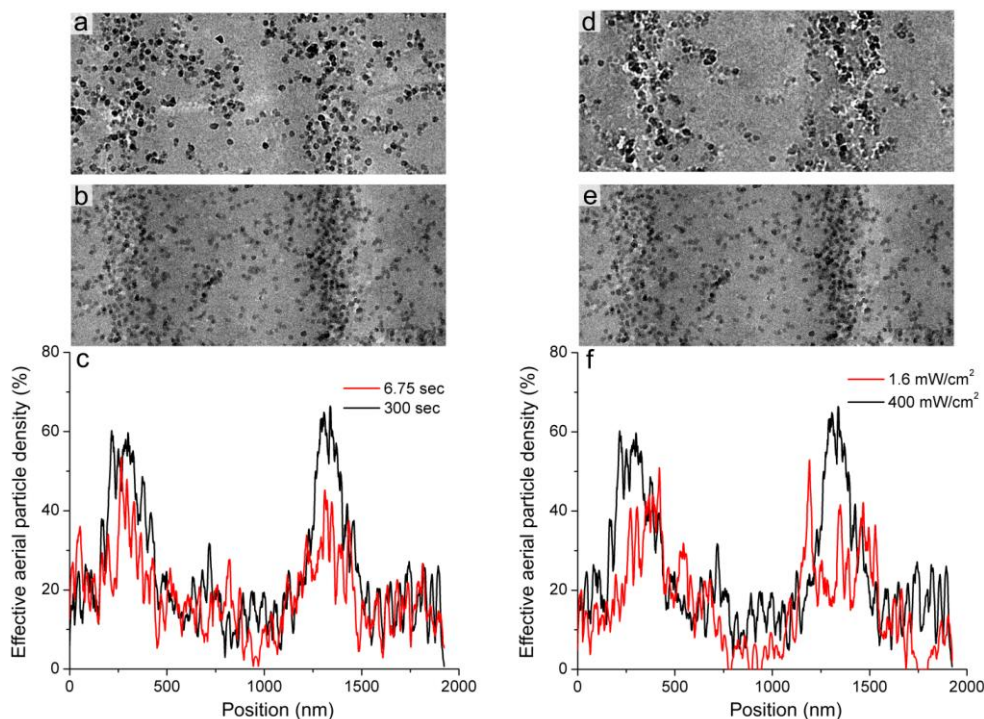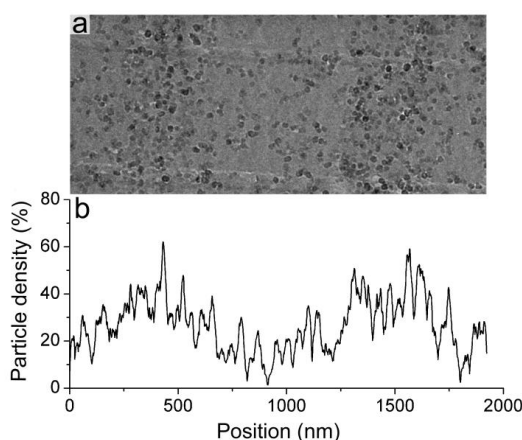

Figure 2.11. (a) TEM micrograph of a sample containing 12.8 w% 25 nm SiO$_2$ photopolymerized at 1.6 mW/cm^2 (~1 μm periodicity) for 6.75 seconds. (b) Graph of the effective aerial nanoparticle density as a function of position extracted from (a).

Finally, if the nanoparticles must move through the polymerizing matrix into the regions of low-intensity, then there should be a maximum hologram periodicity after which the nanoparticles could not move the distance necessary before gelation locks them in place. Smaller periodicities should show better sequestration since the particles have the same time to diffuse a shorter distance. To test this assumption, the periodicity was reduced from about 1 μm to 500 nm by increasing the angles of incidence of the interfering beams. Figure 2.12a is a TEM micrograph of the sample with 500 nm periodicity. Relative to samples with 1 μm periodicity exposed using similar conditions (Figure 2.12b) there are very few nanoparticles within the constructive interference regions of the 500 nm sample. The nanoparticles in the 500 nm periodic sample had the same amount of time to move before gelation as did the 1 um periodic sample, but the silica did not have to move as far to reach the low-intensity regions. More of the nanoparticles in the sample with small periodicity were displaced to their appropriate positions before gelation locked them in place. As the periodicity was increased to 2 microns (Figure 2.12c), the nanoparticles did not diffuse into the low intensity regions and the nanoparticle density does not seem to fluctuate with position. As expected, best nanoparticle sequestration occurs at smaller periodicities.
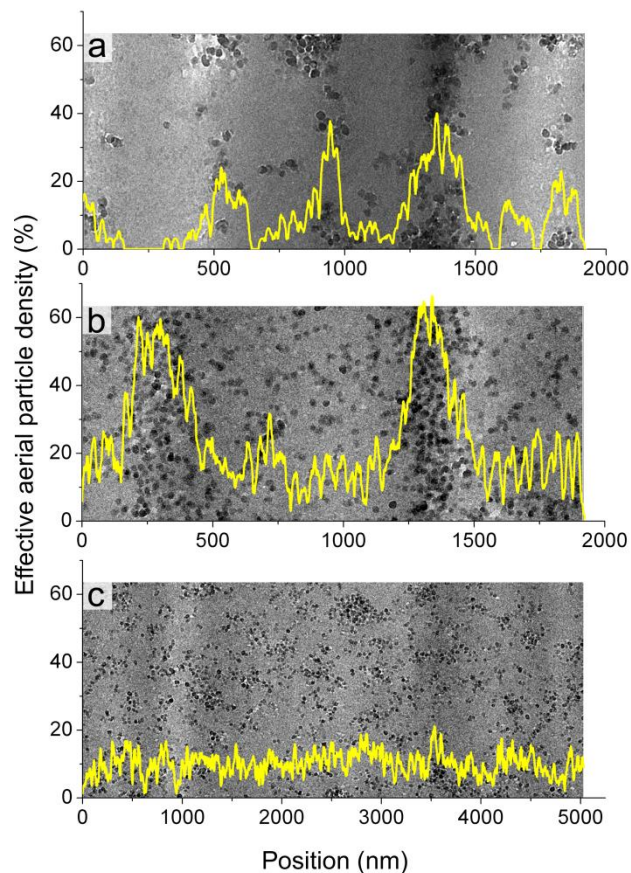
Figure 2.12. TEM micrographs of samples containing 12.8 w% 25 nm SiO_2 photopolymerized for 300 seconds at an exposure power density of 400 mW/cm^2 at periodicities of (a) 500 nm, (b) 1000nm, and (c) 2000nm. The effective aerial nanoparticle density as a function of position is plotted over each micrograph. The x-axis is to scale for each TEM micrograph.

2.4.3.1 Stokes-Einstein Predictions

To help understand the limits of nanoparticle transport within our system, Stokes-Einstein dynamics were compared to experimental observations. The viscosity of the nanoparticle/monomer resin before polymerization was measured at 0.07 Pa*sec using a parallel plate rheometer. Assuming that nanoparticle transport is governed by Stokes-Einstein diffusion, the diffusion constant of the nanoparticles in the photo-curable resin can be estimated at 0.25 μm^2/sec. The Stokes-Einstein diffusion constant was determined by:

$$D = \frac{k_B T}{6\pi\eta r}$$

Where k_B is Boltzmann's constant, T is temperature (295K), η is viscosity, and r is the radius of the nanoparticle (12.5 nm). To estimate the distance that the nanoparticles can diffuse before gelation, the following equation was used:

$$\text{Distance Diffused} = \sqrt{Dt}$$

t is a measure of time before gelation which was assumed to be 1- 4 seconds, giving an estimated diffusion distance of 0.5 − 1 μm. This is most likely greater than the actual value because it does not account for the increase in viscosity before gelation, which increases exponentially with time.[95-96] The maximum diffusion distance observed was approximately 0.5 μm (Figure 9c), which is in reasonable agreement with the Stokes-Einstein predictions.

2.5 Conclusions and Future Directions

The holographically defined assembly of nanoparticle-polymer composites was studied using a new nanocomposite system. In this system, the magnitude of the diffraction was not a good indicator of the actual structure, so TEM imaging was used to evaluate the degree of nanoparticle assembly. The mechanism for nanoparticle movement was studied by changing exposure geometry, exposure time, exposure power density, nanoparticle size and periodicity. The primary mechanism for nanoparticle assembly was determined to be diffusion- limited nanoparticle transport in an optically defined gradient of polymer density. This is supported by the fact that exposure time did not affect the resulting structure, while lowering exposure power density, decreasing nanoparticle size, and smaller interferogram periodicity all gave better nanoparticle sequestration. Stokes-Einstein dynamics were a good guide for determining maximum nanoparticle diffusion distances. Although the low-contrast system may not be

pertinent to applications which require high diffraction efficiencies, it does explicitly highlight the relationship between the kinetics of the polymerization and the structures formed in polymerization-induced nanoparticle assembly.

CHAPTER 3

NANOPARTICLE SYNTHESIS, FUNCTIONALIZATION AND INCORPORATION INTO HOLOGRAPHICALLY ASSEMBLED NANOCOMPOSITES

3.1 Introduction

The previous chapter described the success in holographically fabricating nanocomposites in which the nanoconstituent was arranged in a regular fashion instead of the typical isotropic distribution. Depending on the nanoconstituent used, the anisotropic periodicity can bring about interesting optical, magnetic, or electrical properties. Silica nanoparticles were used to determine the feasibility of holographic assembly since they were easy to functionalize and incorporate into monomers. There is a slight index of refraction mismatch between the silica nanoparticles (1.46) and matrix monomers (1.5) that adds index contrast between high and low intensity regions of the sample; but despite this small increase in optical efficiency, the silica nanoparticles do not add much functionality to the nanocomposite. Adding other types of nanoparticles could add more interesting functionality to the holographically assembled nanocomposites.   For instance, adding titanium dioxide which has an index of refraction of 2.55 significantly increases the index contrast between the nanoparticles and the polymer matrix, making it possible to fabricate high efficiency holographic optical elements in one step. Another possibility would be to create a nanocomposite with alternating planes of two different types of nanoparticles by selectively assembling one type of particle into high intensity regions and another type of particle into low intensity regions.

Instead of incorporating nanoparticles into a solely monomeric matrix, there are also interesting applications if assembled inside holographic polymer dispersed liquid crystals (HPDLCs).   To assemble the nanoparticles inside of a HPDLC, there must be a way to

selectively control the placement of particles into regions of polymer or liquid crystal. Previous

work by John Busbee demonstrated that silica nanoparticles can be selectively assembled in the

polymeric or liquid crystalline regions of HPDLCs by changing the functional groups on the

outside of the nanoconstituent.[97] (Figure 3.1)
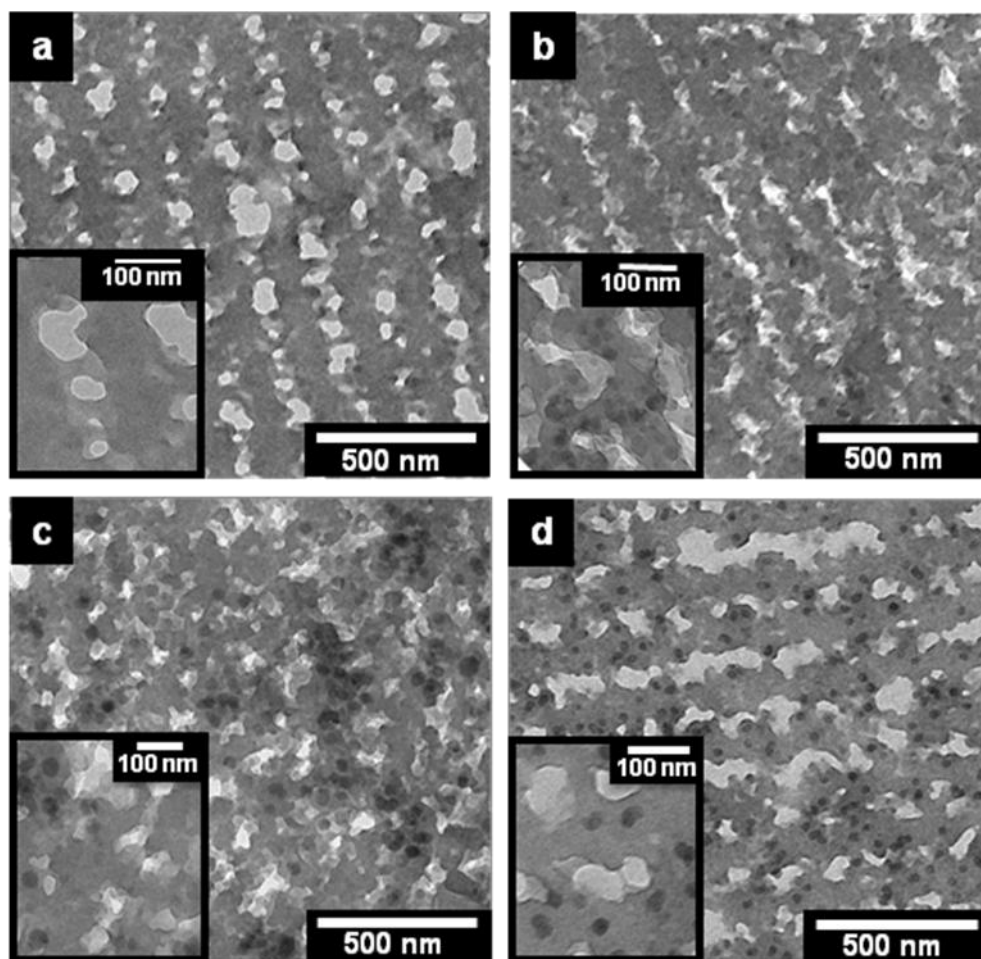
Figure 3.1. TEM micrographs of 75 nm thick microtomed cross-sections of HPDLCs created
through 2-beam exposure. All samples contain the same acrylate based polymer matrix and
liquid crystal. a) Without nanoparticles, b) with 10 wt% unfunctionalized 20 nm diameter SiO_2
nanoparticles, c) with 10 wt% SiO_2 nanoparticles functionalized with pentyltriethoxysilane, and
d) with 10 wt% SiO_2 nanoparticles functionalized with methacryloxypropyltrimethoxysilane.[97]

Unfunctionalized silica nanoparticles that were added to the HPDLC mixture before

photopolymerization, were sequestered into the regions of liquid crystal upon exposure.

However, if the same silica nanoparticles were functionalized with methacryloxypropyltrimethoxysilane before polymerization, the nanoparticles would end up in the polymeric regions of the sample. With the ability to engineer the positions of the nanoparticles, it would be interesting to add nanoparticles that serve a function.

If quantum dots are added into the polymeric regions of the HPDLC, and their emission is engineered to occur at the wavelength of the band edge of the HPDLC, then the absolute intensity of the quantum dot emission could be tuned by applying an electric field and changing the director positions of the liquid crystal. Due to the high density of states at the band edge there would be a greater absolute intensity of the quantum dot emission when the Bragg grating is on and the voltage is off. The one-step fabrication of quantum dots inside of the polymeric regions of an HPDLC offers a way to electrically modulate quantum dot emission intensity.

Adding ferroelectrically bistable particles to the HPDLC would also be interesting for the purpose of creating bistable optical displays. The liquid crystal could be switched by an electric field, and the ferroelectric nanoparticles within the polymeric regions of the HPDLC could hold the charge necessary to keep the liquid crystals from relaxing back into their original positions. An opposite field would have to be applied in order to reorient the liquid crystals. This type of bistable device would be advantageous in applications like electronic paper.

Many types of small nanoparticles were synthesized for incorporation into holographically assembled nanocomposites. These include silica, titania, ferroelectric barium titanate, and silica coated quantum dots.

3.2 Nanoparticle Synthesis and Functionalization

3.2.1 Silica Nanoparticles

20 nm silica particles were created by a modified Stöber recipe.[98] 92.16 mL of 200 proof, non-denatured ethanol were added into a round bottom flask and stirring vigorously with a magnetic stir bar. 3.26 mL of ammonium hydroxide were added and allowed to stir for at least 1 min before adding 3.72 mL of tetraethoxysilane (TEOS). It was important to measure out the complete amount of TEOS and pour it into the stirring solution all at once to keep the nanoparticles monodisperse. The mixture was stirred for at least 8 hours.

20 nm silica recipes that do not use any water tended to become susceptible to changes in size as the humidity changed. To combat this, water could be added to the recipe.   A more reliable recipe to use contains: 40 mL ethanol, 1 mL ammonium hydroxide, .5 mL DI water and 1 mL TEOS mixed in the order listed. (Figure 3.2)

50 nm silica was prepared very similarly, but the volume fractions (mL) of ethanol, DI water, ammonium hydroxide, and TEOS were changed to a volume ratio of 245: 3.8: 8.5: 7.7 respectively. (Figure 3.3)
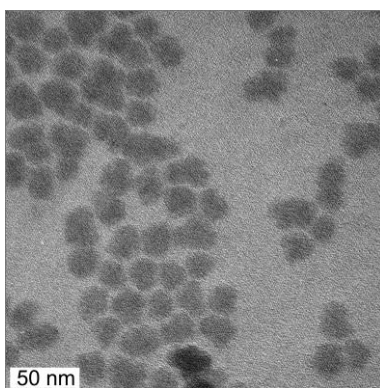
Figure 3.2. TEM micrograph of 20 nm silica particles created by mixing 40 mL ethanol, 1 mL ammonium hydroxide, .5 mL DI water and 1 mL TEOS.

46
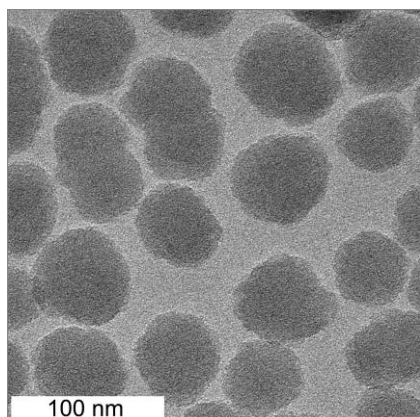
Figure 3.3. TEM micrograph of 50 nm silica particles.

The silica surface was functionalized using silane moieties. Before the particles were cleaned, silanes were added into the stirring mixture to functionalize the surface. For instance, 0.86 mL of methacryloxypropyltrimethoxysilane (MPTMOS) was added into the nanoparticle mixture to add functional acrylate groups to the surface of the silica. If the ammonium hydroxide was removed from the nanoparticle mixture, a base needed to be added or the silane would not attach to the silica surface. The mixture was stirred for another 8 hours after silanes were added, and then cleaned by dialysis.

3.2.2 Silica Coated Quantum Dots

Silica coated quantum dots were created by following Holloway's paper on water soluble core shell nanocrystals.[99] The resulting quantum dots absorbed at 380 nm and emitted at 590 nm. The quantum dots were created by first making the CdS:Mn core, then adding on the ZnS shell, and finally the silica shell.

To make the CdS:Mn core, a mixture of 4.44 g sodium bis(2-ethylhexyl) sulfosuccinate (AOT) and 100 mL heptane were stirred in a round bottom flask. 0.048 g $Cd(CH_3CO_2)_2 \cdot 2H_2O$, 0.0006 g $Mn(CH_3CO_2)_2$, and 1.80 mL water were premixed together and added into the

AOT/heptane solution to make a Cd^{2+}/Mn^{2+} micelle solution that was stirred for 15 minutes. Simultaneously, in a separate round bottom flask, 13.5 g AOT was mixed with 303 mL heptane. 0.2812 g Na_2S and 5.46 mL water were premixed together and added to the AOT/heptane mixture and allowed to stir for 15 min to create a S^{2-} micellar mixture. The Cd^{2+}/Mn^{2+} micelle solution was then injected into this a S^{2-} micellar mixture and stirred for 15 minutes to create a yellow solution of quantum dots.

In another round bottom flask, 13.6 g AOT was mixed with 307 mL heptane. A premixed solution of 0.264 $Zn(CH_3CO_2)_2$ and 5.53 mL water was mixed into the AOT/heptane mixture and stirred for 15 minutes. This mixture was then slowly added (~1.5 mL/min) into the quantum dot solution. A ZnS shell covers the quantum dots after this step.

Finally a silica shell is added over the ZnS shell. 3.7 mL TEOS was injected into the quantum dot mixture and stirred for 15 min. After 15 min, a premixed solution of 5.5 g AOT, 123 mL of heptane, and 2.2 mL NH_4OH (30 wt%) was injected into the quantum dot mixture and stirred for 48 hours. The result was 20 nm silica overcoated quantum dots. (Figure 3.4)
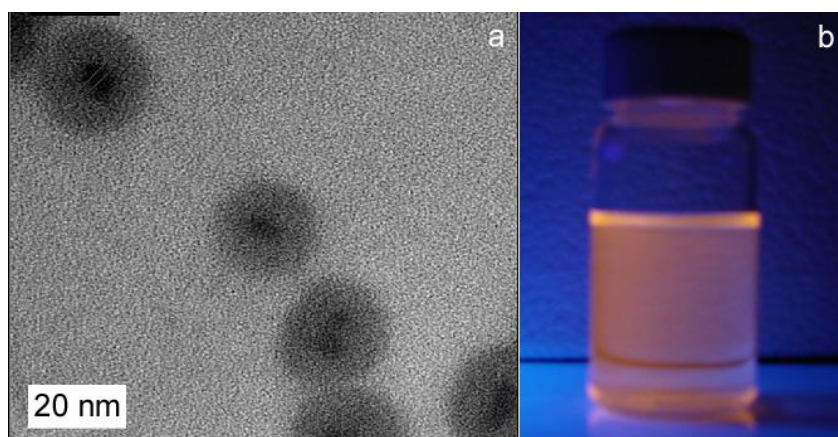
Figure 3.4. a) TEM micrograph of CdS:Mn/ZnS quantum dots covered by a silica shell. b) A macroscopic view of the same CdS:Mn/ZnS quantum dots in solution under UV excitation.

1 mL MPTMOS was added for every 100 mL unpurified quantum dots to functionalize the surface with acrylate functional groups. To clean the quantum dots, 2 parts acetone was added to 1 part of the quantum dot solution and centrifuged. Quantum dots could be redispersed in heptane, but were still covered in AOT. More cleaning cycles led to aggregation of the quantum dots.

3.2.3 Titanium Dioxide

This TiO_2 synthesis was modified from the paper ―Hydrothermal Synthesis of Er-Doped Luminescent TiO_2 nanoparticles".[100] 54 mL deionized water (DI) was added into a round bottom flask and stirred vigorously. 5.68 g of titanium isopropoxide was added slowly into the water and stirred for 1 hour. This mixture was then filtered through a glass frit and washed with DI water three times. The damp sediment was placed in a flask with 13 mL DI water and 0.456 g tetramethylammonium hydroxide. The tetramethylammonium hydroxide functionalized the surface of the titanium dioxide with a quatanery amine. This mixture was sonicated for 5 min and subsequently heated to 85°C for 1 hour in a closed container under vigorous stirring. After an hour, 2 more mL of DI water were added, and the mixture was placed in a Parr acid digestion bomb for 3 hours at 210°C. The resulting mixture was centrifuged 4 times at 8000 RCF for 3 hours and then easily redispersed in water due to the amine functionalization. (Figure 3.5)
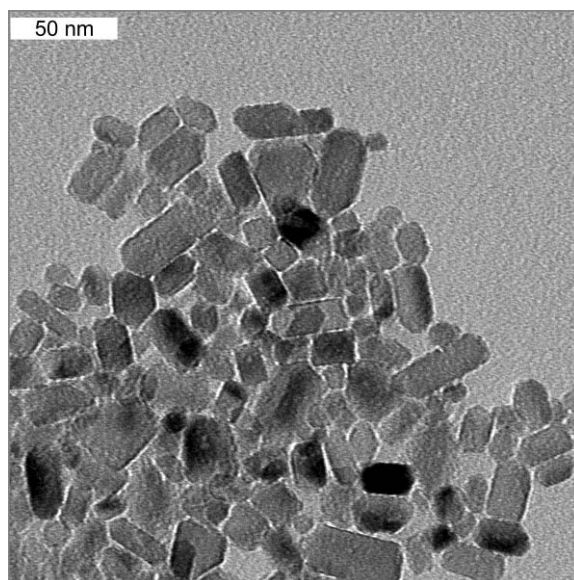
Figure 3.5. TEM micrograph of hydrothermally synthesized titania nanoparticles.

3.2.4 Barium Titanate

70 nm tetragonal $BaTiO_3$ nanoparticles were fabricated by following a paper titled :

―Tetragonal Nanocrystalline Barium Titanate Powder: Preparation, Characterization, and

Dielectric Properties".[101] 39.04 g of $BaCl_2 \cdot 2H_2O$ were mixed with 18.90 g (10.98 mL) $TiCl_4$ and

10mL DI water. 36 g of NaOH were then added to the mixture, but this was done slowly since

the reaction was very exothermic. A white colloidal sol was formed with some undissolved

barium salts. More DI water was added to the mixture to make the final volume 100 mL. 20mL

of the final mixture was added into a Parr acid digestion bomb and heated to 240°C for 12 hours.

The $BaTiO_3$ was rinsed with water and centrifuged. The precipitate could be dried using a

vacuum oven at 60°C for 24 hours. These particles were not functionalized.
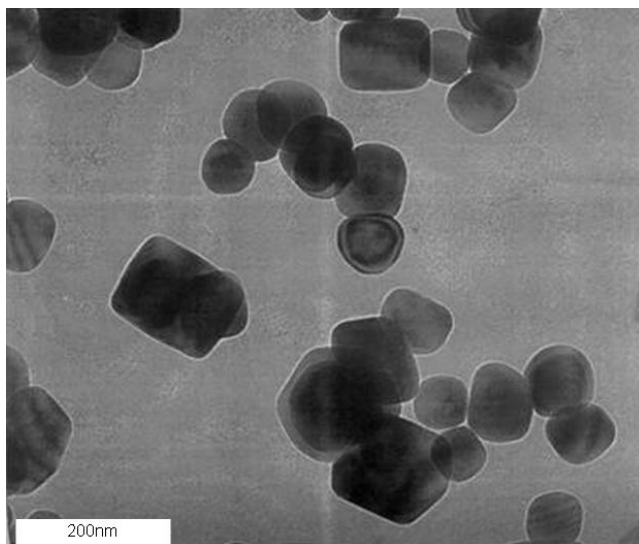
Figure 3.6. TEM micrograph of hydrothermally synthesized barium titanate nanoparticles.

3.3 Nanoparticle Incorporation into Holographically Assembled Nanocomposites

Once synthesized, the nanoparticles needed to be incorporated into a mixture of

monomer and photoinitiator for assembly by photopolymerization. The method of

holographically assembling nanoparticles was intended to be a tool that could assemble most

arbitrarty nano-sized materials, but there were actually many requirements for both the

monomeric matrix and the nanoconstituent.   The most obvious requirement was that the

nanoparticles must not aggregate when mixed into the monomer and photoinitiator or the

aggregations would be too large to move. The monomeric mixture had to be soluble in the

nanoconstituent's solvent, because the nanoparticles were added in solution and then the solvent

was rotovaped out of the mixture.   The nanoconstiuent typically needed to be functionalized to

keep it from aggregating in the monomeric mixture. Figure 3.7 demonstrates that

unfunctionalized 20 nm silica particles aggregate in a Norland Optical Adhesive 65 thiol-ene

matrix, but the same particles functionalized with MPTMOS disperse well in the matrix.
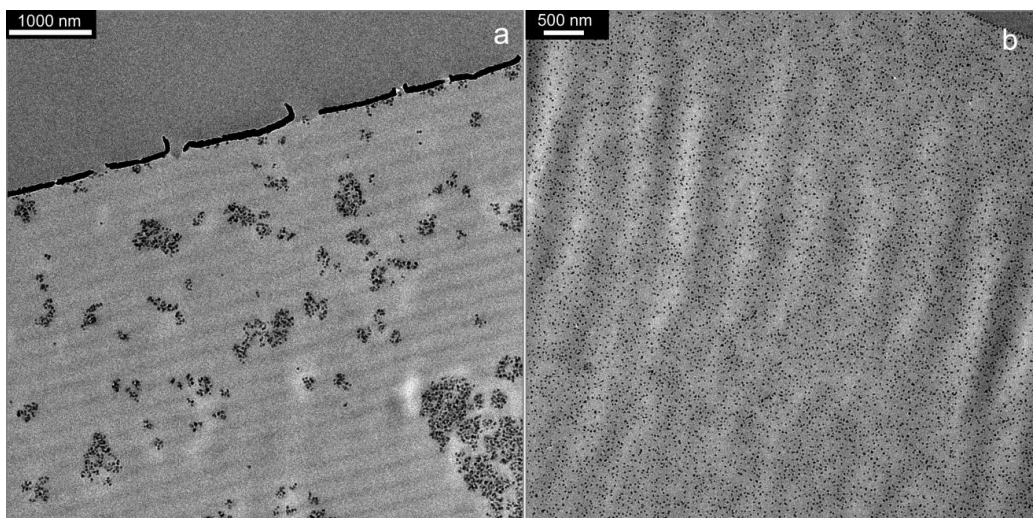
Figure 3.7. Two TEM micrographs of 90 nm microtomed sections of a polymerized NOA 65 matrix containing a) unfunctionalized 20 nm silica particles b) silica nanoparticles functionalized with MPTMOS.

The viscosity of the mixture needed to stay around or below 0.1 Pa*sec for the biased Brownian motion to move nanoparticles before gelation locked them in place. Typically a high viscosity and a low viscosity acrylate were mixed to create a matrix in which the nanoparticles would not aggregate. In most cases, adding more of the low viscosity monomer would cause the nanoparticles to aggregate. The best way to decrease the viscosity without changing the monomers was to add NVP; not only because of its low viscosity, but it typically increased the miscibility of the nanoparticles and it incorporated into the matrix during polymerization.

Holographic assembly occurred in the discussed nanocomposites because a laser interference pattern induced biased Brownian motion of the nanoparticles that caused them to sequester into periodic lines. The interferogram can assemble particles throughout the thickness of the sample in a perfectly transparent nanocomposite. However, if the nanoparticles are large or if there are even small agglomerations of nanoconstituent, then light scattering will quickly distort the high and low intensity regions of the interference pattern. The Rayleigh scattering

formula can be used to determine the transparency loss from spherical nanoparticles of radius r.[102-104]

$$T = \frac{I}{I_0} = \exp\left\{ -\frac{32\pi^4 \phi_p x r^3 n_m^4}{\lambda^4} \left[\frac{\left(n_p/n_m\right)^2 - 1}{\left(n_p/n_m\right)^2 + 2} \right]^2 \right\}$$

I/I_o is the transmitted intensity over the initial intensity of the incoming light, x is the optical path length, n_p is the nanoparticle index of refraction, n_m is the index of refraction of the monomer, λ is the wavelength of the incoming light, and ϕ_p is the volume fraction of nanoparticles in the nanocomposite. For small optical loss by scattering, the index contrast between the polymer matrix and the nanoconstituent should be made as small as possible, and the nanoparticles should be made smaller than 25 nm. High index particles can be assembled if their size is less than 10 nm, and large particles can be assembled on the surface of a nanocomposite, but not through the thickness of the sample. Despite efforts to functionalize the surface of the synthesized BaTiO$_3$ or TiO$_2$ with silanes, phosphonic acid,[105] methacrylic acid, or a biomimetic inititator,[106] the particles agglomerated in each monomeric matrix. (Figure 3.8)
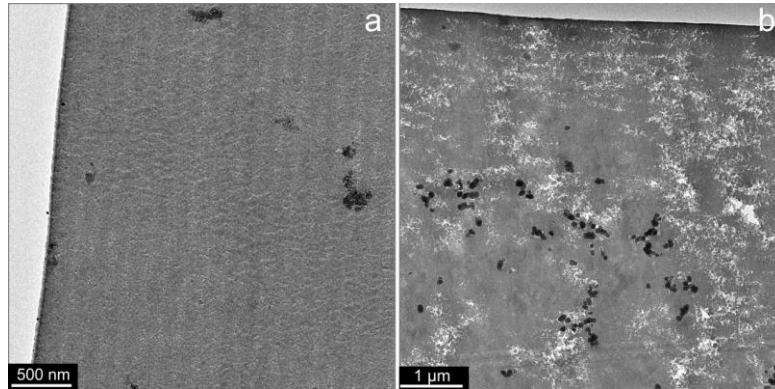
Figure 3.8. TEM micrographs of 90 nm microtomed cross-sections of a) MPTMOS functionalized TiO$_2$ in an acrylate matrix and b) phosphonic acid modified BaTiO3 in an acrylate based HPDLC.

Finally, the nanoconstituent added must not significantly absorb the writing wavelength of the laser because the high and low intensity regions of the interferogram quickly become distorted.

3.3.1 Quantum Dot Incorporation into Photoresist

With a better understanding of the properties necessary for assembling nanoparticles, we can extend this method to assembling nanoparticles that add functionality to the system. In this case, quantum dots were added into holographic polymer dispersed liquid crystals. The periodic layers of polymer and liquid crystal form a stop band within the transmission spectra. If the emission wavelength of the embedded quantum dots can be engineered to be at a slightly higher wavelength then the stop band, it is possible to decrease the group velocity of the quantum dot emission and increase the interaction time of light within the device. When an electric field is applied it should cause the stop band to disappear, and the interaction time of the quantum dot emission in the HPDLC should decrease as well.

CdSe/ZnS quantum dots with a trioctylphosphine oxide (TOPO) shell were fabricated by Congjun Wang in Moonsub Shim's group. (Figure 3.9)
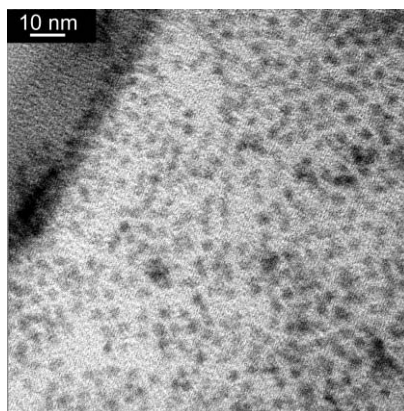
Figure 3.9. TEM micrograph of CdSe quantum dots with a ZnS shell that emit at 520 nm.

The quantum dots had to reside within the polymeric regions of the HPDLC so that they would not affect the switching of the liquid crystal by an electric field. Rather than assembling the quantum dots into regions of destructive interference (liquid crystal regions), a reactive acrylate functionalization was added on to the surface of the quantum dots to trap them into the regions of constructive interference. The quantum dots were first cleaned by adding 2 mL of butane for every 5 mL of the quantum dots in TOPO. Methanol was added to this mixture until the quantum dots began to precipitate, and then the mixture was centrifuged. The dots were re-dispersed in chloroform and excess methacrylic acid was added. The mixture was heated at 100°C for an hour, and then cooled, and water was added to precipitate the quantum dots again and clean out the excess methacrylic acid. The nanocrystals were centrifuged again and then re-dispersed in ethanol. Figure 3.10 shows the red-shift of the quantum dot absorption and emission before (black) and after (red) the addition of the methacrylic acid.
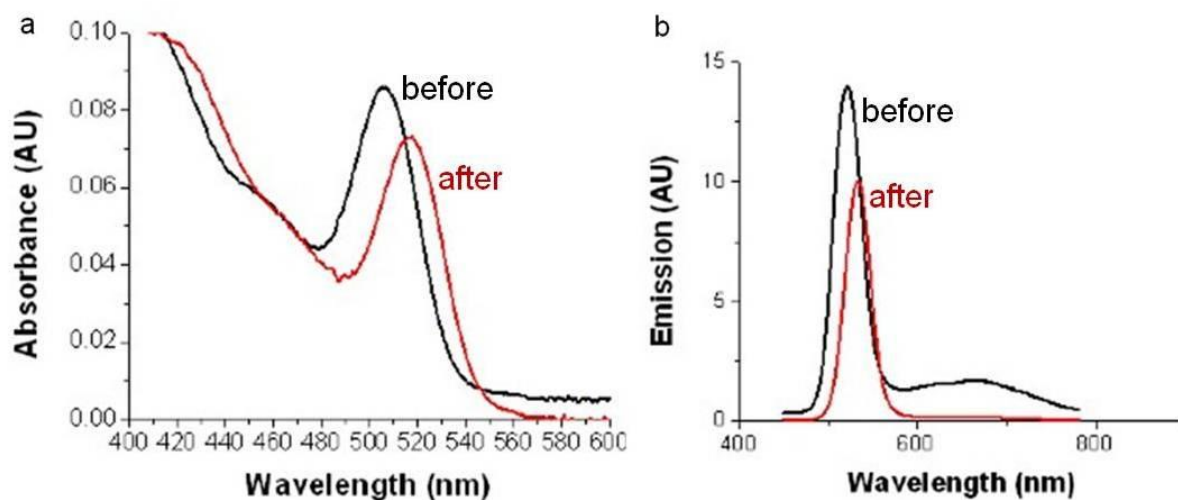
Figure 3.10. The a) absorption and b) emission spectra of CdSe/ZnS quantum dots before cleaning (black) and after functionalization with methacrylic acid (red).

The quantum dots were added into 0.50 g dipentaerythritol penta-/hexa-acrylate and 0.003 g monomethyl ether hydroquinone (MEHQ), which inhibited polymerization of the

monomer until photopolymerized by a 532 nm laser. The excess ethanol was rotovaped from the monomer and the other components of the HPDLC photopolymerizable mixture were added. This included: 0.01 g Diiodoflurescein (initiator), 0.02 g 2,6-Diisopropyl-N,N-dimethylaniline (co-intiator), 0.1 g 1-Vinyl-2-pyrrolidinone (solublizer), 0.05 g octanoic acid (surfactant for liquid crystal switching), 0.30 g TL213 (liquid crystal), 10 micron glass spheres (spacers), and 2 drops of NOA 65 (monomer). A few drops of this mixture were placed between ITO coated glass slides and polymerized with a 532 nm laser in Bragg reflection geometry for 1 min at 30 – 75 mW. The diffraction efficiency of the films ranged from 36 – 44% on the day of exposure. The films were microtomed and viewed by TEM. (Figure 3.11) The quantum dots were trapped within the polymer matrix, while the liquid crystal sequestered into the regions of destructive interference.
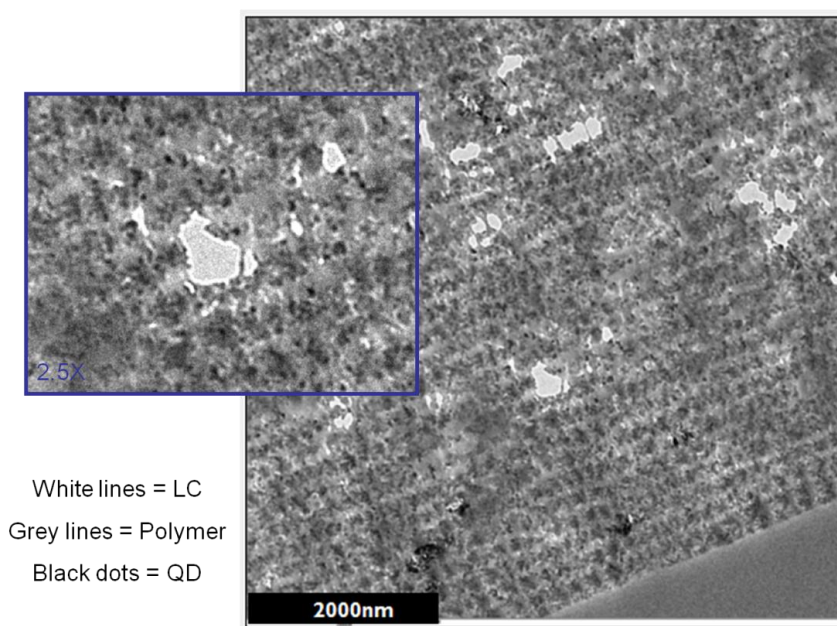
Figure 3.11. TEM micrograph of a 90 nm microtomed Bragg reflection notch in which CdSe/ ZnS quantum dots are embedded within the polymeric regions of a HPDLC.

The laser geometry was carefully tuned so that the reflection notch would fall around 560 nm after accounting for shrinkage due to photopolymerization. This put the quantum dot emission of 577 nm on the low-energy side of the reflection notch, where the group velocity of light was slowed. (Figure 3.12)
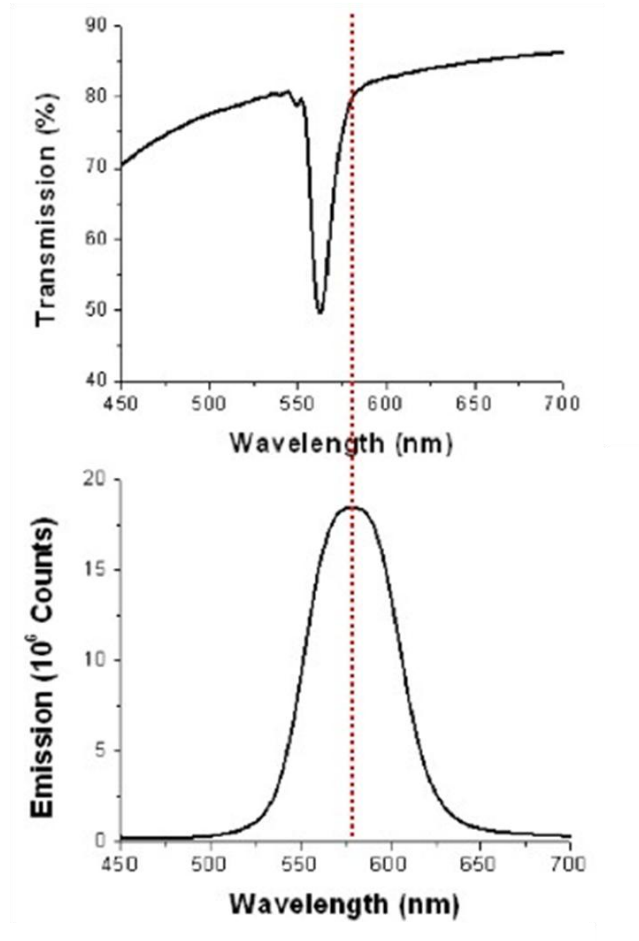
Figure 3.12. Above is the transmission spectra of a reflection HPDLC with embedded quantum dots. Below is the absorbance spectra for CdSe/ ZnS quantum dots embedded in the HPDLC. The peak of the quantum dot emission falls on the low-energy side of the HPDLC stop band.

3.3.2 *Optical Characterization of Quantum Dots in HPDLCs*

In order to measure the effect that the HPDLC has on the quantum dot emission, a laser with a 441.6 nm wavelength was used to excite the quantum dots within the HPDLC. The yellow emission from the QD was normal to the surface of the sample and was passed through a

filter to block the blue laser's light, and then into a spectrometer. The intensity of the quantum

dot emission was monitored with and without the application of an electric field to turn the

HPDLC off and on. A graph of the quantum dot emission with the grating turned on and off is in

figure 3.13. There was an increase in the absolute intensity of the quantum dot emission when

the grating was on versus off, but the effect was not great due to the poor diffraction efficiency

of the HPDLC and the small quantity of quantum dots that could be embedded in the sample.

The quantum dots had a rather high absorption at the writing wavelength of 532nm, which

reduced the diffraction efficiency of the sample. Since the width of the quantum dot emission is

around 100 nm, there is no writing wavelength that will allow for high diffraction efficiency

while still keeping the peak of the QD emission on the low- energy side of the stop band.
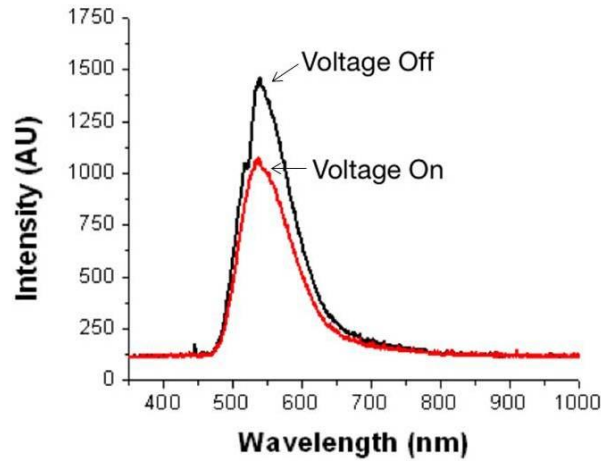
Figure 3.13. Emission from quantum dots embedded inside of a HPDLC. The blue curve is the
QD emission when the HPDLC is in the reflective state with the grating turned on. The orange
curve is the emission after an electric field is applied, and the absolute value of the quantum dot
emission decreases.

The diffraction efficiency of the quantum dot HPDLC as a function of voltage applied is in

figure 3.14. The measurement was taken twice to show the reproducibility of the switching.
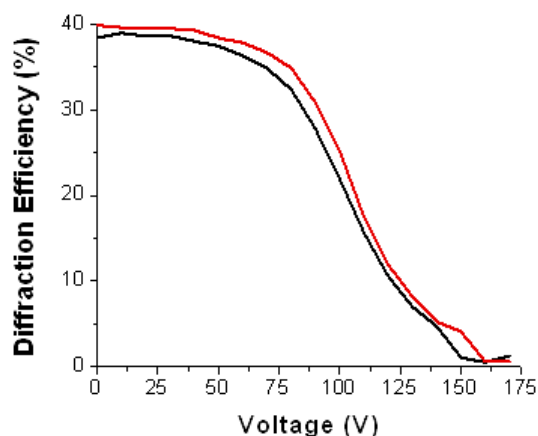
Figure 3.14. The diffraction efficiency of the reflection mode HPDLC containing CdSe/ZnS quantum dots as a function of switching voltage. The cell was 10 microns thick and approximately and inch in diameter. The cell was switched twice to demonstrate its reproducibility.

3.4 Conclusions

Assembling inorganic nanoconstituents anisotropically in an organic matrix offers the possibility of nanocomposites with unique properties. The method of assembling these nanoconstiuents holographically offers a quick one-step method to pattern nanoscale moieties over large areas. However, there are some restrictions to applying this method to any arbitrary material. The major obstacle in utilizing this method is creating a highly transparent nanocomposite. There are methods of increasing transparency by reducing index contrast between the polymeric matrix and the inorganic nanoparticle, or just using nanoparticles less than 10 nm in size. Since 2002 there have been many reports of using holographic assembly to add functionality to nanocomposites. For example, high efficiency holographic optical elements were created by assembling high index titania or zirconia nanoparticles less than 10 nm in size.[67-71] Recently, one group assembled quantum dots and zirconia silumtaneously to amplify the spontaneous emission of the quantum dots within the nanocomposite. The core–shell CdSe/ZnS nanocrystals were used as a gain medium, while the ZrO_2 nanoparticles were used to create the

high efficiency refractive index grating.[75] Advances in surface modifications of nanoparticles, their compatability with polymeric matricies, and increasing transparency of nanocomposites will make holographic assembly a more widely used method to create functional nanocomposites.

CHAPTER 4

LIQUID CRYSTAL IN-FILLED SU8 NANOSTRUCTURES FOR ACTIVE OPTICAL

DEVICES

4.1 Introduction

Photonic crystals are materials of periodic relief structures with size comparable to the wavelength of incident light, which inhibit light propagation of a certain frequency range.[3] To make optical switches or tunable filters out of photonic crystals it is necessary to have a method of tuning the optical properties. Electrical,[107-110] thermal,[111-112] mechanical,[113] and optical[114-117] approaches have all been used to alter the band gap of photonic crystals. Perhaps the most widely used method for switching photonic crystals is by infiltrating the structure with electrically switchable birefringent liquid crystals, since the tuning is reversible.

Many research groups have in-filled self- assembled colloid photonic crystals with liquid crystal, and studied the effects of electrical or thermal switching on the optical properties.[118-123] Since the colloidal crystals are three-dimensional (3D), a full photonic band gap can be achieved; however, the crystals are prone to defects and cannot be made over large areas. Holographic polymer dispersed liquid crystals (HPDLC's) offer a one step process to create 3D optical devices that can be controlled by an electric field.[124-126] However, there are many limitations to this system as well. Typically the volume fraction of liquid crystal cannot be greater than 20%-50% at room temperature or else the resin loses liquid crystal solubility. The periodicity can't be much greater than a few microns because the liquid crystal cannot diffuse far enough before gelation. The acrylate and thiol-ene chemistries do not offer a smooth-walled, connected network of liquid crystal, and the switching voltage can vary greatly by making small changes in the chemical composition.

Interference lithography offers a method of creating large defect-free photonic crystals that can be filled with a wide range of liquid crystal filling fractions. Although the fabrication will no longer be a single step, it is possible to produce much more perfect photonic crystals in SU8, and then fill these structures with liquid crystal. The SU8 can also be inverted to a different material to achieve larger index contrast. There are very few reports of infilling holographically created SU8 nanostructures to create switchable optical elements,[127] and none of the reports use nanostructured materials. In this chapter, the behavior of nematic liquid crystal within holographically fabricated SU8 photonic crystals was studied by monitoring the diffraction efficiency as a function of an applied electric field.

One, two, and three dimensional (1D, 2D, and 3D) photonic crystals with a periodicity of approximately 600 nm were fabricated on indium tin oxide substrates (ITO) using SU8 photoresist. The corresponding structures were created with two, three, and four laser beams respectively at a wavelength of 532 nm. After fabrication, the photonic crystals were filled with TL213 liquid crystal, and electrically switched while the diffraction efficiency was monitored. The diffraction efficiency of the one and 3D photonic crystals filled with TL213 varied as an electric field was applied. However, the 2D photonic crystal filled with TL213 did not switch, even at high voltages, indicating that the liquid crystal was either confined, strongly anchored inside the cylindrical geometry, or that the liquid crystal directors took on an orientation that was in the same direction as the applied electric field. The same 2D nanostructure was then in-filled with a negative dielectric liquid crystal called 2079. The diffraction efficiency varied with electric field, but the threshold voltage for switching was high. This suggests that the liquid crystal was not confined in the 2D structure because it switched. The high threshold voltage is most likely due to strong surface anchoring.

4.2 Device Fabrication

4.2.1 *Laser Setup*

A Coherent Inc. Verdi 5W frequency doubled Nd:YVO4 continuous wave laser with a 2.25 mm beam diameter and a constant wavelength was used as a coherent beam source. The laser was placed on a floating optical table to reduce vibrations. The polarization of the beam out of the laser was vertical.   The beam was first reflected off two mirrors to change the propagation direction of the beam by 180° which reduced reflections back into the laser. It is always advantageous to start with two mirrors that allow fine tuning in two dimensions (for example x and y). If an optic gets knocked out of position, every degree of freedom is available by changing those two mirrors, and the laser can be aligned into the desired position. The laser was then directed through a spatial filter to reduce imperfections and erase the higher diffracted orders within the beam.   The beam was expanded by four times from the spatial filter. From this point, the laser was directed into a two beam and a four beam interference setup. A fixed half waveplate (vertical polarization switched to horizontal) was added before a polarizing beam splitter, which sent 100% of the power in a horizontally polarized beam to the four beam set-up. When the two beam set-up was to be used, another movable half waveplate was inserted after the previous half waveplate but before the polarizing beam splitter. This sent the 100% vertically polarized light through a different face of the beam cube. In this way a single optic could be moved to switch between each setup. A beam profiler was used to measure the intensity of the Gaussian beam after the polarizing beam splitter. (Figure 4.1) The dust spots are on the neutral density filter of the beam profiler.
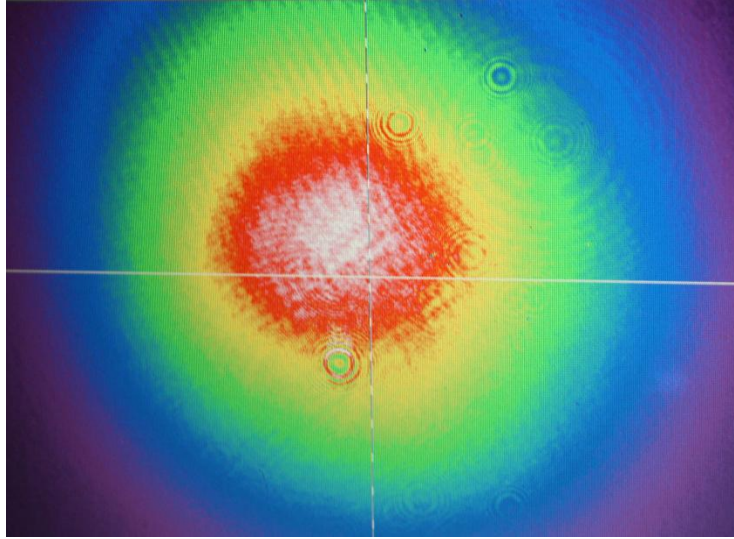
Figure 4.1. A Si detector taking the Gaussian beam intensity profile at a 532 nm wavelength. White represents the highest intensity while purple represents the lowest. The dust spots are on the beam profiler and are not artifacts in the beam.

For the two beam setup, the beam was expanded to 10x the size of the 2.25 mm beam, a 50/50 non-polarizing beam cube was used to split the one beam into two beams, and the two beams were overlapped in a transmission geometry. The reflections off of the sample holder were made to overlap with the incoming beams to keep the grating from being blazed.

The four beam interference was setup in an umbrella configuration. (Figure 4.2) Three side beams with linear polarization and equal power formed a perfectly isosceles triangle around a central beam that ran perpendicular to the laser table. The center beam had a circular polarization and the power of the center beam was 3.7 times the power of an individual side beam. The power of each beam was controlled by half waveplates and beam splitters.
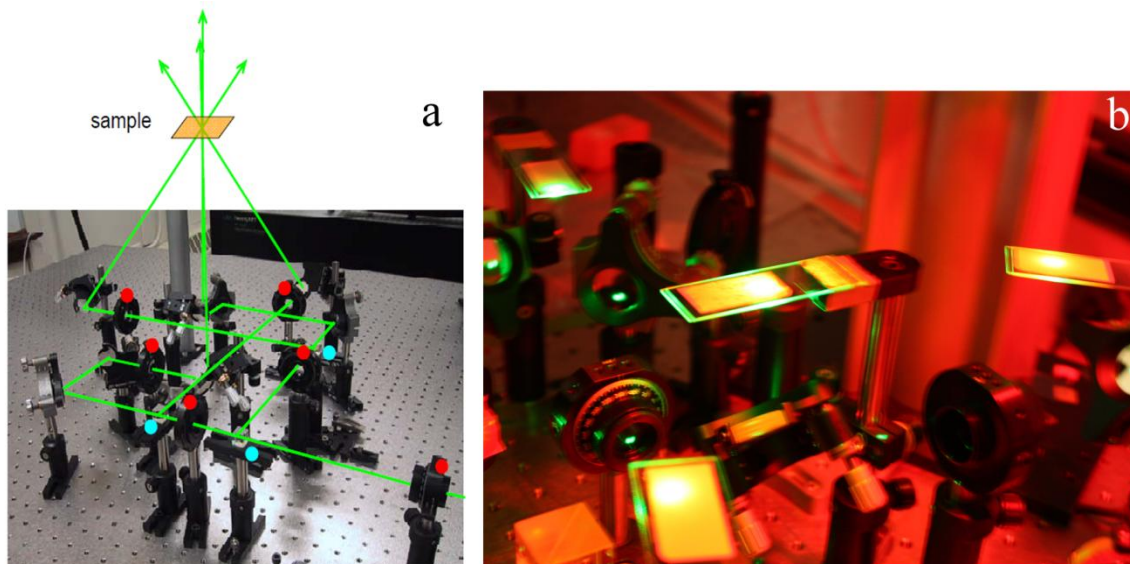
Figure 4.2. a) Optical setup for four beam interference. Image provided by Dr. Ying-Chieh Chen. b) Image of the four beam optical setup, where each of the four beams intersects with a plane parallel to the laser table. The three linear beams form an isosceles triangle around the central beam.

4.2.2 Liquid Crystal Rubbing Layer

Liquid crystal rubbing layers direct the orientation of the liquid crystal on the surface of a substrate. The rubbing layer usually consists of a 500-5000Å thick layer of polyimide that has been rubbed with a piece of felt or velvet in a preferential direction. In this case, 8 mL of HD Microsystems PI2555 was mixed with 32.5 mL of N-methyl pyrrolidone and 9.1 mL of 1-methoxy-2-propanol. Once homogenously mixed, the resin was filtered through a 0.45 µm syringe filter.

The substrate was cleaned by oxygen RIE or by sonicating in methanol followed by acetone and finally drying with nitrogen. The substrate surface was fully covered with the polyimide mixture and then spin coated. The spin recipe was 15 seconds at ramp 1000 to 500 rpm followed by 60 sec at ramp 1000 to 2000 rpm. After coated, the samples were heated to 200°C for 30 min to polymerize the polyimide. After cooling, a 3 inch tall cylindrical glass vile

was filled with sand and water to make its mass 57.5 grams. A pendulum was formed by placing the cylinder inside a loop formed by holding two ends of a felt piece of fabric. The substrate was rubbed by the felt surface, and the sand-filled vial provided the force necessary for the rubbed layer. The pendulum is rubbed over the polyimide layer 30 times.

4.2.3 SU8 Processing

To create the SU8 resin for the 1 and 2 dimensional photonic crystals, 0.0361 g of Cyclopentadienyl(fluorene)iron(II) hexafluoro-phosphate (PAG) was mixed with 6.5 g of cyclopentanone (CP) and sonicated. 10.33 g of SU8 2025 was added into this mixture and stirred overnight. To create the 3 dimensional photonic crystals, 0.029 g of PAG was mixed with a few drops of CP. The CP was only added to solubilize the powdered photosensitizer. After sonication, 10 g of SU8 2010 was added and this was stirred overnight.

Before the substrate can be coated with the SU8 resin, it must first be cleaned. If the SU8 is going to be on a bare glass or ITO substrate, then the substrate must be cleaned with a strong oxygen reactive ion etch (RIE). The RIE etch should be done at a pressure of 25 mTorr with 10 ccm oxygen at a power of 150 W for 6 min. The SU8 should be coated on the substrate as soon as the RIE has been completed. If the SU8 layer does not have to touch the bare substrate, it can be put on an adhesion layer, or a flat thin cross-linked layer of SU8. This cross-linked layer was fabricated by spin coating a thin layer of SU8 2000.5 onto the substrate surface. This film was baked at 95°C for 10 min, exposed to long wave UV light for 20 min, and then baked again for 25 min at 95°C. The SU8 resin can be spin-coated onto this cross-linked layer. The adhesion layer is stable for months and does not have to be cleaned or developed.

After the substrate has been prepared, the SU8 processing steps can begin as outlined in figure 4.3. First the resin can be spin coated onto the surface. Unless otherwise noted all spin coating was done with the following recipe:

	rpm	ramp	time
Step 1	500	.5	15 sec
Step 2	2000	2	1 min

Table 4.1. SU8 spin coating recipe.

The substrate should be entirely covered by the SU8 resin before spin coating. The 3D resin has a spun coat thickness of 10 μm, but it shrinks to a final thickness of 5 μm after development. The 1D resin has a final thickness of 2.5μm after development. After coating the samples, they are prebaked by heating on a 65°C hotplate for 10 min, followed by a 95°C hotplate for 25 min. The heating of the sample removes the solvent from the film. An oven is not used because it only dries out the top layer and it traps the solvent inside the thickness of the film. The hotplate offers better uniformity throughout the sample.

After prebaking the samples, they are exposed to the interference pattern. The exposure time is carefully controlled by an electronic shutter. When the sample is exposed to the light, it generates an acid in the regions of constructive interference. The acid does not efficiently crosslink the SU8 until it has been heated. Post baking was completed at 72°C for 20 min in dry air. Since the humidity changes can alter the exposure dose, the samples were baked in dry air. However, although not well understood, oxygen needs to be present for the post bake. Neither nitrogen nor argon environments should be used while post baking. The sample should be baked immediately after exposure to keep the acid from diffusing throughout the sample.
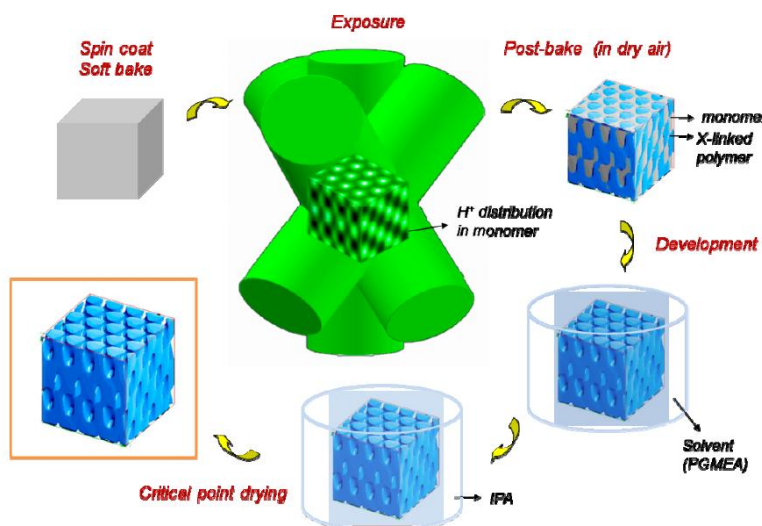
Figure 4.3. SU8 processing steps. The samples are first coated with the SU8 resin and then baked. The samples are then exposed to the interference pattern which releases acid into the monomer. Afterwards, the samples are baked to crosslink the monomer within the exposed regions of the sample. The monomer is removed from the unexposed regions during development in PGMEA. The sample is transferred to IPA for super critical drying. Figure provided by Dr. Ying-Chieh Chen.

After post bake, the samples are cooled and placed in Propylene Glycol Methyl Ether Acetate (PGMEA) to solubilize and remove the uncrosslinked monomer in the destructive interference regions of the sample. The samples should be in the PGMEA for at least 30 min, and they can stay in the PGMEA for days without destruction of the structure. PGMEA is a good solvent for SU8 and causes swelling of the nanostructure. If dried out of PGMEA, the samples collapse. The samples are therefore placed in isopropyl alcohol (IPA) which is a poor solvent for SU8. This causes the SU8 to shrink and protect against collapse. The SU8 structure can be pulled out of IPA and dried in air or by nitrogen. If dried in this manner, the structures are subjected to surface tension during the drying process which can alter the final structure. For high aspect ratio structures, or structures with small interconnected volumes, it is better to super critically dry the structure. During super critical drying, samples are dried at the triple point of carbon dioxide, to remove surface stresses.

4.2.4 Final SU8 Structures

Examples of 1, 2, and 3D samples created in SU8 are in figure 4.4. Each photonic crystal

has a thickness around 4-6 microns, and is created on an ITO substrate. The 1D was created by

interfering 2 linearly polarized beams in transmission geometry. The periodicity of the 1D

structure in Figure 4.4 is approximately 600 nm. This periodicity can be changed by varying the

angle between the two beams. The 2D structure was created by exposing the two-beam

geometry, and then the sample was rotated by 90° and exposed with the same interference

pattern. The 2D structure also has a 600 nm periodicity. The 3D nanostructure was created

using the four beam umbrella configuration. The corresponding diffraction patterns of each

sample are also shown in figure 4.4.
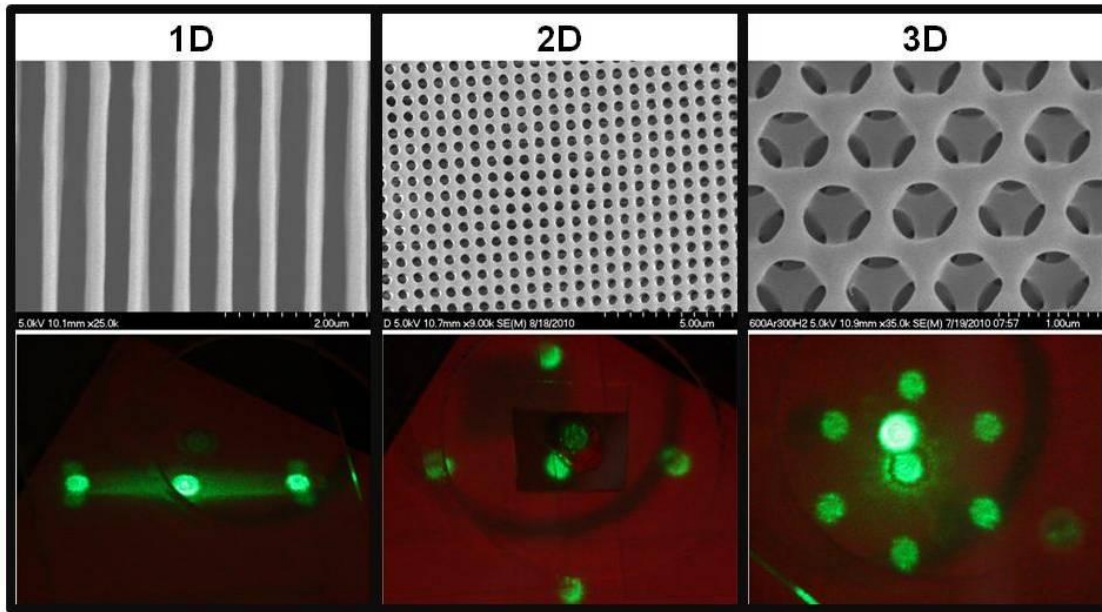
Figure 4.4. SEM of one, two and 3D photonic crystals created in SU8 using a 532 nm laser. The 1D sample was created by interfering two laser beams. The 2D sample was created by recording the 1D interference pattern on the sample, and then rotating it 90º and recording it again. The 3D pattern was made with a 4-beam umbrella configuration. The 1D sample had two diffractions spots, the 2D sample had 4 diffraction spots, and the 3D sample had 6 diffraction spots.

4.3 Device Characterization

The main objective of this project was to study the behavior of liquid crystals within the SU8 structures fabricated by interference lithography.   Polarization optical microscopy, optical spectra, and diffraction measurements were performed on the liquid crystal in-filled SU8 samples.

4.3.1 Polarization Optical Microscopy

Before studying the orientation of the TL213 liquid crystal within the SU8 nanostructures, the orientation on the substrate must first be determined. Polarization optical microscopy can determine the orientation of an anisotropic birefringent specimen, by placing the sample between two crossed polarizers. The possible substrates on which the SU8 nanostructures would be fabricated were an adhesion layer of SU8, ITO on a glass substrate, and a rubbed polyimide layer. To make an accurate determination of the liquid crystal orientation, it had to be sandwiched between two sides of the same substrate, and the thickness of the liquid layer must remain constant. A drop of TL213 was placed on one side of the substrate, two 12 micron Mylar spacers were placed on either side of the drop, and the same substrate was then placed on top of the drop. The samples were placed between two crossed polarizers on an optical microscope set at 50X magnification. The TL213 orientation on a thin adhesion layer of SU8 was tested first. The sample was heated above the liquid crystal clearing temperature and cooled back down to room temperature before placing it on the microscope. The liquid crystal takes on a tilted orientation as demonstrated in Figure 4.5a and b. The change from red to green is most likely due to slight changes in thickness between the SU8 layers.

Figure 4.5. a) Polarization optical micrograph (50X) of TL213 between two SU8 adhesion layers. b) Schematic of TL213 liquid crystal orientation between two SU8 adhesion layers. c) Polarization optical micrograph (50X) of TL213 between two ITO layers. d) Schematic of TL213 liquid cry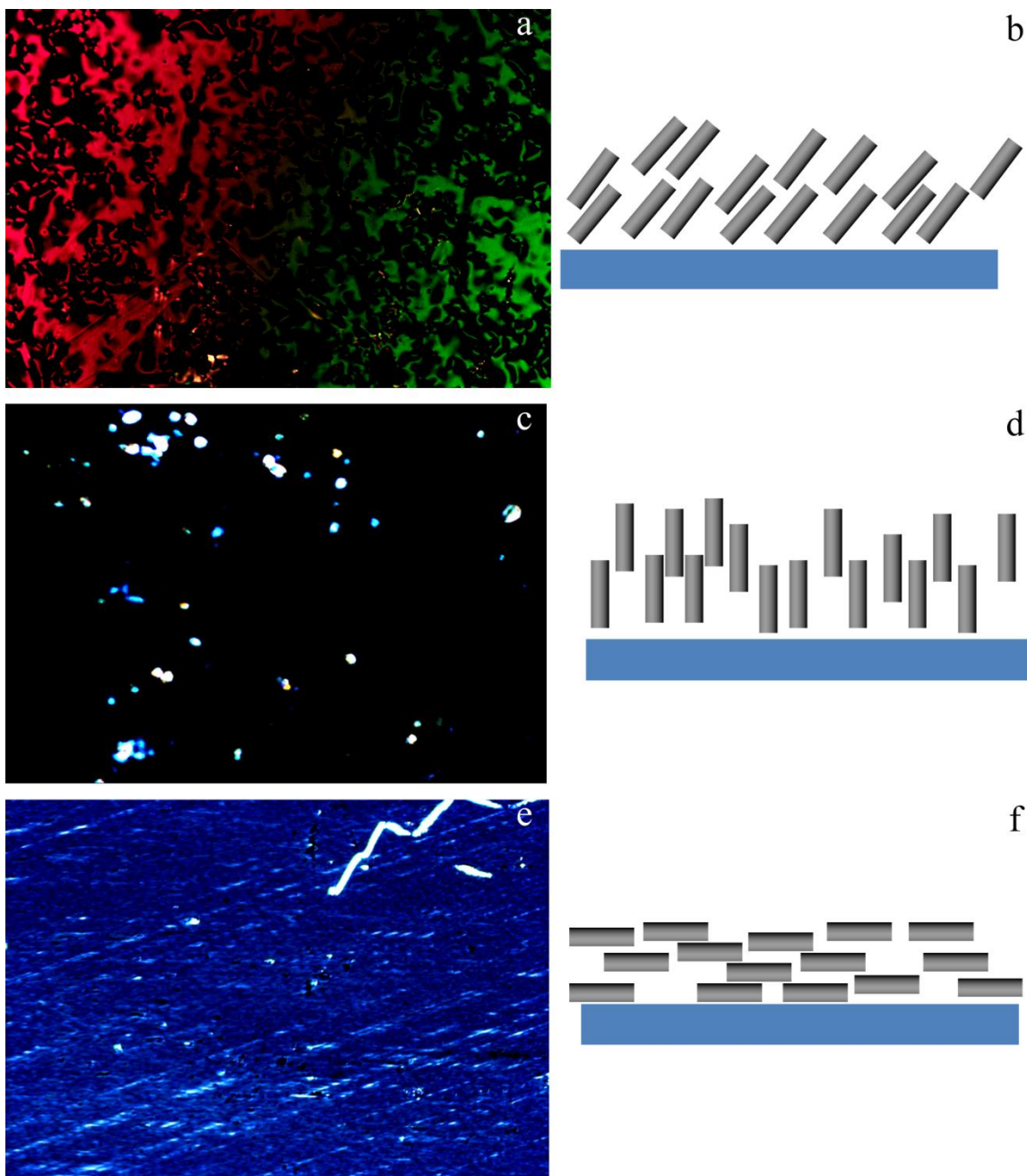stal orientation between two ITO layers. e) Polarization optical micrograph (50X) of TL213 between two polyimide rubbed layers. d) Schematic of TL213 liquid crystal orientation between two polyimide rubbed layers.

When the TL213 was tested on ITO, it surprisingly had a homeotropic alignment.

Usually specialty rubbed layers must be used to achieve homeotropic alignment on a substrate,

the reason for the alignment could be an interesting investigation. When the crossed polarizers were rotated, the sample remained black.

The final substrate tested was the polyimide rubbing layer. The two polyimide rubbing layers, on the top and the bottom of the TL213, were rubbed in the same direction. The rubbing marks are visible in the optical micrograph in Figure 4.5e. When the crossed polarizers were rotated, the sample went from bright to completely black indicating it had a planar orientation.

The liquid crystal orientation in domains smaller than 1 micron cannot be viewed on the polarization optical microscope because optical microscopes do not have that resolution. It would be interesting to view the liquid crystal orientation within an SU8 nanostructure. To do this 1D samples with 2 micron periodicity were fabricated on a liquid crystal rubbing layer. The 1D planes were made parallel to the rubbing layer on some samples and perpendicular on other samples. Both were viewed on the polarization optical microscope. The liquid crystal orientation on the parallel rubbed substrate was as expected. The orientation looked planar (same direction as the rubbing layer) when no voltage was applied, and homeotropic when the voltage was applied. (Figure 4.6) The exact orientation was difficult to determine, because it was hard to differentiate whether the light and dark regions were SU8 or liquid crystal regions. It however was obvious that when switched the liquid crystal did change orientation.

The liquid crystal orientation in the perpendicularly rubbed samples was not simple to determine from the optical micrographs. There was not one homogenous domain within the structure, but rather many different domains. Line defects were visible throughout the structure (Figure 4.7), and only certain parts of the liquid crystal seemed to switch orientation when an electric field was applied. The lack of liquid crystal orientation could be due to the fact that the liquid crystal directors would like to follow the rubbed direction, but were anchored by the SU8

72

structure. There is one research group who studied similar liquid crystal orientations in 1D SU8 structures with 30 micron periodicity.[127] They also observed liquid crystal line defects in samples rubbed perpendicular to the plane direction. They attributed the defects to liquid crystal surface anchoring on the SU8. Two and 3D samples were not studied using polarization optical microscopy because the domains were too small, or the liquid crystal orientation was not obvious.

Voltage Off- planar   Voltage On- homeotropic
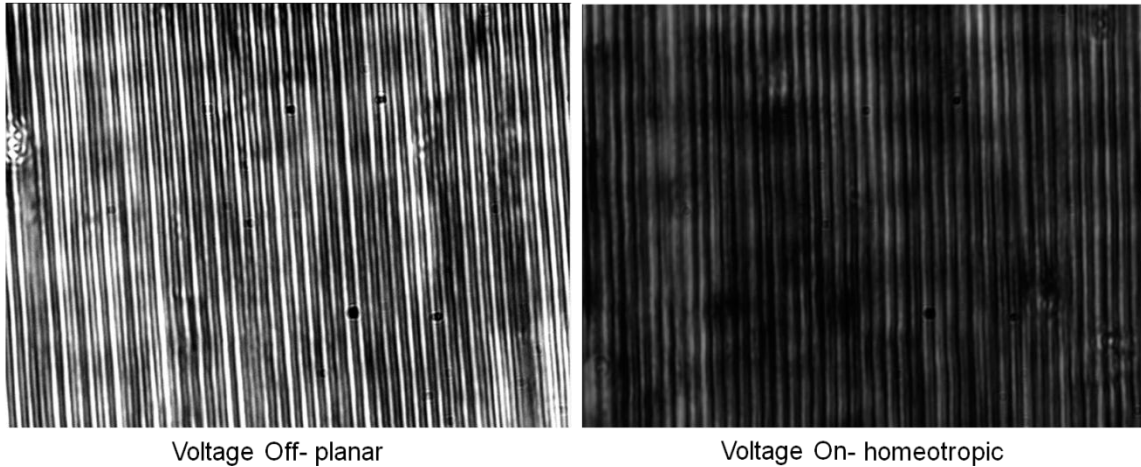
Figure 4.6. Polarization optical micrograph of a 1D SU8 nanostructure with 2 µm periodicity filled with TL213. The left side has no applied voltage, while the right side does.
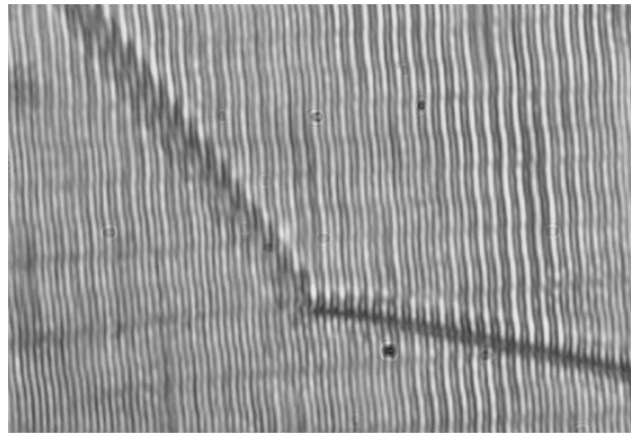
Figure 4.7. Polarization optical micrograph of a 1D SU8 nanostructure with 2 µm periodicity filled with TL213. There are obvious liquid crystal line defects within the structure.

4.3.2 Optical Spectra

Reflectance measurements of the 3D SU8 samples before and after liquid crystal infilling measured the refractive index contrast of the structures. The 1D and 2D structures do not have narrow reflectance bands like the 3D SU8 samples, so they were not studied by reflectance.   The reflectance spectra of the 3D SU8 photonic crystal with and without liquid crystal are in figure 4.8.
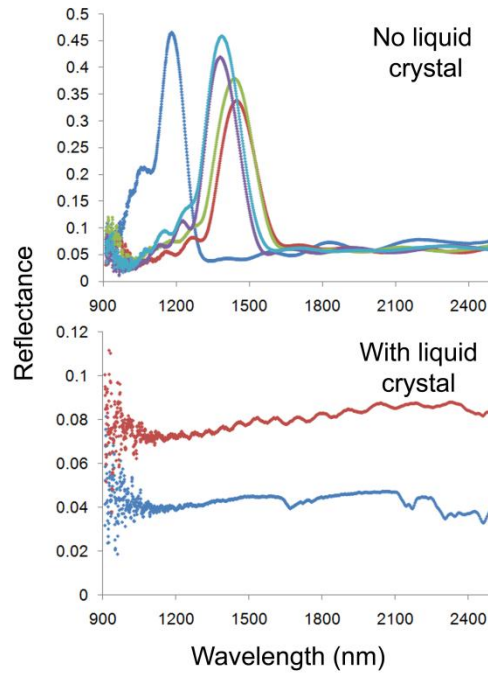
Figure 4.8. Reflectance spectra taken from different 3D SU8 photonic crystals with and without TL213 in-filling.

The reflectance spectra of the 3D SU8 photonic crystal can be modeled using the scalar wave approximation[128] of an inverse opal structure with an FCC lattice. (Modeling performed by Dr. Agustin Mihi). The 3D SU8 crystal is assumed to have a 1.6 refractive index in air, and a reflectance band near 1.2 µm. (Figure 4.9)
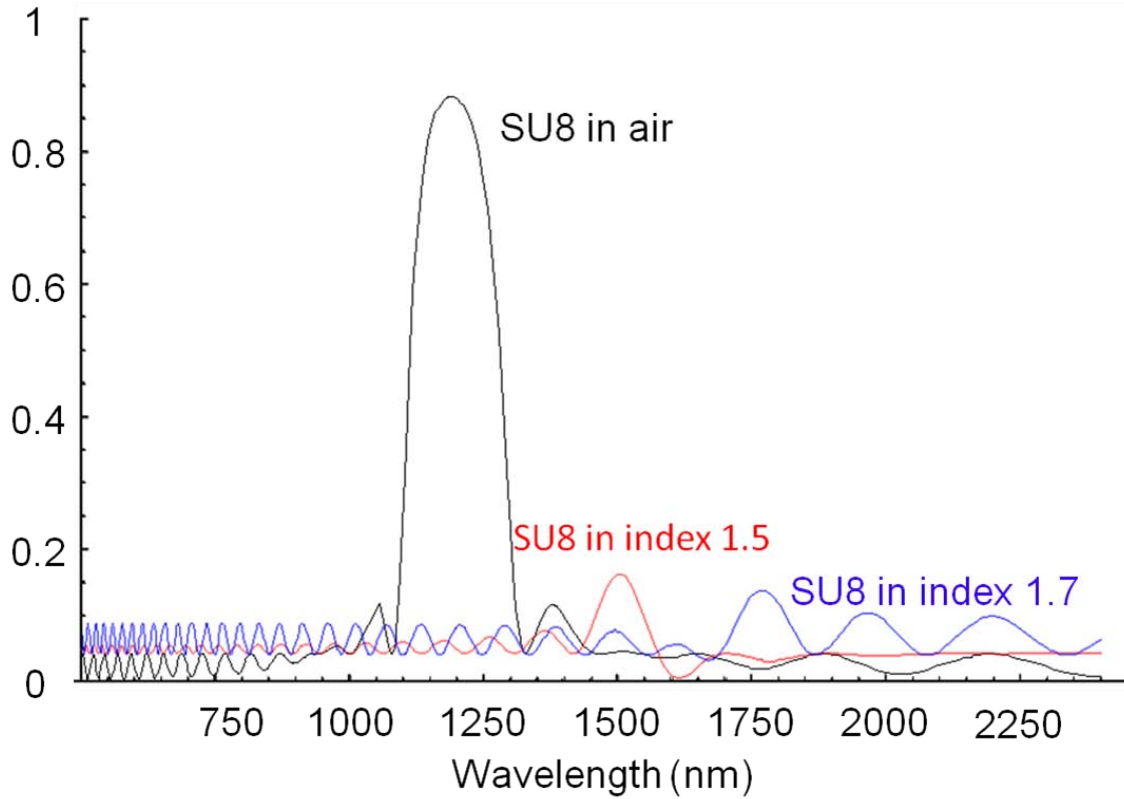
Figure 4.9. Simulated reflectance measurements of a 5 μm thick FCC SU8 photonic crystal in a) air, b) in a matrix with index 1.5, and c) in a matrix with index 1.7

The air portion of the photonic crystal with index 1 can be replaced by liquid crystal to simulate the TL213 in-filling. The index of refraction of TL213 can vary from 1.52 to 1.76. A 3D photonic crystal with index of 1.6 was therefore simulated in a matrix of index 1.5 as well as a matrix at 1.7. (Figure 4.9) Whether in-filled with a 1.5 or 1.7 refractive index, the reflection peak has a small magnitude at normal incidence which corresponds with the empirical data.

4.3.3 Diffraction Measurements

Diffraction efficiency is also an indicator of the refractive index contrast within a Bragg grating. Kogelnik's coupled-wave theory defines diffraction efficiency (DE) of a 1D sinusoidal grating as a function of the index contrast (Δn), the thickness of the sample (L), the Bragg angle (θ_B), and the probing wavelength (λ).[129]

$$DE = \sin^2(\frac{\pi \Delta n L}{\lambda \cos(\theta_B)})$$

When the grating is in-filled with birefringent liquid crystal, the index of refraction of the liquid

crystal varies depending on the orientation of the liquid crystal director. (Figure 4.10) As

voltage is used to rotate the liquid crystal it also varies the Δn, and therefore the DE.
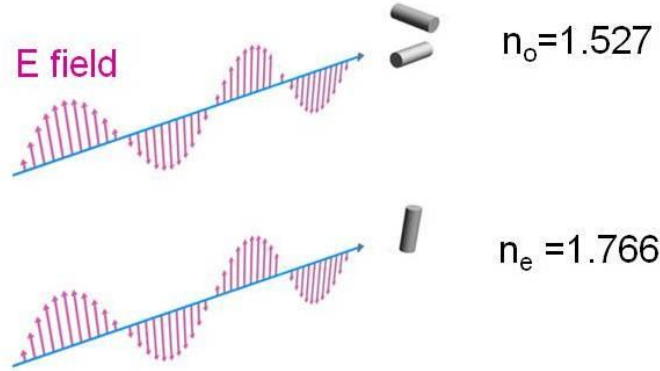
Figure 4.10. TL213 is a birefringent liquid crystal. When an incoming light wave has an electric field perpendicular to the director of the liquid crystal, the index of refraction of the TL213 is 1.527. When an incoming light wave has an electric field parallel to the director of the liquid crystal, the index of refraction of the TL213 is 1.527. Adapted from Reference 130.[130]

The DE of the in-filled 1D, 2D, and 3D SU8 samples was measured in both the on and

off state of the grating, and Δn was plotted versus voltage to measure the switching capabilities

of the nanostructures. To empirically measure the diffraction efficiency, a 532 nm laser with

vertical polarization was incident on the photonic crystals. The intensity of each diffraction spot

was measured with a power meter, and diffraction efficiency was defined as the sum of the

intensities of the transmitted non-0th orders over the sum of intensities of all of the transmitted

orders. (Figure 4.11) The incoming angle of the laser can be varied, and is measured from

normal incidence. The polarization of the incoming laser can also be altered, by inserting a half

waveplate between the laser and the photonic crystal.
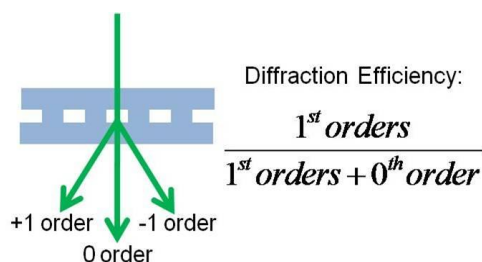
Figure 4.11. A schematic of the laser setup used to measure diffraction efficiency of the SU8 nanostructures, and the formula used to define diffraction efficiency.

Diffraction efficiency of Bragg gratings tends to have a small magnitude at normal incidence; therefore, diffraction measurements were taken at the Bragg angle of a TL213 in-filled 1D SU8 structures. (Figure 4.12) The bragg angle of the structures in Figure 4.12 was 25° off normal incidence.   5 w% octanoic acid had to be added to the TL213 as a surfactant to get the liquid crystal to switch, which indicated that liquid crystal anchoring was strong on the SU8 surface. A grating vector, gv, was defined for ease in describing orientations of the incoming laser electric field, liquid crystal orientation, and orientation of the SU8 features. For the 1D case, the grating vector was perpendicular to the SU8 planes. (Figure 4.12) When DE was measured with incident light polarized perpendicular to the grating vector, there was a very small change in DE as voltage was applied. However, when light polarized parallel to the grating vector was used, there was a large variation in DE as voltage was applied. The results suggest that the 1D in-filled SU8 structures could useful as a switchable bragg grating as the DE can be varied from 70% to nearly 0% with the application of an electric field. The polarization dependence of the DE indicates that the liquid crystal directors most likely lie along the direction of the grating vector when no voltage is applied, but rotate perpendicular to their original positions (out of the page in Figure 4.12a) when the voltage is applied. The diffraction

efficiency is over-modulated in Figure 4.12b because the indices of the SU8 and liquid crystal were not matched perfectly.

Figure 4.12. a) Top-down SEM micrograph of a 1D Bragg grating fabricated in SU8 on an ITO coated glass substrate with a 600 nm periodicity. The grating vector is defined as gv. The Bragg angle is at 25 degrees. b) Diffraction efficiency of the TL213 in-filled SU8 nanostructure for incoming light with polarizations parallel and perpendicular to the grating vector as a function of the voltage applied. c) Cross-section SEM micrograph of the 1D Bragg grating fabricated in SU8 on an ITO coated glass substrate with a 2.5 micron thickness.

The same experiment was completed on the TL213 in-filled 2D SU8 nanostructure with 600 nm periodicity. (Figure 4.13) DE was measured with incident light polarized perpendicular and parallel to the grating vector as voltage was applied. In both cases the DE did not change much, even at high voltages. This suggests that the liquid crystal is either confined in the 2D structure, strongly anchored onto the surface of the SU8, or that the anchoring orientation of the liquid crystal is in the same direction as the applied electric field. The two polarizations are

relatively symmetric which suggests a radial distribution of the liquid crystal inside of the 2D cylinders.

Figure 4.13. a) Top-down SEM micrograph of a 2D Bragg grating fabricated in SU8 on an ITO coated glass substrate with a 600 nm periodicity. The grating vector is defined as gv. The Bragg angle is at 23 degrees. b) Diffraction efficiency of the TL213 in-filled SU8 nanostructure for incoming light with polarizations parallel and perpendicular to the grating vector as a function of the voltage applied. c) Cross-section SEM micrograph of the 2D Bragg grating fabricated in SU8 on an ITO coated glass substrate with a 2.5 micron thickness.

The positive dielectric liquid crystal was not able to switch inside of the 2D cylinders, but would a negative dielectric liquid crystal be able to? A negative dielectric liquid crystal called 2079 was in-filled inside of a sample with the same dimensions as the previous 2D sample. The same experiment was performed and the results are in Figure 4.14. The diffraction efficiency varied with electric field, but the threshold voltage for switching was high. This indicated that the TL213 liquid crystal was probably not confined within the SU8 nanostructure, but rather just

oriented in the same direction as the applied field. Surface anchoring was probably strong in the 2709 in-filled nanostructures because the threshold switching voltages were high.
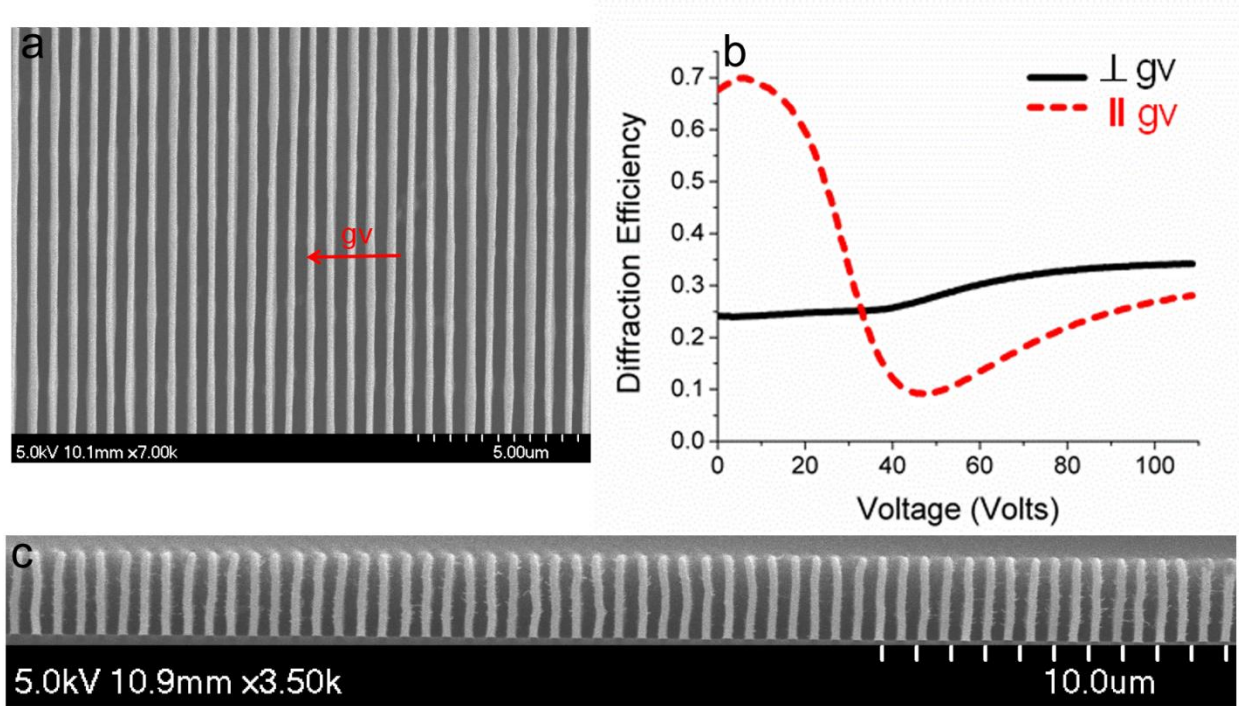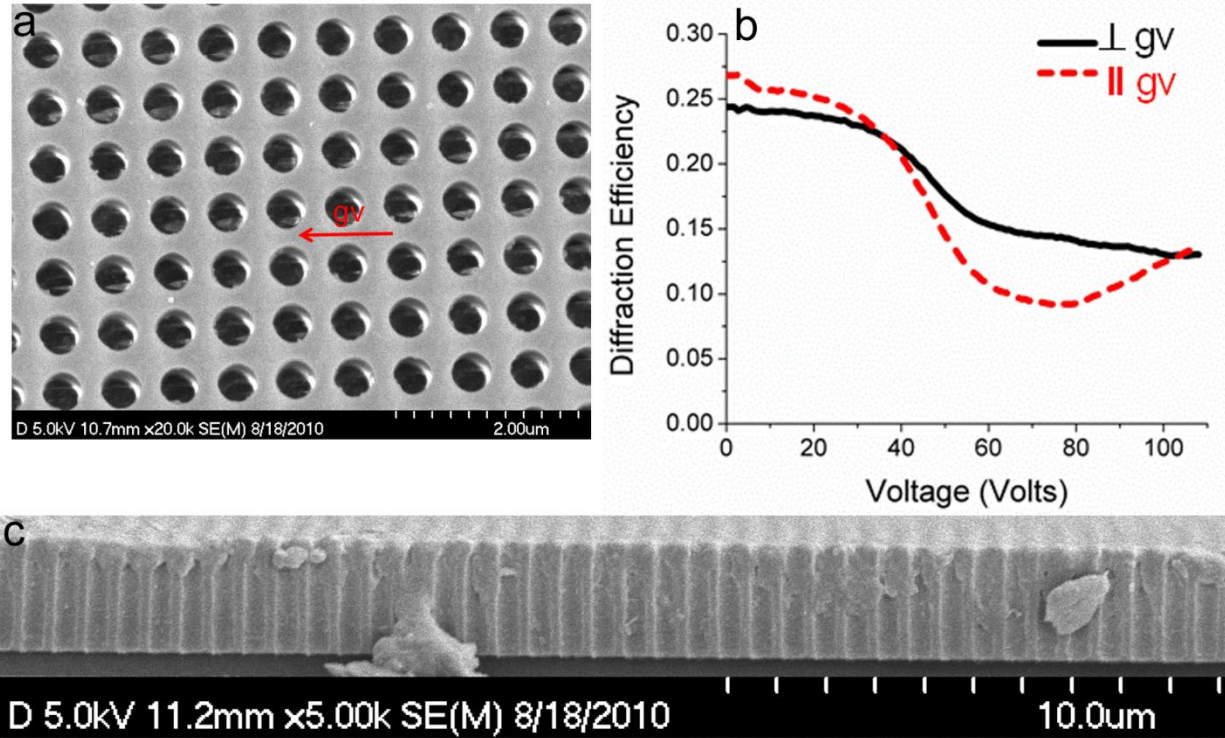

Figure 4.14. a) Top-down SEM micrograph of a 2D Bragg grating fabricated in SU8 on an ITO coated glass substrate with a 600 nm periodicity. The grating vector is defined as gv. b) Diffraction efficiency of the 2709 in-filled SU8 nanostructure for incoming light with polarizations parallel and perpendicular to the grating vector as a function of the voltage applied. c) Cross-section SEM micrograph of the 2D Bragg grating fabricated in SU8 on an ITO coated glass substrate with a 2.5 micron thickness.

Finally, DE measurements were taken at the Bragg angle of the 3D SU8 samples. (Figure 4.15) The DE fluctuated with the application of an electric field with both polarizations of incoming light. The two orthogonal polarizations of the incoming beam resulted in DE measurements that were compliments of each other. The initial increase or decrease in the DE at 10V was apparent in each diffracted beam and was due to liquid crystal switching. The reflections of the diffracted beams increased or decreased just as the transmitted diffracted beams did.
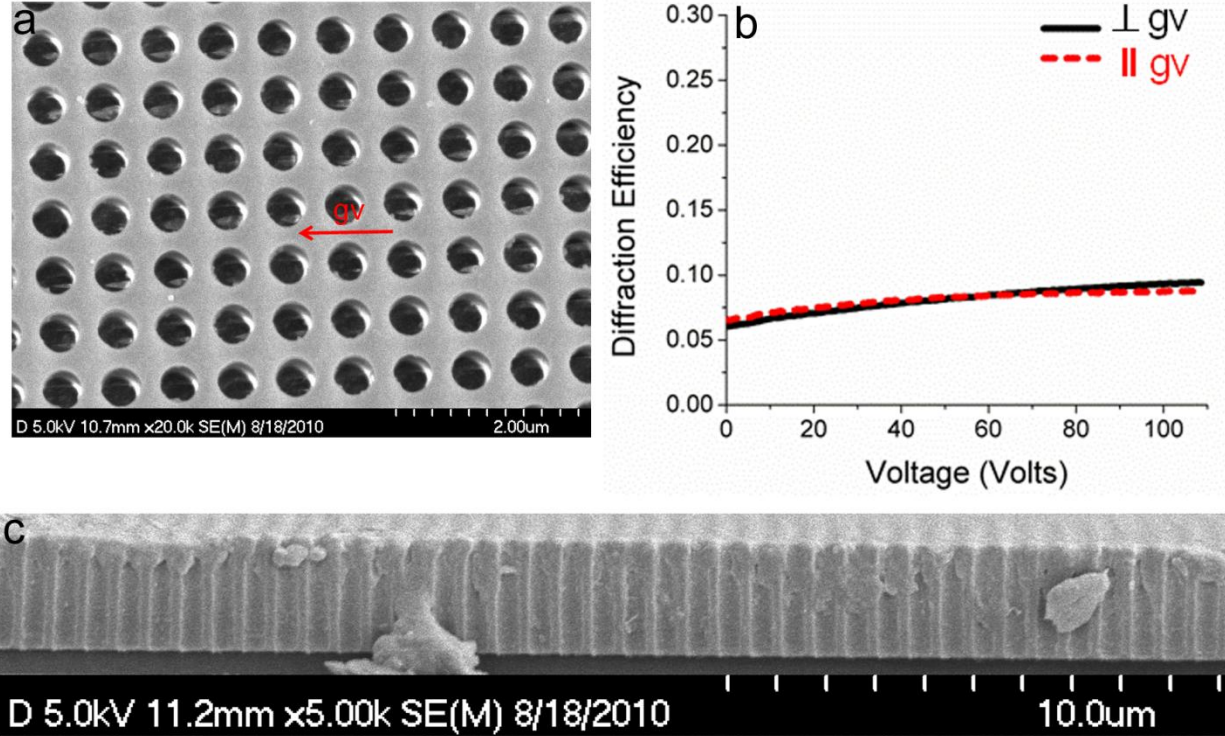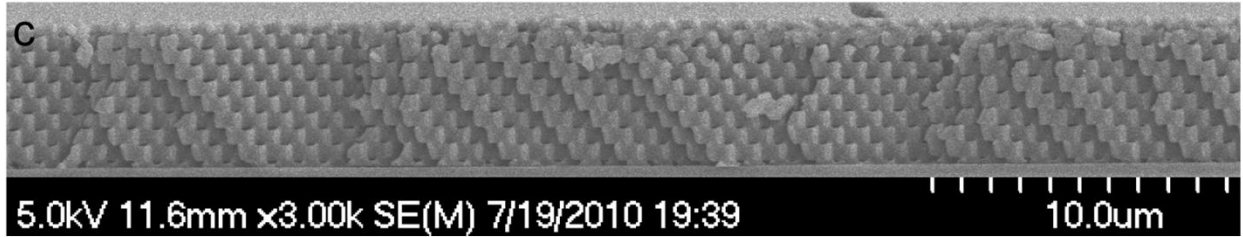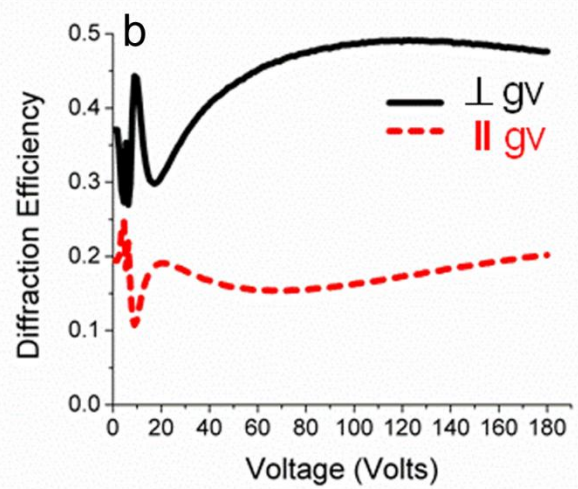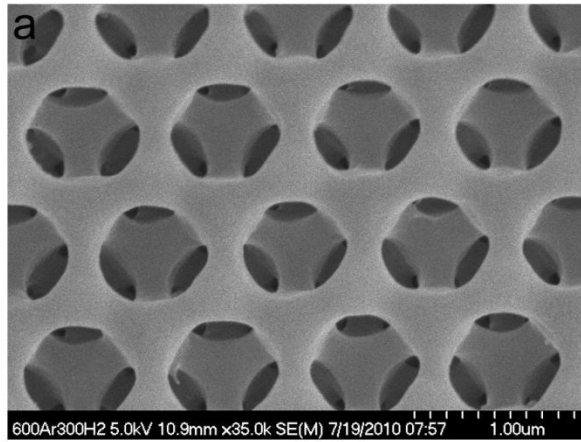
Figure 4.15. a) Top-down SEM micrograph of a 3D Bragg grating fabricated in SU8 on an ITO coated glass substrate. The Bragg angle is at 17 degrees. The grating vector is defined as gv . b) Diffraction efficiency of the TL213 in-filled SU8 nanostructure for incoming light with polarizations parallel and perpendicular to the grating vector as a function of the voltage applied. c) Cross-section SEM micrograph of the 3D Bragg grating fabricated in SU8 on an ITO coated glass substrate with a 5 micron thickness.

The diffraction efficiency of each sample was also measured as a function of the incident angle of the laser on the SU8 photonic crystal. (Figure 4.16a) Each sample had a very broad angular selectivity which can be attributed to the shape of the grating as well as the high aspect ratio. The angular selectivity of similar structures was modeled using coupled wave theory, and predicted the broad angular selectivities.[131-132] The angular selectivity of the 1D sample was also measured as a function of the voltage applied to the sample. (Figure 4.16b) The feature in the DE around -7° is a type of Wood's anomaly.[133]
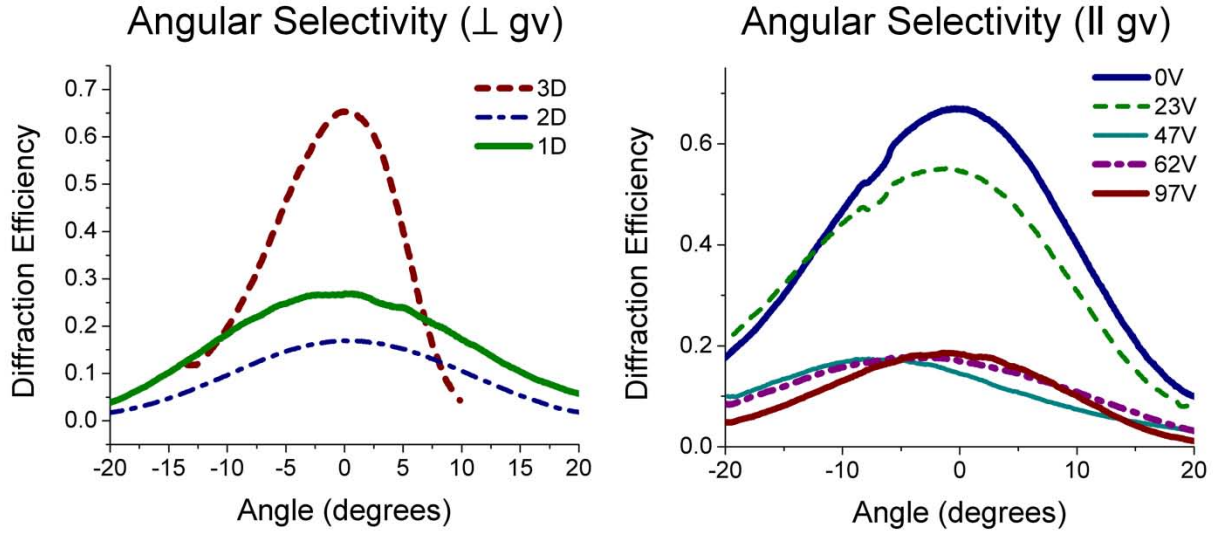
Figure 4.16. a) Angular selectivity curves for 1D, 2D, and 3D SU8 samples. b) Angular selectivity curves of the 1D SU8 sample at various applied voltages.

4.4 Conclusions and Future Directions

Liquid crystal switching within SU8 photonic crystals has been studied. The geometry of the photonic crystal affects the switching capability of the liquid crystal. 1D and 3D SU8 nanostructures were successfully switched after infiltration by the positive dielectric liquid crystal, TL213. The 2D SU8 structure could not be switched using the TL213, but instead a negative dielectric liquid crystal was used to make the photonic crystal active. There is strong surface anchoring of the TL213 onto the surface of the SU8 which can be reduced by adding surfactant. There is not a large index contrast between the liquid crystal and the SU8 photonic crystal. For applications where high index contrast is necessary, the SU8 structure should be inverted to another material.

CHAPTER 5

MULTIFUNCTIONAL SELF-HEALING

5.1 Introduction

The human body has the ability to heal damage like cuts and wounds on the skin. If non-living material systems had the same ability to repair themselves, it would increase the lifetime of coatings that prevent corrosion, structural supports of a bridge, or even electronics. Materials that are engineered to repair damage without any human intervention are called ―self- healing materials." The two typical methods used for autonomic repair of cracks within polymeric systems use encapsulated healing agents[134-136] or microvascular networks[137-139] to bring more material into the area of damage. The encapsulation approach involves adding microcapsules that contain a healing agent into the matrix of a material. When the matrix is damaged, the capsules are ruptured, releasing the healing agent into the crack plane. The healing agent can be excess monomer, but to ―self-heal" the matrix, the monomer must only polymerize when damage has occurred. Typically microcapsules containing a polymerization catalyst are added into the material along with the microcapsules containing the excess monomer, so when damage is imparted on the material, both capsules rupture at the same time to initiate polymerization. Figure 5.1gives a schematic of the self healing process.[140-141] The size, concentration, and type of material for each microcapsule is engineered depending on the end application. In this case, the self healing coating was used to prevent corrosion of metallic surfaces.
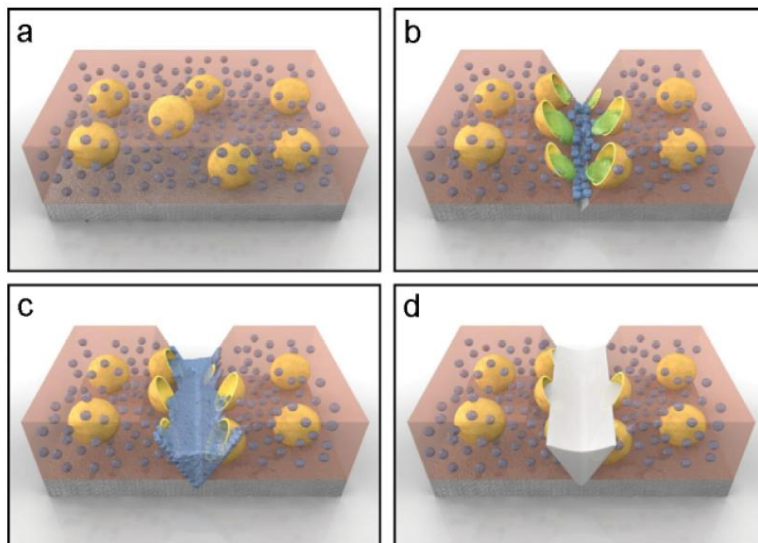
Figure 5.1. Schematic of self-healing process. a) Self-healing coating containing microencapsulated catalyst (yellow) and phase separated healing-agent droplets (blue) in a matrix (light orange) on a metallic substrate (grey). b) Damage to the coating layer releases catalyst (green) and healing agent (blue). c) Mixing of healing agent and catalyst in the damaged region. d) Damage healed by cross-linked polymer, protecting the substrate from the environment. Schematic taken from *Advanced Materials*, **21**, 645-649 (2009).[140-141]

Another method uses a continuous network of healing agent filled channels, or a ―microvascular network,‖ to bring healing agent to the crack plane. This type of system mimics the interconnected network of blood vessels and capillaries that the human body uses to heal itself. (Figure 5.2)
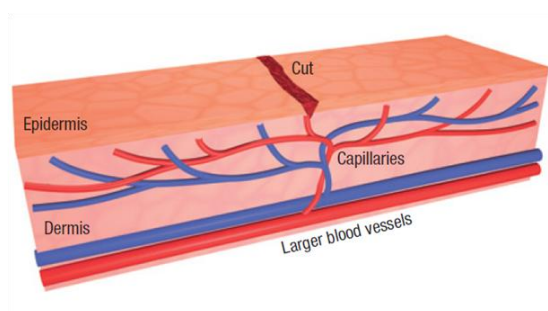
Figure 5.2. Schematic of an interconnected network of blood vessels and capillaries in the dermis of the human body, which is used to heal damage to the skin. Schematic taken from *Nature Materials*, **6**, 582 (2007)

Just as the body can heal multiple cuts made on the same area of the skin, microvascular networks can heal multiple times within one volume of the material due to the reservoir of healing agent. The fabrication of a microvascular network is a multistep process. A fully interconnected 3D network must first be fabricated out of a material that can be burned or melted out of the matrix material. The network is then embedded within an uncured matrix and catalyst mixture, and cross-linked. Then the matrix is heated and placed under light vacuum to create a series of connected pipes within the matrix. The open tubes are then filled with healing agent, and the sample is completely sealed shut. For large scale processing it would be optimal to create this interconnected network out of healing agent in a single step, rather than melting out and refilling the network.

Interference lithography will be used to form 3D interconnected networks of monomer within a polymer matrix in a single step for self- healing coatings. A photopolymerizable monomer and a reaction monomer will be mixed and used as a template to record a laser interference pattern. As the photopolymerizable monomer begins to crosslink, the reaction monomer will be sequestered into the regions of destructive interference. Not only does interference lithography have the advantage of forming self-healing coatings in one step, it also creates a periodic change in the index of refraction that causes large reflections of a single wavelength of light. The periodicity of the structures can be engineered to tune the reflected wavelength to the visible region of the spectrum, and this can be used to detect damage within the system. One disadvantage of this system is that the catalyst cannot be incorporated into the thickness of the structure. Rather than using a catalyst, moisture from the environment will catalyze the polymerization of the healing agent.

5.2 Synthesis of Thermally-Healed Coatings by Interference Lithography

To make the self- healing coatings, acrylate and isocyanate monomers were mixed together into a homogonous resin. The components added to the uncured resin are listed in Table 1.

% by weight	Component
0.5	ammonium cerium(IV) nitrate salt (CAN)
20.0	trimethylolpropane triacrylate (TMPTA)
0.9	diiodofluorescein
1.8	2,6-Diisopropyl-N,N-dimethylaniline (DIDMA)
75.9	isophorone diisocyanate (IPDI)
0.9	50µm glass spheres

Table 5.1. Components of the photocurable resin used to create thermally- healed coatings.

All of the components except the IPDI and glass spheres were mixed together with excess ethanol to solubilize the powdered chemicals. The IPDI was not added until after the ethanol was removed by rotovap to protect the isocyanate groups from reacting with the hydroxyl groups. TMPTA was chosen because it was a tri-functional acrylate with minimal residual hydroxyl groups left from purification of the monomer. TMPTA would serve as the polymeric matrix, encapsulating a network of monomeric IPDI, or healing agent. The 50 µm glass spheres were spacers to keep the thickness of the coating uniform.

Once the resin was mixed together homogeneously, it was holographically exposed in a Bragg geometry at 200 mW for 30 sec with a 532 nm laser. Upon exposure, the diiodofluorescein and DIDMA served as initiators to free radical polymerize the TMPTA. (Figure 5.3) As the TMPTA polymerizes, the monomeric IPDI sequesters into the regions of destructive interference because IPDI is a reaction monomer that does not polymerize in the

presence of the free radicals. The final result was planes of monomeric IPDI encased in a

TMPTA matrix. A SEM and TEM of a one- dimensional grating written into in this manner can

be seen in figure 5.4.

$$I \xrightarrow{hv} 2R\cdot$$
$$R\cdot + M \rightarrow M_1\cdot$$

$$M_1\cdot + M \rightarrow M_2\cdot$$
$$M_n\cdot + M \rightarrow M_{n+1}\cdot$$

$$M_n\cdot + M_m\cdot \rightarrow M_{n+m}$$
$$M_n\cdot + M_m\cdot \rightarrow M_n + M_m$$
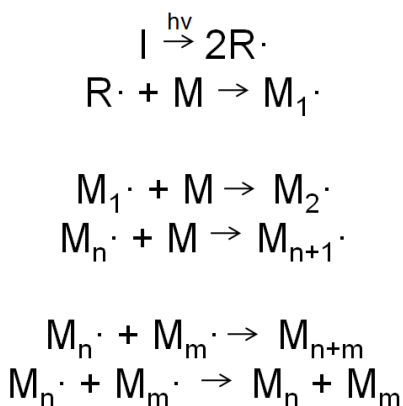
Figure 5.3. A generic photoinitiated free radical reaction mechanism. I is the initiating species, R is a radical, and M is a monomeric species.
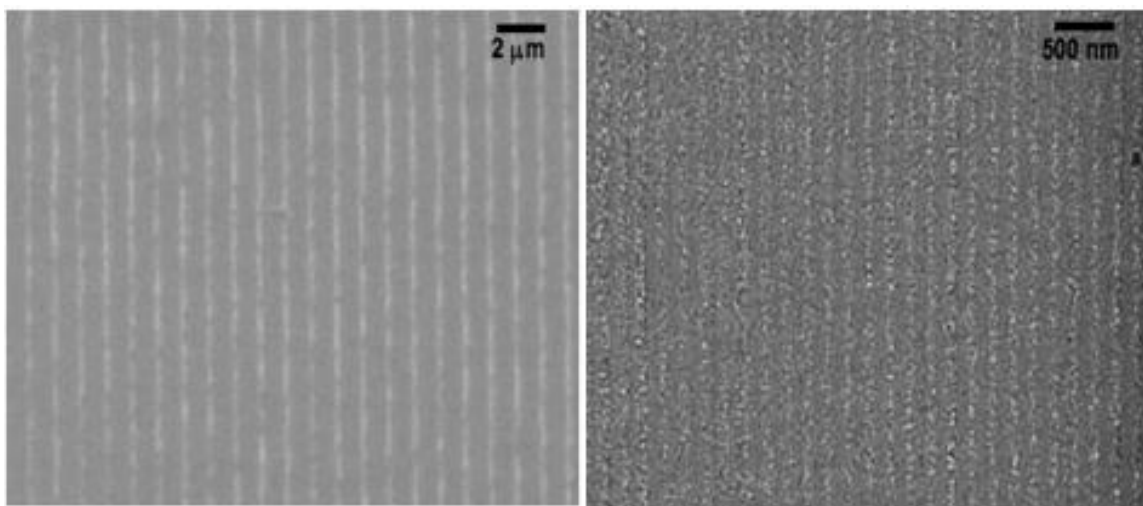
Figure 5.4. a) SEM top-view of a transmission grating recorded by a 532nm laser into a 50:50 mixture of isophorone diisocyanate and trimethylolpropane triacrylate. b) TEM microtomed cross-section of a reflection grating recorded by a 532nm laser into a 40:60 mixture of isophorone diisocyanate and pentaerythritol tetraacrylate.

To further evidence that the IPDI remained monomeric after the photopolymerization, FTIR of the mixture was taken before and after exposure to a 532 nm light. The NCO peak at 2350 cm^{-1} remained after 17 min of exposure to a green laser. (Figure 5.5)
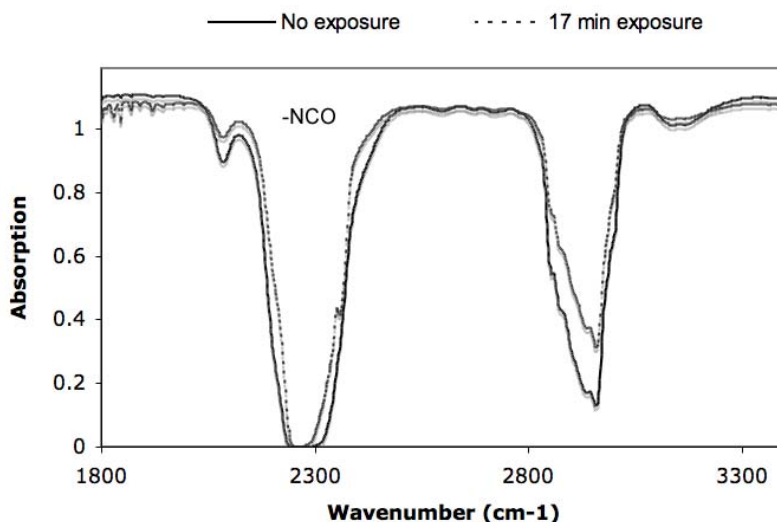
Figure 5.5. FTIR spectrum of an acrylate and diisocyanate photoreactive resin before photopolymerization, and after 17 min of exposure to 532nm light. The isocyanate -NCO peak is around 2350 cm^{-1}. Despite the polymerization of the acrylate, the –NCO peak is still evident.

Even though the IPDI monomer and TMPTA polymer formed the desired geometry within the coating, it would not self heal when damaged. The monomeric IPDI should leak from the crack when damaged, and the water in the environment was supposed to act as a catalyst for isocyanate polymerization . Isocyanates are known for their reactivity with moisture (Figure 5.6); however, the IPDI monomer, or other aliphatic isocyanate monomers, would not polymerize quickly enough with moisture in the air to heal the coating within hours. Since the coating would not heal itself, it was heated to 95°C for 30 min to promote the polyaddition reaction between the leftover hydroxyl groups and the isocyanate monomer.[142] CAN was also added to the coating, so when the coating was heated it would initiate radical polymerization of unreacted acrylate groups.[142] Even though the hydroxyl groups were limited in the preparation of the resin,

there were enough within the mixture to polymerize the isocyanate. Using this thermally healing

system as a proof of concept, samples were fabricated, damaged, and then heated to determine if

isocyanate would flow into the crack plane.

$$R-N=C=O \ + \ H_2O \ \xrightarrow{\text{Step 1}} \ R-N-\overset{\overset{\displaystyle O}{\|}}{\underset{\underset{\displaystyle H}{|}}{C}}-O-H$$

$$R-N-\overset{\overset{\displaystyle O}{\|}}{\underset{\underset{\displaystyle H}{|}}{C}}-O-H \ \xrightarrow[\text{decomposes}]{\text{Step 2}} \ R-NH_2 \ + \ CO_2^{\text{gas}}$$

$$R-N=C=O \ + \ R-NH_2 \ \xrightarrow{\text{Step 3}} \ -R-\overset{}{\underset{\underset{\displaystyle H}{|}}{N}}-\overset{\overset{\displaystyle O}{\|}}{C}-\overset{}{\underset{\underset{\displaystyle H}{|}}{N}}-R-$$
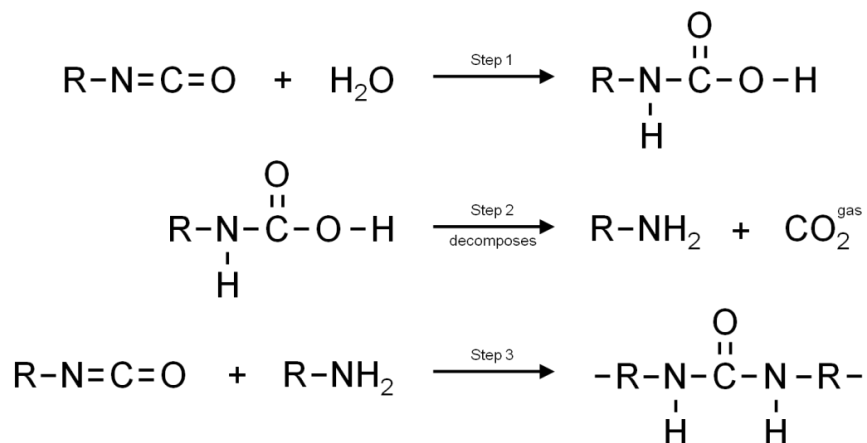
Figure 5.6. The mechanism for isocyanate polymerization when exposed to water.

50 μm coatings were fabricated in Bragg reflection geometry using interference

lithography. The first sample was made using the prescribed composition from Table 5.1 and

polymerized at 200 mW for 30 sec. The second sample was made exactly the same, except the

IPDI monomer was left out of the resin before photopolymerization. Each sample was cured

under a white light for 5 min after holographic exposure, and then the samples were opened to

the air, cut with a razor blade, and immediately placed on a 95°C hotplate for one hour. After

heating, the samples were coated with gold and a SEM was used to look at the surface of the

coatings. (Figure 5.7) The sample without isocyanate did not show any evidence of healing, but

the sample containing isocyanate did show that isocyanate had leaked into the crack plane. This

result shows promise that interference lithography could be used to create self-healing coatings;

however, the isocyanate reaction rate with water must be increased so thermal intervention is not

needed.

89
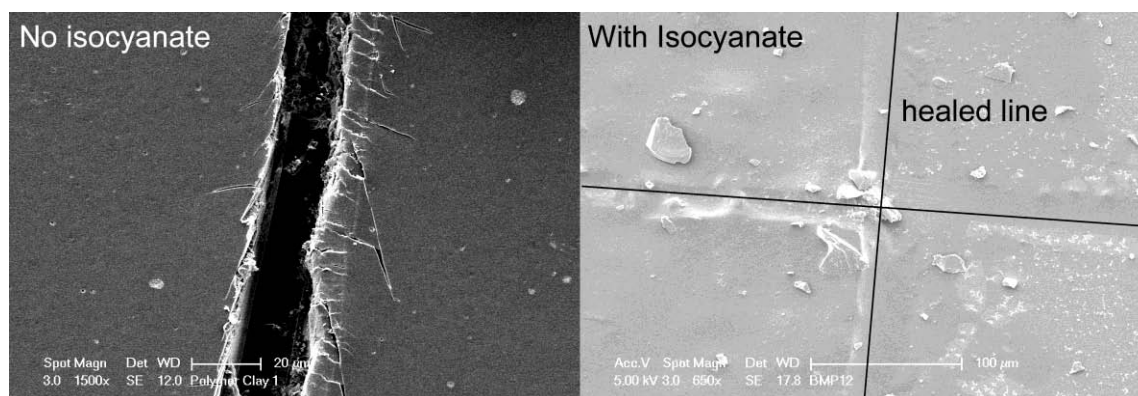
Figure 5.7. SEM micrographs of an acrylate coating and an acrylate/isocyanate coating fabricated by interference lithography.   Each sample was scratched by a razor blade and then heated to 95ºC. The sample without any isocyanate showed no healing, while the sample containing isocyanate did show healing.

SEM micrographs of the reflection grating were also taken on the edge of the interference region of the sample to see how the isocyanate monomer and acrylate polymer structure when there was no interference pattern. (Figure 5.8) In the regions exposed to the interference pattern, there were alternating planes of isocyanate and acrylate parallel to the substrate, so only the top plane of acrylate monomer was seen by the SEM. However, in the regions exposed to a homogenous beam the isocyanate monomer still phase separated from the acrylate polymer.   It is interesting to note that when a crack formed in the homogenously exposed region of the sample, only parts of the crack that passed through the isocyanate phases were healed. This shows that the geometry of the interferogram is important when engineering self-healing samples.
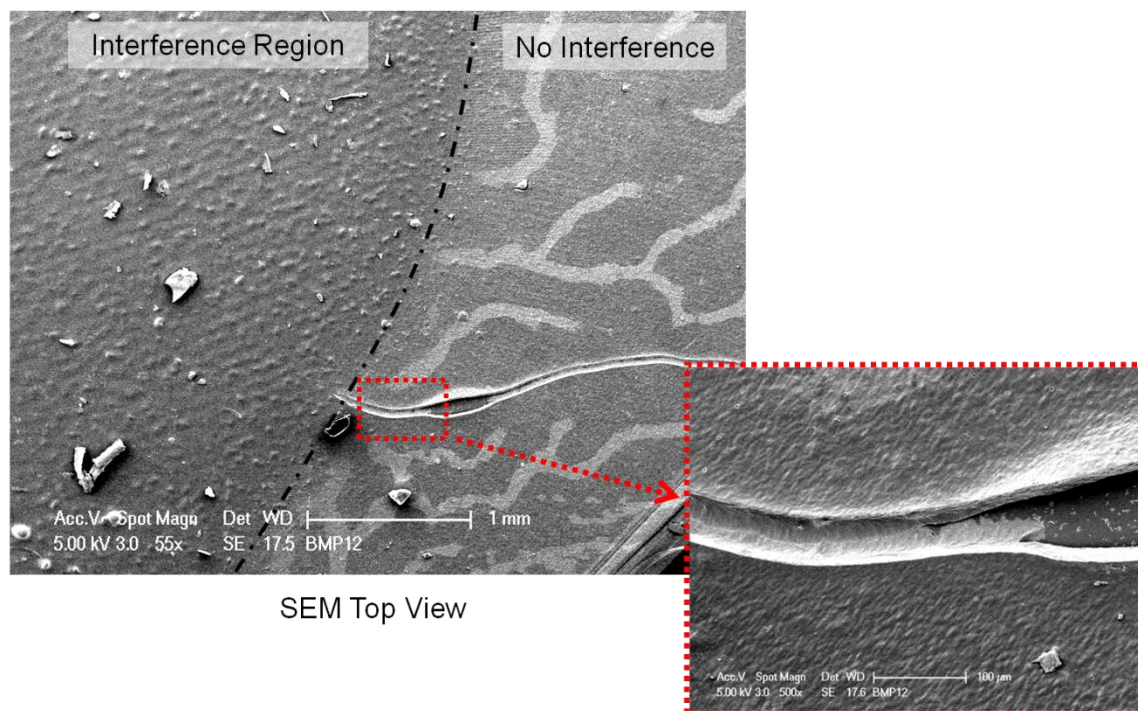
Figure 5.8. SEM micrograph of the edge of a Bragg reflection grating composed of alternating planes of isocyanate monomer and acrylate polymer. The sample was heated to 90°C for one hour to polymerize the isocyanate before SEM. The left side shows an area of the sample that was exposed to the 1D interference pattern, while the right side was only exposed to homogenous light. The inset is a higher magnification of a crack that runs through the area exposed to a homogenous beam. Only regions passing through the white isocyanate phases of the sample were healed.

5.3 Autonomic Readout

Another feature of this system is that the layered monomer/ polymer structure causes a periodic change in the index of refraction, or a stop band to open up in the transmission spectra of the sample. The wavelength of the stop band of the sample can be engineered by changing the periodicity of the TMPTA and IPDI. The periodicity was set around 200 nm so that visible green light was reflected from the sample. The isocyanate monomer was carefully chosen so that the index of refraction of the monomer form of the isocyanate was about 0.05 lower than the acrylate polymer index of refraction. When heat was applied to polymerize the sample, the isocyanate monomer polymerized causing its index if refraction to increase by about 0.05. In

doing so, the periodic change in the index of refraction was lost, and the sample no longer

reflected green light. The coating changing color from green to clear can be used as a

mechanism to readout when damage has occurred. A schematic of this system is in figure 5.9.
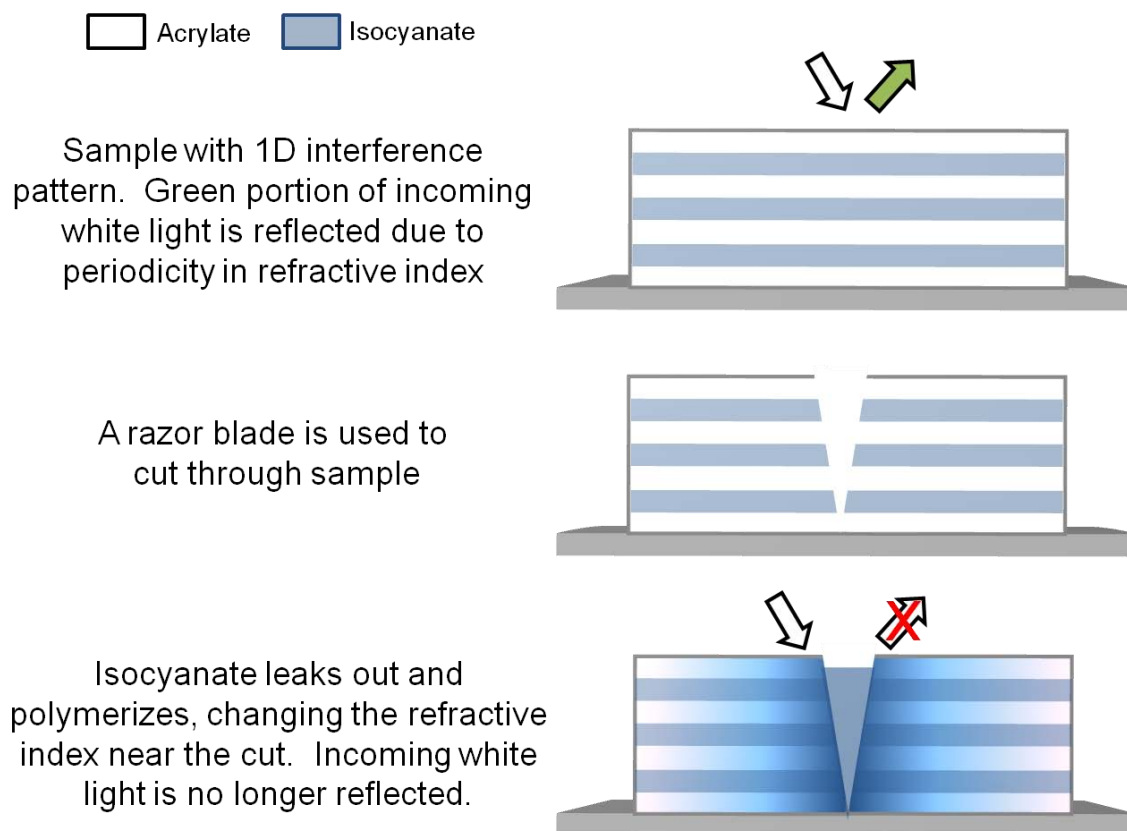
Figure 5.9. Schematic of proposed multifuncational self- healing coating. Interference lithography is used to create the layered isocyanate/acrylate structure. The thickness of each period determines the wavelength reflected by the structure. A razor blade can then be used to damage the coating, which causes the low- viscosity isocyanate to leak out into the crack. Upon exposure to water, the isocyanate polymerizes, its index increases by about 0.05 causing the coating to appear clear.

One 12 micron thick reflection grating was fabricated with interference lithography

composed of acrylate polymer and isocyanate monomer. The transmission spectrum of the green

sample was measured after fabrication and is shown in Figure 5.10. The sample was then heated

to 95°C for one hour to polymerize the isocyanate, and the transmission spectrum was measured

again. There was an obvious decrease in the height of the stop band and the sample appeared

clearer.
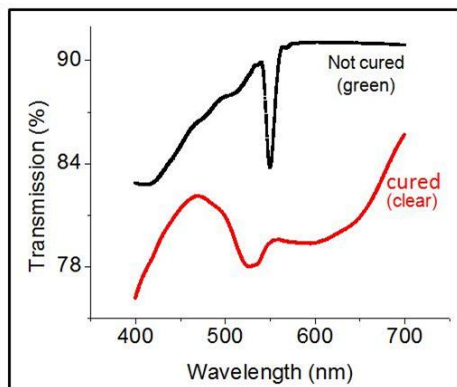
Figure 5.10. Transmission spectra of 12 μm thick reflection gratings containing isophorone diisocyanate, pentaerythritol tetraacrylate, and a cerium salt catalyst (39:60:.7). The black curve is transmission spectra for an uncured sample while the red curve is for a sample cured at 95°C for 1 hour.

5.4 Autonomic Repair

With the ability to easily create periodic encapsulated monomer domains within a

polymer matrix and to autonomically readout when damage has occurred, the next step is to

engineer a method for self-healing of the coating. Since the moisture in the air was not enough

to catalyze IPDI polymerization at room temperature, there are a few options for creating a self-

healing coating. The first option is to spincoat a chemical containing free amine or hydroxyl

groups onto the surface of the coating, so when the sample is damaged, the catalyst mixes with

the leaked isocyanate and polymerizes. This is an easy way to make a self-healing coating, but it

also involves adding more steps to the process and it loses the novelty of having a catalyst free

system. However, the isocyanate within the coating will be stable for long periods of time.

Another option is to use an isocyanate that reacts more readily with water. For instance,

aromatic isocyanates or polyisocyanates polymerize within hours of exposure to the moisture in

the air. The chemistry is more difficult and the lifetime of the isocyanate within the coating

probably will not be more than 6 months, but it would be a moisture-catalyzed system. Further

research was done using isocyanates with greater reactivity with water.

Isocyanates that have greater reactivity with water are typically aromatic like methylene

diphenyl diisocyanate (MDI), toluene diisocyanate (TDI), and polyisocyanates. A chart of the

properties of some commercially available isocyanates is in Table 5.2, with the unfavorable

properties listed in red. The perfect isocyanate monomer for this application would be clear and

transparent so that the laser interference pattern would not be attenuated. It would fully

polymerize in air within 12 hours, for quick healing of the coating. It would also have a low

viscosity, so that the isocyanate monomer could be sequestered into the destructive interference

regions when exposed.   Finally, the isocyanate cannot foam when exposed to air. Figure 5.6

gave the mechanism for isocyanate polymerization with water, and carbon dioxide is a byproduct

of the reaction. If the isocyanate polymerizes very quickly, the CO_2 becomes trapped within the

film and causes bubbles or foam.

	TDI	Desmodur 75L	Desmodur XP2410	Pelucid (sealant)	Desmodur MP210
Main isocyanate component	TDI	Polyisocyanate TDI	Polyisocyanate HDI	Unknown polyisocyanate	Polyisocyanate MDI
Color	Clear	Clear	Clear	Clear	Yellow
Polymerize in air in 12 hours?	Yes	Yes	No	Yes	Yes
Visocsity (mPa·s)	5	~1600	~700	~200	~300
Foam?	Yes	No	No	No	No
Soluble w/ photo-initiator	Yes	Yes	Yes	No	Yes

Table 5.2. Table of isocyanate characteristics.

The pure TDI monomer cannot be used because it reacts with water so readily that it foams. The Desmodur 75L has a high viscosity, but if it can be incorporated into the coating using interference lithography then it is a possibility. The Desmodur XP2410 is an aliphatic polyisocyanate, and despite the oligomers, it does not polymerize readily in air. Pelucid is a commercial polyurethane wood floor sealant that dries in air. It leaves a nice coating, but the diiodoflurescein photoinitiator is not miscible in it. The photoinitiator can be changed, but it may be easier to do the fabrication in the UV where there are many photoinitiators to choose from. Finally, the Desmodur MP210 has a dark yellow color which may attenuate the laser during the writing of the coating. The most promising isocyanate for the self-healing coating is the commercial Pelucid using a UV initiator, or the Desmodur 75L with added components to reduce the viscosity.

The isocyanate needs to phase separate from the acrylate when exposed, it needs to be able to form a grating for autonomic readout, and it needs to leak into the crack plane when damaged. The first possible chemistries were tried with the Pelucid monomer. 0.005 g Diiodofluorescein, 0.01 g DIDMA, 0.2 g ethanol, 0.5 g acrylate monomer (either TMPTA or Dipentaerythritol penta-/hexa-acrylate), and 1 g Pelucid were used to create the resin. First the diiodoflurescein, ethanol, and acrylate monomer were mixed together homogenously. The smallest possible amount of photoinitiator was used so that the insolubility between the didiofluorescein and Pelucid was minimized, but free radical polymerization would still occur when exposed.   Ethanol was obviously an odd choice for solvent because it contains hydroxyl groups that will make the Pelucid polymerize. It was used because it had high solubility with the photoinitator and acrylate monomers, but it was rotovaped out of the mixture before the addition of the Pelucid. The DIDMA was added after rotovaping, and the vial was placed in an argon

atomosphere glove box where the Pelucid was added. A drop of the resin containing the

TMPTA monomer was placed between two glass slides and exposed to a transmission grating at

200 mW for 60 sec. There was no visible Bragg grating. After exposing the unpolymerized

resin to air, it remained clear and did not foam. Another sample was made using the

Dipentaerythritol penta-/hexa-acrylate monomer and polymerized under the same conditions.

This monomer typically forms a grating due to the high number of acrylate groups, but it also

contains penta and tri acrylate functional molecules which have hydroxyl groups that might

compromise the stability of the Pelucid. This sample did form a nice grating, but when the

sample was opened and exposed to air, it immediately turned white due to foaming. (Figure 5.11)

The foaming seems to be due to the mixture of the Pelucid with Dipentaerythritol penta-/hexa-

acrylate) polymer or the confinement of small volumes of Pelucid inside of the polymer.   The

same experiment was done with acetone rather than ethanol to reduce the number of hydroxyl

groups. The TMPTA sample did not polymerize when exposed and the hex-acrylate sample

formed a grating that foamed when exposed to air.

Figure 5.11. a) Photograph of a transmission grating of a sample containing 0.005 g Diiodofluorescein, 0.01 g DIDMA, .5 Dipentaerythritol penta-/hexa-acrylate), and 1 g Pelucid that was polymerized at 200 mW for 1 min. b) Photograph of the same sample after exposure to air.

Silicone oil can be added to isocyanate chemistries as an anti- foaming agent.[143] 0.2 grams of silicone oil were mixed into the previously described hexacrylate/ Pelucid system, and it did reduce the amount of foaming, but not enough to maintain a clear coating. Adding more silicone oil resulted in phase separation of the resin before photopolymerization. Instead of trying different anti-foaming agents, the isocyanate monomer was varied. The acrylate monomer was not varied because most multi-functional acrylate monomers , other than TPMPTA, contain hydroxyl groups.

Further research on self-healing coatings used Desmodur 75L as the healing agent. 0.005 g Diiodofluorescein, 0.01 g DIDMA, 0.2 g actone, 0.5 g Dipentaerythritol penta-/hexa-acrylate), and 1 g Desmodur 75L were prepared as done with the Pelucid. The viscosity of the resin was very high. The samples were exposed to a transmission grating interferogram at 200 mW for 60 sec. A grating did form, and when the grating was exposed to air, it did not foam. Some of the diffraction efficiency of the grating was lost over time, but the grating never went completely clear. (Figure 5.12) The same procedure was duplicated with Desmodur MP 210 and the results were similar.
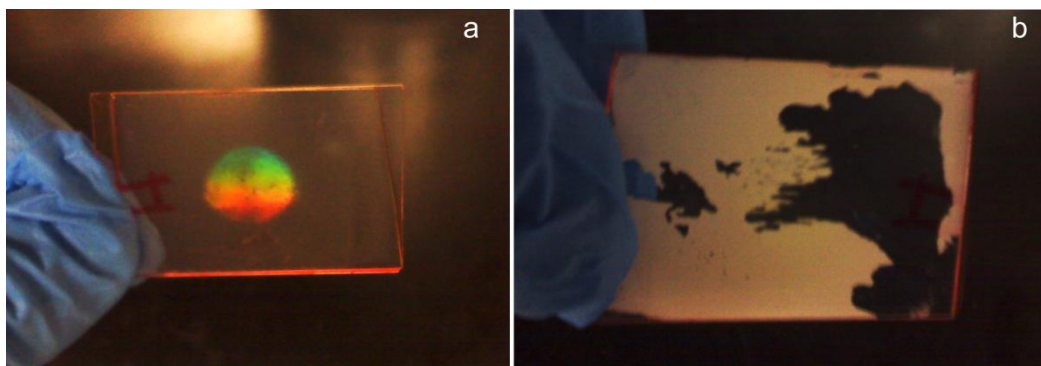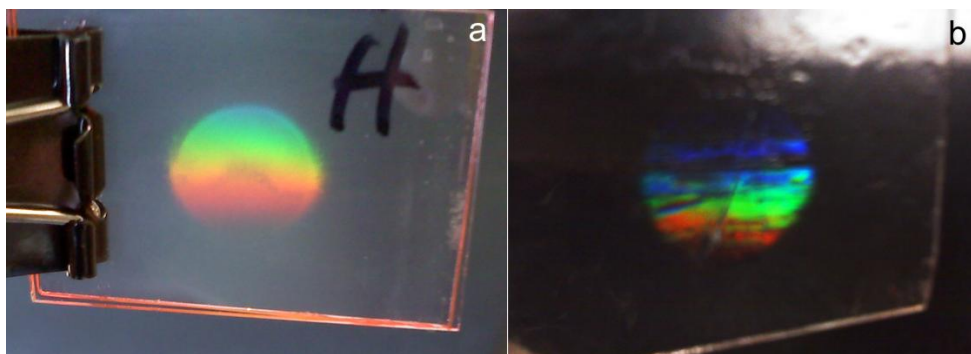

Figure 5.12. a) Photograph of a transmission grating of a sample containing 0.005 g Diiodofluorescein, 0.01 g DIDMA, .5 Dipentaerythritol penta-/hexa-acrylate), and 1 g Desmodur 75L that was polymerized at 200 mW for 1 min. b) Photograph of the same sample after exposure to air.

The Dipentaerythritol penta-/hexa-acrylate/ Desmodur 75L sample could not be tested for healing because it was made in transmission geometry, and the planes of isocyanate rest perpendicular to the structure. Another sample was made in reflection geometry that contained the same components, except the hexa-acrylate was replaced with Pentaerythritol tetraacrylate to lower the viscosity. After the sample was polymerized it was opened to air, scratched with a razor blade, and left to polymerize for 12 hours. The SEM of the scratched sample is in Figure 5.13. There is no evidence of the isocyanate leaking out and healing. The isocyanate may already be polymerized by excess hydroxyl groups in the acrylate monomers before moisture exposure, it may be too viscous to leak out into the crack before polymerization occurs, or confining the isocyanate to such small volumes may speed up the polymerization rate.
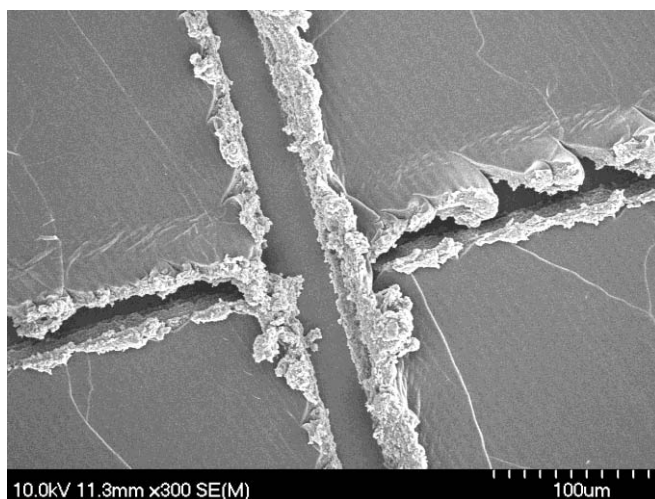
Figure 5.13. SEM micrograph of a reflection grating containing 0.005 g Diiodofluorescein, 0.01 g DIDMA, .5 Pentaerythritol tetraacrylate, and 1 g Desmodur 75L that was polymerized at 200 mW for 1 min. The grating was scratched with a razor blade in a cross pattern immediately after it was opened to air.

If the Desmodur 75L were polymerizing due to hydroxyl groups in the acrylate monomer, there should be polymerization as soon as they are mixed together. There is no evidence of isocyanate polymerization before photopolymerization. If confining the isocyanate to small

98

volumes causes the reaction rate to increase, so polymerization occurs before flow, then no chemistry will be able to create a self-healing coating. The viscosity of the resin can be altered to see if it has any effect on the isocyanates ability to leak out into the crack plane.

The viscosity of the resin can be decreased by adding low viscosity components such as IPDI, pure TDI, or solvents. It would also be interesting to switch the isocyanate from Desmodur 75L to MP210 because it has a lower viscosity and it had promising results. Adding any TDI to the Desmodur 75L samples caused foaming, so it could not be used. IPDI was added in various concentrations, and while it did not cause any foaming, it never polymerized. The initiation of the Desmodur 75L polymerization did not induce any polymerization of the IPDI. Finally, resins incorporating solvents like ethyl acetate, xylene, and acetone were photopolymerized. Because the solvents were miscible in both the acrylate and isocyanate, there was no phase separation of the two monomers and no grating formed. The samples were still cut open after polymerization and scratched with a razor. None of the samples showed evidence of healing. (Figure 5.14)
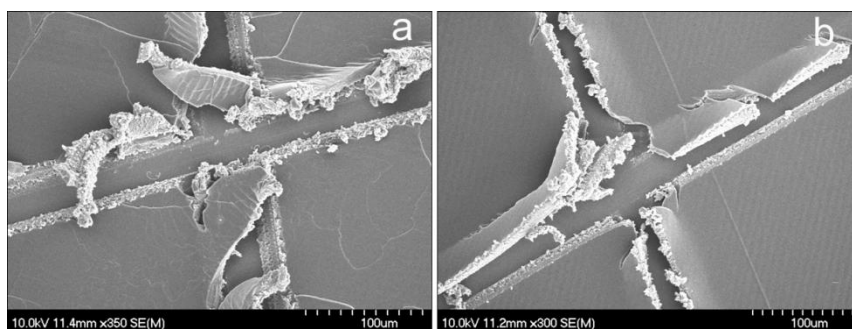
Figure 5.14. SEM micrographs of reflection gratings composed of acrylate polymer and isocyanate monomer that have been scratched and exposed to air for 12 hours. Sample a) is composed of 21 w% tetraacrylate, 69 w% Desmodur 75L, 8 w% ethyl acetate, 2 w% acetone, and less than 1 w% of Diiodoflurescein, DIDMA, and 12 μm glass spheres. Sample b) is composed of 21 w% tetraacrylate, 69 w% Desmodur 75L, 8 w% xylene, 2 w% acetone, and less than 1 w% of Diiodoflurescein, DIDMA, and 12 μm glass spheres.

5.5 Conclusions and Future Directions

Coatings composed of alternating planes of isocyanate and acrylate monomers have been fabricated via interference lithography. This method of fabrication allows monomeric isocyanate to be encapsulated within polymeric acrylate in a single step exposure, which is applicable to self- healing coatings. Coatings composed of IPDI and TMPTA monomers have the ability to change color when damage has occurred but the system cannot be healed without thermal intervention. Making the coatings self- healing may be as simple as spin-coating a layer of amine functional groups on the surface of the coating, so when damaged, the groups will polymerize the IPDI that leaks into the crack plane. More research needs to be performed test this hypothesis.

Another method of making the coating heal autonomically is to use isocyanates with greater reactivity with water. The isocyanate must phase separate from the acrylate when exposed, form a grating for autonomic readout, and leak into the crack plane when damaged, but none of the isocyanates tested have been able to do all three. Getting the isocyanate to leak into the crack plane has been the major obstacle, which could be caused by the polyisocyanate's high viscosity, or by the increase in polymerization rate due to the small volumes of monomer that are sequestered. Further research using lower viscosity isocyanates, or acrylates with less miscibility with the isocyanates may produce the desired coating.

If self- healing coatings are created by adding catalyst to the top of the holographically structured coating, interference lithography would be an efficient method for fabrication. Especially for the case where a 3D interconnected network of healing agent needs to be formed within a matrix of polymer, this method saves many steps of processing. Not only does it save

time, but the consequences of the periodic structuring allows for readout when damage has occurred. Coatings created by interference lithography show a lot of potential, but further research needs to be performed to make them self-healing.

CHAPTER 6

CONCLUSIONS

Interference lithography offers a promising single- step method of assembling nanoconstituents within nanocomposites. A system that reproducibly sequesters nanoparticles in destructive interference regions of a polymeric resin was developed. The best nanoparticle sequestration was observed at reduced laser power, smaller interferogram periodicity, and decreased nanoparticle size. This indicates that particle segregation is dominated by diffusion-limited nanoparticle transport directed by a matrix containing a gradient of polymerization kinetics. This research has provided the understanding necessary to predict whether this method would be useful with other materials systems. Large nanoconstituents can only be assembled on the surface of a composite because they scatter the incoming laser light. The nanoparticles cannot absorb the incoming laser light, or the interference pattern is attenuated. The transparency of the nanocomposite is incredibly important, making this method applicable to smaller nanoparticle systems.

A coating containing encapsulated isocyanate monomer within an acrylic matrix was fabricated by interference lithography for self- healing applications.   Due to the optical properties of the coating, it is able to readout when it has been damaged. This type of coating would be appropriate for moisture sensitive applications such as organic light emitting diodes (OLED). The OLED would be less likely to fail if the outer coating could heal itself when damaged before any moisture could leak into the device. It would also be beneficial to know when polymerization of the moisture sensitive isocyanate occurred, as a warning that the device is getting damaged. However, the current system containing a non-viscous isocyanate that leaks into the crack plane has to be thermally healed. And the system allowing a moisture-catalyzed

polymerization of the isocyanate, does not readout damage nor does it heal. To make this coating more effective, a chemistry that combines the best properties of both systems needs to be developed. The easiest way to create a self-healing coating that reads out damage would be to add a catalyst onto the surface of the coating, and to not rely on the moisture-catalyzed curing of the isocyanate.

Finally, interference lithography was used in a very conventional manner to create robust SU8 nanostructures in 1, 2, and 3 dimensions. These nanostructures were filled with liquid crystal, and the switching behavior of the liquid crystal was studied by polarization optical microscopy, reflectance, and diffraction measurements. There was strong surface anchoring of the liquid crystal on the SU8 walls, but this could be diminished by adding surfactant. 1D and 3D SU8 nanostructures were successfully switched after infiltration by the positive dielectric liquid crystal, TL213. The 2D SU8 structure could not be switched using the TL213, but instead a negative dielectric liquid crystal was used to make the photonic crystal active.

Overall, interference lithography was used to create assembled nanocomposites, self-healing coatings, and active photonic crystals. It is a nice method of quickly structuring on the nanoscale without defects. This thesis only discusses a few of the promising applications, but it will remain a highly utilized method.

REFERENCES

1.   Hecht, E., *Optics* 4ed.; Pearson Education, Inc.: San Francisco, CA, 2002.

2.   Maiman, T. H., Stimulated Optical Radiation in Ruby. *Nature* **1960,** *187*, 493-494.

3.   Joannopoulos, J. D.; Johnson, S. G.; Winn, J. N.; Meade, R. D., *Photonic Crystals: Molding the Flow of Light* second ed.; Princeton University Press: Princeton, NJ, 2008.

4.   Maldovan, M.; Thomas, E. L., *Periodic materials and interference lithography for photonics, phononics and mechanics*. Wiley-VCH: 2008; p 313.

5.   Escuti, M. J.; Crawford, G. P., Holographic Photonic Crystals. *Optical Engineering* **2004,** *43* (9), 1973-1987.

6.   Mei, D.; Cheng, B.; Hu, W.; Li, Z.; Zhang, D., Three-dimensional ordered patterns by light interference. *Optics Letters* **1995,** *20* (5), 429-431.

7.   Berger, V.; Gauthier-Lafaye, O.; Costard, E., Photonic band gaps and holography. *Journal of Applied Physics* **1997,** *82* (1), 60-64.

8.   Campbell, M.; Sharp, D. N.; Harrison, M. T.; Denning, R. G.; Turberfield, A. J., Fabrication of photonic crystals for the visible spectrum by holographic lithography. *Nature* **2000,** *404* (6773), 53-56.

9.   Chen, Y. C.; Geddes, J. B.; Iii; Lee, J. T.; Braun, P. V.; Wiltzius, P., Holographically fabricated photonic crystals with large reflectance. *Applied Physics Letters* **2007,** *91* (24), 241103.

10.   Ramanan, V.; Nelson, E.; Brzezinski, A.; Braun, P. V.; Wiltzius, P., Three dimensional silicon-air photonic crystals with controlled defects using interference lithography. *Applied Physics Letters* **2008,** *92* (17), 173304.

11.   Yang, S.; Megens, M.; Aizenberg, J.; Wiltzius, P.; Chaikin, P. M.; Russel, W. B., Creating Periodic Three-Dimensional Structures by Multibeam Interference of Visible Laser. *Chemistry of Materials* **2002,** *14* (7), 2831-2833.

12.   Miklyaev, Y. V.; Meisel, D. C.; Blanco, A.; Freymann, G. v.; Busch, K.; W.Koch; Enkrich, C.; Deubel, M.; Wegener, M., Three-dimensional face-centered-cubic photonic crystal templates by laser holography: fabrication, optical characterization, and band-structure calculations. *Applied Physics Letters* **2003,** *82*, 1284-1286.

13.   Shoji, S.; Sun, H.-B.; Kawata, S., Photofabrication of wood-pile three-dimensional photonic crystals using four-beam laser interference. *Applied Physics Letters* **2003,** *83*, 608-611.

14.   Ullal, C. K.; Maldovan, M.; Thomas, E. L.; Chen, G.; Han, Y.-J.; Yang, S., Photonic crystals through holographic lithography: Simple cubic, diamond-like, and gyroid-like structures. *Applied Physics Letters* **2004,** *84*, 5434-5437.

15.   http://ab-initio.mit.edu/photons/tutorial/.

16.   Painter, O.; Lee, R. K.; Scherer, A.; Yariv, A.; O'Brien, J. D.; Dapkus, P. D.; Kim, I., Two-Dimensional Photonic Band-Gap Defect Mode Laser *Science* **1999,** *284* (5421), 1819 - 1821

17.   Baker, S. E.; Pocha, M. D.; Chang, A. S. P.; Sirbuly, D. J.; Cabrini, S.; Dhuey, S. D.; Bond, T. C.; Létant, S. E., Detection of bio-organism simulants using random binding on a defect-free photonic crystal. *Applied Physics Letters* **2010**, 113701-04.

18.   Russell, P., Photonic Crystal Fibers *Science* **2003,** *299* (5605), 358-362.

19.   Mekis, A.; Chen, J. C.; Kurland, I.; Fan, S.; Villeneuve, P. R.; Joannopoulos, J. D., High Transmission through Sharp Bends in Photonic Crystal Waveguides. *Physical Review Letters* **1996,** *77* (18), 3787-3790.

20.   Lee, W.; Pruzinsky, S. A.; Braun, P. V., Multi-photon polymerization of waveguide structures within three-dimensional photonic crystals. *Advanced Materials* **2002,** *14*, 271-274.

21.   Lin, S. Y.; Moreno, J.; Fleming, J. G., Three-dimensional photonic-crystal emitter for thermal photovoltaic power generation. *Applied Physics Letters* **2003,** *83* (2), 380-382.

22.   Fleming, J. G.; Lin, S. Y.; El-Kady, I.; Biswas, R.; Ho, K. M., All-metallic three-dimensional photonic crystals with a large infrared bandgap. *Nature* **2002,** *417*, 52-55.

23.   Yablonovitch, E., Inhibited Spontaneous Emission in Solid-State Physics and Electronics. *Physical Review Letters* **1987,** *58* (20), 2059.

24.   Yablonovitch, E., Inhibited Spontaneous Emission in Solid-State Physics and Electronics. *Physical Review Letters* **1987,** *58*, 2059-2062.

25.   Kosaka, H.; Kawashima, T.; Tomita, A.; Notomi, M.; Tamamura, T.; Sato, T.; Kawakami, S., Photonic crystals for micro lightwave circuits using wavelength-dependent angular beam steering. *Applied Physics Letters* **1999,** *74*, 1370-1372.

26.   Sperling, L. H., *Introduction to Physical Polymer Science*. John Wiley and Sons, Inc.: New York, NY, 1992.

27.   Fouassier, J.-P., *Photoinitiation Photopolymerization and Photocuring. Fundamentals and Applications*. Hanser/Gardner Publications, Inc.: Cincinnati, OH, 1995.

28.   Flory, P. J., *Principles of polymer chemistry*. Cornell University Press: Ithaca,NY, 1953.

29.   Drzaic, P. S., *Liquid Crystal Dispersions*. World Scientific: River Edge, NJ, 1995.

30.   Salamone, J. C., *Polymeric materials encyclopedia*. CRC Press: Boca Raton, FL, 1996; Vol. 7.

31.   Belfield, K. D.; Schafer, K. J.; Liu, Y.; Liu, J.; Ren, X.; Stryland, E. W. V., Multiphoton-absorbing organic materials for microfabrication, emerging optical applications and non-destructive three-dimensional imaging *Journal of Physical Organic Chemistry* **2000,** *13*, 837-849.

32.   http://www.basf.com/group/corporate/en/brand/DAROCUR.

33.   www.sigmaaldrich.com.

34.   Odian, G. G., *Principles of polymerization*. John Wiley and Sons, Inc.: Hoboken, NJ, 2004.

35.   Zweifel, F. L. a. H., Photocrosslinking of Epoxy Resins. *Advances in Polymer Science* **1986,** *78*, 61-81.

36.   Scaiano, J. C.; Kim-Thuan, N.; Leigh, W. J., Diazonium salts in photochemistry V: photosensitized decomposition of benzenediazonium tetrafluoroborate in solutions of cationic detergents.
Journal of Photochemistry **1984,** *24*, 79-86.

37.   Crivello, J. V., Cationic polymerization — Iodonium and sulfonium salt photoinitiators. *Advances in Polymer Science* **1984,** *62*, 1-48.

38.   Crivello, J. V., The Discovery and Development of Onium Salt Cationic Photoinitiators. *Journal of Polymer Science Part A: Polymer Chemistry* **1999,** *37* (23), 4241-4254.

39.   http://pltus.textcube.com/entry/Photolithography.

40.   Sastri, V. S., *Plastics in Medical Devices: Properties, Requirements and Applications*. Elsevier Books: 2010; p 121-173.

41.   Alger, M., *Polymer science dictionary*. Chapman and Hall: London, 1997.

42.   Studer, K.; Nguyena, P. T.; Decker, C.; Beck, E.; Schwalm, R., Redox and photoinitiated crosslinking polymerization III. Clear and pigmented acrylic coatings. *Progress in Organic Coatings* **2005,** *54*, 230–239.

43.   www.sartomer.com.

44.   Gush, D. P., Ketley, A.D., Thiol/acrylate hybrid systems. *Modern Paint and Coatings* **1978,** *11*, 68.

45.   Morgan, C. R., Magnotta, F., Ketley, A.D., Thiol-ene photocurable polymers. *J Polym Sci Polym Lett Ed* **1977,** *15*, 627.

46.   Morgan, C. R., Ketley, A.D., The effect of phophones on thiol-ene curing systems. *J Polym Sci Polym Lett Ed* **1978,** *16*, 75.

47.   Hoyle, C. E.; Lee, T. Y.; Roper, T., Thiol-enes: Chemistry of the past with promise for the future. *Journal of Polymer Science Part a-Polymer Chemistry* **2004,** *42* (21), 5301-5338.

48.   http://www.microchem.com/products/pdf/SU-82000DataSheet2000_5thru2015Ver4.pdf.

49.   White, T. J.; Natarajan, L. V.; Tondiglia, V. P.; Lloyd, P. F.; Bunning, T. J.; Guymon, C. A., Holographic polymer dispersed liquid crystals (HPDLCs) containing triallyl isocyanurate monomer. *Polymer* **2007,** *48* (20), 5979-5987.

50.   Brott, L. L.; Naik, R. R.; Pikas, D. J.; Kirkpatrick, S. M.; Tomlin, D. W.; Whitlock, P. W.; Clarson, S. J.; Stone, M. O., Ultrafast holographic nanopatterning of biocatalytically formed silica. *Nature* **2001,** *413* (6853), 291-293.

51.   Vaia, R. A.; Dennis, C. L.; Natarajan, L. V.; Tondiglia, V. P.; Tomlin, D. W.; Bunning, T. J., One-Step, Micrometer-Scale Organization of Nano- and Mesoparticles Using Holographic Photopolymerization: A Generic Technique. *Advanced Materials* **2001,** *13* (20), 1570-1574.

52.   Curtis, K.; Psaltis, D., Characterization of the DuPont Photopolymer for three-dimensional holographic storage. *Applied Optics* **1994,** *33* (23), 5396-5399.

53.   Rhee, U.-S.; Caulfield, H. J.; Vikram, C. S.; Shamir, J., Dynamics of hologram recording in DuPont photopolymer. *Applied Optics* **1995,** *34* (5), 846-853.

54.   Crooker, P. P.; Yang, D. K., Polymer-dispersed chiral liquid crystal color display. *Applied Physics Letters* **1990,** *57* (24), 2529-2531.

55.   Mach, P.; Rodriguez, S. J.; Nortrup, R.; Wiltzius, P.; Rogers, J. A., Monolithically integrated, flexible display of polymer-dispersed liquid crystal driven by rubber-stamped organic thin-film transistors. *Applied Physics Letters* **2001,** *78* (23), 3592-3594.

56.   Bunning, T. J.; Natarajan, L. V.; Tondiglia, V. P.; Sutherland, R. L., Holographic Polymer- Dispersed Liquid Crystals (H-PDLCs). *Annual Review of Materials Science* **2000,** *30* (1), 83-115.

57.   Liu, Y. J.; Sun, X. W., Holographic Polymer-Dispersed Liquid Crystals: Materials, Formation, and Applications. *Advances in OptoElectronics* **2008,** (684349), 1-52.

58.   Jakubiak, R.; Tondiglia, V. P.; Natarajan, L. V.; Sutherland, R. L.; Lloyd, P.; Bunning, T. J.; Vaia, R. A., Dynamic Lasing from All-Organic Two-Dimensional Photonic Crystals. *Advanced Materials* **2005,** *17* (23), 2807-2811.

59.   Ji, H.-S.; Kim, J.-H.; Kumar, S., Electrically controllable microlens array fabricated by anisotropic phase separation from liquid-crystal and polymer composite materials. *Opt. Lett.* **2003,** *28* (13), 1147-1149.

60.   Hongwen, R.; Yun-Hsing, F.; Shin-Tson, W., Tunable Fresnel lens using nanoscale polymer-dispersed liquid crystals. *Applied Physics Letters* **2003,** *83* (8), 1515-1517.

61.   Escuti, M. J.; Qi, J.; Crawford, G. P., Tunable face-centered-cubic photonic crystal formed in holographic polymer dispersed liquid crystals. *Opt. Lett.* **2003,** *28* (7), 522-524.

62.   Bunning, T. J.; Natarajan, L. V.; Tondiglia, V. P.; Sutherland, R. L., Holographic Polymer-Dispersed Liquid Crystals (H-PDLCs). *Annual Review of Materials Science* **2000,** *30* (1), 83-115.

63.   Courtesy of Wright Patterson Air Force Base.

64.   Chou, S. Y.; Krauss, P. R.; Renstrom, P. J., Imprint Lithography with 25-Nanometer Resolution. *Science* **1996,** *272* (5258), 85-87.

65.   Xia, Y.; Whitesides, G. M., Soft Lithography. *Annual Review of Materials Science* **1998,** *28* (1), 153-184.

66.   Gonsalves, K. E.; Merhari, L.; Wu, H.; Hu, Y., Organic-Inorganic Nanocomposites: Unique Resists for Nanolithography. *Advanced Materials* **2001,** *13* (10), 703-714.

67.   Garnweitner, G.; Goldenberg, L. M.; Sakhno, O. V.; Antonietti, M.; Niederberger, M.; Stumpe, J., Large-Scale Synthesis of Organophilic Zirconia Nanoparticles and their Application in Organic-Inorganic Nanocomposites for Efficient Volume Holography. *Small* **2007,** *3* (9), 1626-1632.

68.   Sakhno, O. V.; Goldenberg, L. M.; Stumpe, J.; Smirnova, T. N., Surface modified ZrO2 and TiO2 nanoparticles embedded in organic photopolymers for highly effective and UV-stable volume holograms. *Nanotechnology* **2007,** (10), 105704.

69.   Suzuki, N.; Tomita, Y.; Ohmori, K.; Hidaka, M.; Chikama, K. In *Characterization of volume gratings formed in ZrO$_2$ nanoparticle-dispersed photopolymers*, Lasers and Electro-Optics, 2007 and the International Quantum Electronics Conference. CLEOE-IQEC 2007. European Conference on, 2007; pp 1-1.

70.   Sánchez, C.; Escuti, M. J.; van Heesch, C.; Bastiaansen, C. W. M.; Broer, D. J.; Loos, J.; Nussbaumer, R., TiO2 Nanoparticle-Photopolymer Composites for Volume Holographic Recording. *Advanced Functional Materials* **2005,** *15* (10), 1623-1629.

71.   Suzuki, N.; Tomita, Y.; Kojima, T., Holographic recording in TiO$_2$ nanoparticle-dispersed methacrylate photopolymer films. *Applied Physics Letters* **2002,** *81* (22), 4121-4123.

72.   Sakhno, O. V.; Smirnova, T. N.; Goldenberg, L. M.; Stumpe, J., Holographic patterning of luminescent photopolymer nanocomposites. *Materials Science and Engineering: C* **2008,** *28* (1), 28-35.

73.   Suzuki, N.; Tomita, Y., Silica-Nanoparticle-Dispersed Methacrylate Photopolymers with Net Diffraction Efficiency Near 100%. *Appl. Opt.* **2004,** *43* (10), 2125-2129.

74.   Sakhno, O. V.; Goldenberg, L. M.; Stumpe, J.; Smirnova, T. N., Effective volume holographic structures based on organic–inorganic photopolymer nanocomposites. *Journal of Optics A: Pure and Applied Optics* **2009,** *11*, 024013.

75.   Smirnova, T. N.; Sakhno, O. V.; Yezhov, P. V.; Kokhtych, L. M.; Goldenberg, L. M.; Stumpe, J., Amplified spontaneous emission in polymer-CdSe/ZnS-nanocrystal DFB structures produced by the holographic method. *Nanotechnology* **2009,** *20* (24), 245707.

76.   Ostrowski, A. M.; Naydenova, I.; Toal, V., Light-induced redistribution of Si-MFI zeolite nanoparticles in acrylamide-based photopolymer holographic gratings. *Journal of Optics A: Pure and Applied Optics* **2009,** *3* (11), 034004.

77.   Leite, E.; Naydenova, I.; Pandey, N.; Babeva, T.; Majano, G.; Mintova, S.; Toal, V., Investigation of the light induced redistribution of zeolite Beta nanoparticles in an acrylamide-based photopolymer. *Journal of Optics A: Pure and Applied Optics* **2009,** *2* (11), 024016.

78.   Vaia, R. A.; Maguire, J. F., Polymer Nanocomposites with Prescribed Morphology: Going beyond Nanoparticle-Filled Polymers. *Chemistry of Materials* **2007,** *19* (11), 2736-2751.

79.   Schilling, M. L.; Colvin, V. L.; Dhar, L.; Harris, A. L.; Schilling, F. C.; Katz, H. E.; Wysocki, T.; Hale, A.; Blyler, L. L.; Boyd, C., Acrylate Oligomer-Based Photopolymers for Optical Storage Applications. *Chemistry of Materials* **1999,** *11* (2), 247-254.

80.   Dhar, L., High-Performance Polymer Recording Materials for Holographic Data Storage *MRS Bulletin* **2006,** *31* (4), 324-328.

81.   Ray, S. S.; Bousmina, M., *Polymer Nanocomposites and Their Applications*. American Scientific,: Stevenson Ranch, CA, 2006.

82.   Schmidt, G.; Nakatani, A. I.; Butler, P. D.; Karim, A.; Han, C. C., Shear Orientation of Viscoelastic Polymer-Clay Solutions Probed by Flow Birefringence and SANS. *Macromolecules* **2000,** *33* (20), 7219- 22.

83.   Martin, C. A.; Sandler, J. K. W.; Windle, A. H.; Schwarz, M.-K.; Bauhofer, W.; Schulte, K.; Shaffer, M. S. P., Electric field-induced aligned multi-wall carbon nanotube networks in epoxy composites. *Polymer* **2005,** *46*, 877-886.

84.   Koerner, H.; Hampton, E.; Dean, D.; Turgut, Z.; Drummy, L.; Mirau, P.; Vaia, R., Generating triaxial reinforced epoxy/montmorillonite nanocomposites with uniaxial magnetic fields. *Chemistry of Materials* **2005,** *17* (8), 1990-1996.

85.   Bockstaller, M. R.; Mickiewicz, R. A.; Thomas, E. L., Block Copolymer Nanocomposites: Perspectives for Tailored Functional Materials. *Advanced Materials* **2005,** *17*, 1331-1349.

86.   Suzuki, N.; Tomita, Y., Real-time phase-shift measurement during formation of a volume holographic grating in nanoparticle-dispersed photopolymers. *Applied Physics Letters* **2006,** *88* (1), 011105-3.

87.   Tomita, Y.; Suzuki, N., Holographic manipulation of nanoparticle distribution morphology in nanoparticle-dispersed photopolymers. *Optics Letters* **2005,** *30* (8), 839-841.

88.   Goldenberg, L. M.; Sakhno, O. V.; Smirnova, T. N.; Helliwell, P.; Chechik, V.; Stumpe, J., Holographic Composites with Gold Nanoparticles: Nanoparticles Promote Polymer Segregation. *Chemistry of Materials* **2008,** *20* (14), 4619-4627.

89.   Tomita, Y.; Chikama, K.; Nohara, Y.; Suzuki, N.; Furushima, K.; Endoh, Y., Two-dimensional imaging of atomic distribution morphology created by holographically induced mass transfer of monomer molecules and nanoparticles in a silica-nanoparticle-dispersed photopolymer film. *Opt. Lett.* **2006,** *31* (10), 1402-1404.

90.   Suzuki, N.; Tomita, Y., Highly transparent ZrO_2 nanparticle-dispersed acrylate photopolymers for volume holographic recording. *Optics Express* **2006,** *14* (26), 12712-19.

91.   Busbee, J. D. Nanoparticle Transport using Holographic Photopolymerization. Univeristy of Illinois, Urbana-Champaign, Urbana, IL, 2009.

92.   Saleh, B. E. A.; Teich, M. C., *Fundamentals of Photonics*. John Wiey & Sons Inc.: New York, 1991.

93.   Takahashi, H.; Naito, T.; Tomita, Y., Holographic Recording in Methacrylate Photopolymer Film Codoped with Benzyl n-Butyl Phthalate and Silica Nanoparticles. *Japenese Journal of Applied Physics* **2006,** *45* (6A), 5023-5026.

94.   Astumian, R. D., Thermodynamics and Kinetics of a Brownian Motor. *Science* **1997,** *276*, 917-922.

95.   Colvin, V. L.; Larson, R. G.; Harris, A. L.; Schilling, M. L., Quantitative model of volume hologram formation in photopolymers. *Journal of Applied Physics* **1997,** *81* (9), 5913-5923.

96.   Zhao, G.; Mouroulis, P., Diffusion Model of Hologram Formation in Dry Photopolymer Materials. *Journal of Modern Optics* **1994,** *41* (10), 1929 - 1939.

97.   Busbee, J. D.; Griffith, A. T.; Natarajan, L. V.; Tongdilia, V. P.; Bunning, T. J.; A.Vaia, R.; Braun, P. V., SiO2 Nanoparticle Sequestration via Reactive Functionalization in Holographic Polymer Dispersed Liquid Crystals. *Advanced Materials* **2009,** *21*, 3659.

98.   A. Van Blaaderen; J. Van Geest; Vrij, A., Monodisperse colloidal silica spheres from tetraalkoxysilanes: Particle formation and growth mechanism *Journal of Colloid and Interface Science* **1992,** *154*, 481.

99.   Yang, H.; Holloway, P. H.; Santra, S., Water-soluble silica-overcoated CdS:Mn/ZnS semiconductor quantum dots. *J. Chem. Phys.* **2004,** *121*, 7421.

100.   Jeon, S.; Braun, P. V., Hydrothermal Synthesis of Er-Doped Luminescent TiO2 Nanoparticles. *Chemistry of Materials* **2003,** *15* (6), 1256-63.

101.   Xu, H.; Gao, L., Tetragonal nanocrystalline barium titanate powder: preparation, characterization, and dielectric properties. *Journal of the American Ceramic Society* **2003,** *86* (1), 203-5.

102.   Lu, C.; Yang, B., High refractive index organic-inorganic nanocomposites: design, synthesis and application. *Journal of Materials Chemistry* **2009,** *19*, 2884-2901.

103.   Caseri, W. R., Nanocomposites of polymers and inorganic particles: preparation, structure and properties *Mateials Science and Technology* **2006,** *22* (7), 807-817.

104.   Tsuzuki, T., Abnormal Transmittance of Refractive-Index-Modified ZnO/Organic Hybrid Films. *Macromolecular Materials and Engineering* **2008,** *293*, 109-113.

105.   Kim, P.; Jones, S. C.; Hotchkiss, P. J.; Haddock, J. N.; Kippelen, B.; Marder, S. R.; Perry, J. W., Phosphonic Acid-Modified Barium Titanate Polymer Nanocomposites with High Permittivity and Dielectric Strength. *Advanced Materials* **2007,** *19* (7), 1001-1005.

106.   Fan, X.; Lin, L.; Messersmith, P. B., Surface-initiated polymerization from TiO2 nanoparticle surfaces through a biomimetic initiator: A new route toward polymer–matrix nanocomposites. *Composites Science and Technology* **2006,** *66*, 1195–1201.

107.   Leonard, S.; Mondia, J.; van Driel, H.; Toader, O.; John, S.; Busch, K.; Birner, A.; Gosele, U.; Lehmann, V., Tunable two-dimensional photonic crystals using liquid-crystal infiltration. *Physical Review B* **2000,** *61* (4), R2389-R2392

108.   Ferrini, R.; Martz, J.; Zuppiroli, L.; Wild, B.; Zabelin, V.; Dunbar, L.; Houdre, R.; Mulot, M.; Anand, S., Planar photonic crystals infiltrated with liquid crystals: optical characterization of molecule orientation. *Optics Letters* **2006,** *31* (9), 1238-1240.

109.   Busch, K.; John, S., Liquid-crystal photonic-band-gap materials: The tunable electromagnetic vacuum. *Physical Review Letters* **1999,** *83* (5), 967-970.

110.   Maune, B.; Loncar, M.; Witzens, J.; Hochberg, M.; Baehr-Jones, T.; Psaltis, D.; Scherer, A.; Qiu, Y., Liquid-crystal electric tuning of a photonic crystal laser. *Applied Physics Letters* **2004,** *85* (3), 360-362.

111.   Li, C. Y.; Birnkrant, M. J.; Natarajan, L. V.; Tondiglia, V. P.; Lloyd, P. F.; Sutherland, R. L.; Bunning, T. J., Polymer crystallization/melting induced thermal switching in a series of holographically patterned Bragg reflectors. *Soft Matter* **2005,** *1* (3), 238-242.

112.   Chong, H. M. H.; De La Rue, R. M., Tuning of photonic crystal waveguide microcavity by thermooptic effect. *IEEE Photonics Technology Letters* **2004,** *16* (6), 1528-1530.

113.   Park, W.; Lee, J., Mechanically tunable photonic crystal structure. *Applied Physics Letters* **2004,** *85* (21), 4945-4847.

114.	Asano, T.; Kunishi, W.; Nakamura, M.; Song, B.; Noda, S., Dynamic wavelength tuning of channel-drop device in two-dimensional photonic crystal slab. *Electronics Letters* **2005,** *41* (1), 37-38.

115.	Husko, C.; Rossi, A. D.; Combrié, S.; Tran, Q. V.; Raineri, F.; Wong, C. W., Ultrafast all-optical modulation in GaAs photonic crystal cavities. *Applied Physics Letters* **2009,** *94*, 021111-4.

116.	Grillet, C.; Monat, C.; Smith, C.; Lee, M.; Tomljenovic-Hanic, S.; Karnutsch, C.; Eggleton, B., Reconfigurable photonic crystal circuits. *Laser & Photonics Reviews* **2010,** *4* (2), 192-204.

117.	Faraon, A.; Englund, D.; Bulla, D.; Luther-Davies, B.; Eggleton, B. J.; Stoltz, N.; Petroff, P.; Vuckovic, J., Local tuning of photonic crystal cavities using chalcogenide glasses. *Applied Physics Letters* **2008,** *92* (4), 043123.

118.	Kubo, S.; Gu, Z.-Z.; Takahashi, K.; Fujishima, A.; Segawa, H.; Sato, O., Tunable Photonic Band Gap Crystals Based on a Liquid Crystal-Infiltrated Inverse Opal Structure. *JACS* **2004,** *126*, 8314-8319.

119.	Ozaki, M.; Shimoda, Y.; Kasano, M.; Yoshino, K., Electric Field Tuning of the Stop Band in a. Liquid-Crystal-Infiltrated Polymer Inverse Opal. *Advanced Materials* **2002,** *14* (7), 514-518.

120.	Kang, D.; Maclennan, J. E.; Clark, N. A.; Zakhidov, A. A.; Baughman, R. H., Electro-optic Behavior of Liquid-Crystal-Filled Silica Opal Photonic Crystals: Effect of Liquid-Crystal Alignment. *Physical Review Letters* **2001,** *86*, 4052-4055.

121.	Shimoda, Y.; Ozaki, M.; Yoshino, K., Electric field tuning of a stop band in a reflection spectrum of synthetic opal infiltrated with nematic liquid crystal *Applied Physics Letters* **2001,** *79* (22), 3627-3629.

122.	Mertens, G.; Roder, T.; Schweins, R.; Huber, K.; Kitzerow, H.-S., Shift of the photonic band gap in two photonic crystal/liquid crystal composites. *Applied Physics Letters* **2002,** *80* (11), 1885-1887.

123.	Mach, P.; Wiltzius, P.; Megens, M.; Weitz, D. A.; Lin, K.-h.; Lubensky, T. C.; Yodh, A. G., Electro-optic response and switchable Bragg diffraction for liquid crystals in colloid-templated materials. *Physical Review E* **2002,** *65*, 031720.

124.   Escuti, M. J.; Qi, J.; Crawford, G. P., Tunable face-centered-cubic photonic crystal formed in holographic polymer dispersed liquid crystals. *Optics Letters* **2003,** *28* (7), 522-524.

125.   Sun, X.; Tao, X.; Ye, T.; Xue, P.; Szeto, Y.-S., 2D and 3D electrically switchable hexagonal photonic crystal in the ultraviolet range *Applied Physics B: Lasers and Optics* **2007,** *87* (2), 267-271.

126.   Tondiglia, V. P.; Natarajan, L. V.; Sutherland, R. L.; Tomlin, D.; Bunning, T. J., Holographic Formation of Electro-Optical Polymer–Liquid Crystal Photonic Crystals. *Advanced Materials* **2002,** *14* (3), 187-191.

127.   Lester, G.; Strudwick, A.; Coulston, S., Electronically switchable diffractive optical elements. *Opto-electronics review* **2004,** *12* (3), 313-316.

128.   Mittleman, D.; Bertone, J.; Jiang, P.; Hwang, K.; Colvin, V., Optical properties of planar colloidal crystals: Dynamical diffraction and the scalar wave approximation. *Journal of Chemical Physics* **1999,** *111* (1), 345-354.

129.   Kogelnik, H., Coupled Wave Theory for Thick Hologram Gratings. *The Bell System Technical Journal* **1969,** *48* (9), 2909-2927.

130.   http://dept.kent.edu/spie/liquidcrystals/maintypes3.html.

131.   Moharam, M. G.; Gaylord, T. K., Diffraction analysis of dielectric surface-relief gratings. *Journal of the Optical Society of America* **1982,** *72* (10), 1385-1392.

132.   Sakai, K.; Miyai, E.; Noda, S., Two-dimensional coupled wave theory for square-lattice photonic-crystal lasers with TM-polarization. *Optics Express* **2007,** *15* (7), 3981-3990.

133.   Moharam, M. G.; Gaylord, T. K.; Sincerbox, G. T.; Werlich, H.; Yung, B., Diffraction characteristics of photoresist surface-relief gratings. *Applied Optics* **1984,** *23* (18), 3214-3220.

134.   White, S. R.; Sottos, N. R.; Geubelle, P. H.; Moore, J. S.; Kessler, M. R.; Sriram, S. R.; Brown, E. N.; Viswanathan, S., Autonomic healing of polymer composites. *Nature* **2001,** *409* (6822), 794-797.

135.   Caruso, M. M.; Delafuente, D. A.; Ho, V.; Sottos, N. R.; Moore, J. S.; White, S. R., Solvent-Promoted Self-Healing Epoxy Materials. *Macromolecules* **2007,** *40*, 8830-8832.

136.   Cho, S. H.; Andersson, H. M.; White, S. R.; Sottos, N. R.; Braun, P. V., Polydimethylsiloxane-Based Self-Healing Materials. *Advanced Materials* **2006,** *18*, 997–1000.

137.   Toohey, K. S.; Sottos, N. R.; Lewis, J. A.; Moore, J. S.; White, S. R., Self-healing materials with microvascular networks. *Nat Mater* **2007,** *6* (8), 581-585.

138.   Toohey, K. S.; Hansen, C. J.; Lewis, J. A.; White, S. R.; Sottos, N. R., Delivery of Two-Part Self-Healing Chemistry via Microvascular Networks. *Adv. Funct. Mater.* **2009,** *19*, 1399-1405.

139.   Hansen, C. J.; Wu, W.; Toohey, K. S.; Sottos, N. R.; White, S. R.; Lewis, J. A., Self-Healing Materials with Interpenetrating Microvascular Networks. *Adv. Mater.* **2009,** *21*, 1-5.

140.   Braun, P. V.; Griffith, A.; Cho, S. H.; White, S. R., Self-healing Polymer Coatings. *Polymeric Materials Science and Engineering Preprint* **2009,** *100*, 353-354.

141.   Cho, S. H.; White, S. R.; Braun, P. V., Self-Healing Polymer Coatings. *Advanced Materials* **2009,** *21*, 645–649.

142.   Studer, K.; Decker, C.; Beck, E.; Schwalm, R.; Gruber, N., Redox and photoinitiated crosslinking polymerization I. Dual-cure isocyanate-acrylate system. *Progress in Organic Coatings* **2005,** *53*, 126-133.

143.   Agre, C. L.; Dinga, G.; Pflaum, R., Organic Anti-Foaming Agents. *The Journal of Organic Chemistry* **1955,** *20* (6), 695-699.

AUTHOR'S BIOGRAPHY

Abby Juhl was born as Abigail Griffith in Blue Island, Illinois on June 26th, 1983. She completed kindergarten through 8th grade at a variety of schools in Illinois and North Carolina. Abby graduated high school from Sanderson High in Raleigh, NC in 2001. She continued on to North Carolina State University where she graduated with a B.S. in Materials Science and Engineering in 2005. She came to the University of Illinois to complete a PhD in Materials Science and Engineering under the supervision of Paul Braun. Some of her PhD research was completed at Wright Patterson Air Force Base in Dayton, Ohio. Abby is now a post-doc at Wright Patterson and is living with her husband in Dayton, Ohio.